

A Thesis for the Degree of Ph.D. in Science

**Theoretical study towards realization of
measurement-based quantum computers**

April 2011

GRADUATE SCHOOL OF SCIENCE AND TECHNOLOGY
KEIO UNIVERSITY

Agung Trisetyarso

Principal Adviser

Prof. Kohei M. Itoh Keio University

Associate Advisers

Prof. Rodney Van Meter Keio University

Prof. Naoki Yamamoto Keio University

Prof. Tatsuhiko Koike Keio University

Prof. Eiji Ohta Keio University

Keywords: Dirac potentials, atomic inversion, Darboux transformations, measurement-based quantum computation, quantum carry-lookahead adder, optimization.

©Copyright by Agung Trisetyarso 2011

All rights reserved.

*I would like to dedicate this thesis to
my loving parents, teachers, family,
and friends ...*

Acknowledgements

Say: "If the ocean were ink (wherewith to write out) the words of my Lord, sooner would the ocean be exhausted than would the words of my Lord, even if we added another ocean like it, for its aid."

The cave: 110

"I do not know what I may appear to the world; but to myself I seem to have been only like a boy playing on the seashore, and diverting myself in now and then finding a smoother pebble or a prettier shell than ordinary, whilst the great ocean of truth lay all undiscovered before me."

Isaac Newton

The end of my Ph.D program is just a beginning for a long journey of search of truth; as mentioned by Sir Isaac Newton, we are only a "boy playing on the seashore" while "the great ocean of truth lay all undiscovered before us"; the ocean of truth in which very deep, very beautiful, and unlimited.

Without help and support from loving parents, teachers, family, and friends, it is impossible for me to enjoy the beauty of quantum world.

It was my father, who introduced me to the thought of Richard Feynman; he has "Surely you're joking, Mr. Feynman!"^[1] among his great library. It seems that he was an admirer of Feynman when he was

a student in Kyoto University about forty years ago; the time when Sin-Itiro Tomonaga, Julian Schwinger, and Richard Feynman were awarded Nobel prize in 1965. Hopefully *Our Lord* will place him in the good condition there. My loving mother supports me with endless love and care, at which this achievement is part of my main motivation to felicitate her.

Most importantly, I would like to thank my loving daughter *Rahma* and my loving wife *Pepi* for their endless patience and support so that at last the Ph.D can be achieved. I apologize for *your patience* because I spent a lot of time in Laboratory and go home in very late of night.

I remember, it was in 2007 that Prof. Kohei M. Itoh accepted me as his Ph.D student. For me, it is a great honor that such great Professor want to offer an ordinary man like me. The research environment in Prof. Kohei M. Itoh group is amazing. I really enjoy the presentation of Itoh group members and also from the guests, even sometimes the field is relatively far from what I am doing. Prof. Kohei M. Itoh always encourages me in his style so that I can accomplish the achievement. Therefore, I am very grateful to Prof. Kohei M. Itoh for all helps and supports.

Obviously, the most important person during my Ph.D program is Prof. Rodney Van Meter. His patience and ingenuity lead me to this achievement. I learn a lot of how to think simple without loss of accuracy to solve a hard problem. My skill of \LaTeX is nothing if Prof. Rodney Van Meter did not introduce and teach me about it. Also, the skill of writing scientific paper was entirely supervised by Prof. Rodney Van Meter.

I also would like to thank my teachers in ITB (Institut Teknologi Bandung) starting from Prof. Pantur Silaban who introduced me to the beauty world of theoretical physics, Hans Wospakrik Ph.D who introduced me to the Darboux transformations, and also Prof. Freddy

Permana Zen and Alexander Iskandar Ph.D who are my “everlasting” supervisors.

Endlessly thank to *Our Lord*, I also feel very fortunate that I have remarkable friends during my Ph.D program in Japan. Members of Itoh research group always support me even for the small things such as preparing my presentation for the seminar group. I would like to thank especially Shino Aizawa for her support on my official tasks. I am very grateful to all the members whom we spent fun time: Yoko Kawamura, Toyofumi Ishikawa, Hiroki Morishita, Muhammad R. Rahman, Akhtar M. Waseem, Tomoya Arai, Erika Kawakami, Fang Fang, Yang, Nao Harada, Rii Hirano, Takashi Matsuoka, Katsuhiko Naito, Pierre-Andre Mortemousque, Takahisa Tanaka, Hiroyuki Tezuka, Go Tsuchiya, Luis Jou Garcia, Itaru Arikawa, Satoru Miyamoto, Fumi Yamaga, Hajime Sinohara, Ryo Tomita, Taiga Isoda, Masashi Hirose, and Eri Satou. Thanks a lot for discussions and all supports.

Indonesian communities, especially whom are in Japan, should also be taken into this Acknowledgement. I am very grateful to Achmad Husni Thamrin, Achmad Basuki, Muhammad Dikshie, Pak Totok Suhardiyanto, Ali Barakbah, and friends in SFC campus, Indonesian community in Yagami campus such as Nugroho, Arya, and friends, and also my loving neighbors in Jiyugaoka. I also would like to thank Munawar Riyadi (UTM, Malaysia), one of my best friend when I was a student in ITB.

I also would like to thank Japanese government and also Keio University for financial supports on my research. My work was supported in part by Grant-in-Aid for Scientific Research by MEXT, Specially Promoted Research No. 18001002 and in part by Special Coordination Funds for Promoting Science and Technology and in part by The Keio Leading-edge Laboratory of Science and Technology (KLL).

Abstract

Measurement-based quantum computation (MBQC) is a new exciting paradigm in the field of quantum computation, in which the quantum information processing is proceeded by the sequences of measurements on the logical qubits encoded in a highly entangled state. MBQC is considered to be one of the most realistic formats of quantum computer since it is more robust than the conventional reversible quantum computation protocols. However, there exists a number of challenges to overcome.

This dissertation presents a theoretical study towards realization of measurement-based quantum computer using a single atom contained in a cavity as a qubit node. The control of coherence are achieved with the assistance of an externally applied classical field. An architecture for large number of qubits in a cluster state is also presented.

The first half of this dissertation presents a technique to ensure the qubit coherency because the measurement over the cluster state needs to be performed on the coherently evolving qubits. Under this scheme, a cavity is irradiated concurrently with quantum and classical electromagnetic fields to manipulate the atomic population. It is shown theoretically that manipulation of the time evolution of the population of two states in cavity quantum electrodynamics (QED) is possible by introduction of an appropriate electromagnetic field. The theoretical justification is provided by the use of Darboux transformations on the potential in an one-dimensional stationary Dirac model. Here, Pauli matrices are the central parameters for controlling the collapse and revival of the Rabi oscillations.

The second half of this dissertation presents a new architecture of MBQC. The circuit design and evaluation of a quantum carry-lookahead

adder (QCLA) in MBQC are proposed as a MBQCLA protocol. MBQCLA utilizes MBQC's ability to transfer quantum states in unit time to accelerate addition. MBQCLA breaks the latency limit of addition circuits in nearest neighbor-only architectures : compared to the $\Theta(n)$ limit on circuit depth for linear nearest-neighbor architectures, it can reach $\Theta(\log n)$ depth. MBQCLA is an order of magnitude faster than a ripple-carry adder when adding registers longer than 100 qubits, but requires a cluster state that is an order of magnitude larger. The cluster state resources can be divided into computation and communication parts; for the unoptimized form, $\approx 88\%$ of the resources are used for communication. Hand optimization of horizontal communication costs results in a $\approx 12\%$ reduction in spatial resources for the in-place.

The work provides a theoretical study on manipulation of qubit coherency and the architecture for quantum adder towards realization of measurement-based quantum computers. Considering that the proposal is compatible with the framework of present experimental investigations, this work may contribute directly to the next step of MBQC development.

Contents

| | |
|---|------------|
| Nomenclature | xiv |
| 1 Introduction | 1 |
| 1.1 History of quantum computation | 1 |
| 1.1.1 Quantum bit | 2 |
| 1.1.2 Quantum logic gates | 7 |
| 1.1.3 Quantum measurement | 13 |
| 1.1.4 Quantum logic gates and Schrödinger equation | 14 |
| 1.2 Abstract quantum computation | 17 |
| 1.3 Measurement-based quantum computation | 19 |
| 1.3.1 MBQC gates and graphical notation | 21 |
| 1.4 Darboux transformations | 25 |
| 1.4.1 Darboux transformation and Crum theorem | 25 |
| 1.5 Problem definition | 28 |
| 1.6 Contributions of this thesis | 28 |
| 2 Correlation of Dirac potentials and atomic inversion in cavity quantum electrodynamics | 30 |
| 2.1 Cavity quantum electrodynamics | 30 |
| 2.2 Problem definition | 33 |
| 2.2.1 BBGS-Darboux transformations | 36 |
| 2.3 Rabi model under BBGS-Darboux transformation | 37 |
| 2.3.1 Rabi model in one-dimensional Dirac equation | 38 |
| 2.3.2 The action of BBGS-Darboux transformation on Rabi model in one-dimensional Dirac equation | 39 |

| | | |
|----------|--|-----------|
| 2.3.2.1 | $\mathcal{D}(\sigma_1)$ | 40 |
| 2.3.2.2 | $\mathcal{D}(\sigma_3)$ | 43 |
| 2.3.2.3 | $\mathcal{D}(\sigma_2)$ | 43 |
| 2.4 | Correlations of the one-dimensional stationary Dirac field potential and the Rabi oscillations | 45 |
| 2.4.1 | The parabolic potential | 45 |
| 2.4.2 | The harmonic oscillator potentials | 50 |
| 2.5 | The trade-off between quantum and classical light | 57 |
| 2.6 | Physical implementation | 62 |
| 2.7 | Limitation and future works | 63 |
| 3 | Circuit design for a measurement-based quantum carry-lookahead adder | 64 |
| 3.1 | Introduction | 64 |
| 3.2 | Background | 66 |
| 3.2.1 | Quantum carry-lookahead adder | 66 |
| 3.2.2 | Out-of-place and in-place procedures for abstract quantum carry-lookahead adder | 68 |
| 3.2.3 | Space and depth complexities trade-off in nearest-neighbor interactions architectures | 69 |
| 3.3 | Quantum carry-lookahead adder for measurement-based quantum computation | 70 |
| 3.3.1 | Evaluating algorithms executed using MBQC | 70 |
| 3.3.2 | Out-of-place measurement-based quantum carry-lookahead adder | 73 |
| 3.3.3 | In-place measurement-based quantum carry-lookahead adder | 76 |
| 3.3.4 | MBQCLA latencies | 80 |
| 3.3.5 | Optimized in-place MBQCLA | 80 |
| 3.3.5.1 | Bent network in quantum carry-lookahead adder | 80 |
| 3.3.5.2 | Optimized circuit formulation | 81 |
| 3.3.6 | Graph state quantum carry-lookahead adder (GSQCLA) | 81 |
| 3.3.7 | Resource comparison | 83 |
| 3.4 | Limitation and future works | 89 |

CONTENTS

| | | |
|----------|--|------------|
| 4 | Summary | 90 |
| A | Homotopy perturbation methods | 93 |
| B | Explicit representation for square root of a complex number | 95 |
| C | Computational simulation scheme | 97 |
| D | List of Papers and Presentations | 100 |
| | D.1 Journals | 100 |
| | D.2 Conferences | 100 |
| | D.3 Workshop | 101 |
| | References | 112 |

List of Figures

| | | |
|------|---|----|
| 1.1 | Bloch sphere. | 2 |
| 1.2 | A multipartite quantum system. | 4 |
| 1.3 | Controlled-NOT gate. | 7 |
| 1.4 | Controlled-Controlled-NOT gate. | 8 |
| 1.5 | Deutsch -gate. | 9 |
| 1.6 | Deutsch -gate decomposition. | 9 |
| 1.7 | Quantum measurement. | 13 |
| 1.8 | Comparison between non- and nearest neighbor quantum computers. The yellow and red balls represent the qubits. The lines between the qubits express the communications which are allowed. | 17 |
| 1.9 | NOT gate in MBQC. The input qubit and all pink qubits are measured in the σ_x -eigenbasis and the framed-green qubit is measured in an adaptive basis depending on the measurement outcome of qubit 2. A rotation measurement operator on xy -plane around z -axis with angle π on qubit 3 makes the qubit 3 not adaptive. | 22 |
| 1.10 | Quantum gates in measurement-based quantum computation. Due to the relationship between CCNOT and Toffoli Phase Gate (TPG), $\text{CCNOT} = H_t(\text{TPG})H_t^\dagger$, the target qubit can be chosen arbitrarily by putting a Hadamard gate on the chosen qubit. The Toffoli phase gate is $\text{CCNOT}^{\langle 54 \rangle}$ | 23 |
| 1.11 | Non-adjacent computation. The implementation of four types SWAP gates to propagate the information up-to-down of non-adjacent qubits for performing CNOT. Qubit $ a\rangle$ acts as the control qubit and $ b\rangle$ is the target qubit. | 24 |

LIST OF FIGURES

| | | |
|------|--|----|
| 2.1 | Cavity QED. | 31 |
| 2.2 | Comparison between semiclassical and quantum Rabi oscillations on resonance ($\Delta = 0$). | 32 |
| 2.3 | The evolution of classical electromagnetic field intensity. | 46 |
| 2.4 | The time evolution of the population of two states 2.4(a) and the time evolution of Dirac potential 2.4(b) in cavity quantum electrodynamics of $\mathcal{D}(\sigma_1)$ for $t = 100$ | 47 |
| 2.5 | The time evolution of the population of two states (2.5(a)) for t is from 0 to 10 and for t is from 0 to 2 (2.5(b)) in cavity quantum electrodynamics of $\mathcal{D}(\sigma_1)$. These figures are simulated for 6000 data points. | 48 |
| 2.6 | The time evolution of the population of two states (2.6(a)) and the time evolution of Dirac potential (2.6(b)) in cavity quantum electrodynamics of $\mathcal{D}(\sigma_3)$ for $t = 10^5$ | 51 |
| 2.7 | The time evolution of the population of two states (2.7(a)) and the time evolution of Dirac potential (2.7(b)) in cavity quantum electrodynamics of $\mathcal{D}(\sigma_3)$ for t is from 0 to 100. These figures are simulated for 6000 data points. | 52 |
| 2.8 | The time evolution of the population of two states (2.8(a)) and the time evolution of Dirac potential (2.8(b)) in cavity quantum electrodynamics of $\mathcal{D}(\sigma_3)$ for t is from 0 to 1. These figures are simulated for 6000 data points. | 53 |
| 2.9 | The time evolution of the population of two states (2.9(a)) and the time evolution of Dirac potential (2.9(b)) in cavity quantum electrodynamics of $\mathcal{D}(\sigma_2)$ for t is from 0 to 100. These figures are simulated for 6000 data points. | 54 |
| 2.10 | The time evolution of the population of two states (2.10(a)) and the time evolution of Dirac potential (2.10(b)) in cavity quantum electrodynamics of $\mathcal{D}(\sigma_2)$ for t is from 0 to 10. These figures are simulated for 6000 data points. | 55 |
| 2.11 | The comparison between the quantum Rabi oscillations and the changes due to the Darboux transformations. | 56 |

LIST OF FIGURES

| | | |
|------|---|----|
| 2.12 | (a). $ b_1 = 1000, n = 0$, (b). $ b_1 = 10, n = 1$; (c). $ b_1 = 0, n = 1$; (d). $ b_1 = 10, n = 100$; (e). $ b_1 = 0, n = 1000$; (f). $ b_1 = 1000,$ $n = 1000$ | 58 |
| 2.13 | (a). $ b_2 = 0, n = 1000$; (b). $ b_2 = 0, n = 10$; (c). $ b_2 = 10,$ $n = 1000$; (d). $ b_2 = 1000, n = 10$; (e). $ b_2 = 1000, n = 0$; (f). $ b_2 = 1000, n = 1000$ | 60 |
| 2.14 | (a) and (b). $ b_3 = 0, n = 1000$; (c). $ b_3 = 10, n = 1000$; (d). $ b_3 = 1000, n = 10$; (e). $ b_3 = 500, n = 500$; (f). $ b_3 = 0, n = 1000$. | 61 |
| 3.1 | Illustration for circuit costs for MBQCLA. On a two-dimensional Manhattan grid, the costs contain computational and communica- tion costs. The resources for communication costs can be separated into two types of resources: horizontal (wires) and vertical (SWAP gates). | 71 |
| 3.2 | Out-of-place MBQCLA. For $n=10$, the circuit consists of: 4 addi- tion blocks, 9 rounds of gates for the carry networks (2 Propagate, 3 Generate, 2 Inverse Propagate and 2 Carry networks). For ex- planation of the colors, see Subsection (1.3.1). | 74 |
| 3.3 | Size and depth comparison between MBQC VBE and MBQCLA. “+”, “ \star ”, “o” and “ \square ” marks are for in-place, optimized in-place, out-of-place and MBQC VBE circuits, respectively. | 76 |
| 3.4 | Comparison of computational and communication resources in in- place MBQCLA circuit. The bottom line on the graph repre- sents the ideal circumstance for the computational resource and the other two show the circuit with additional resources for the horizontal and the vertical communications. | 84 |
| 3.5 | In-place MBQCLA. For $n=10$, the circuit consists of: 8 addition circuits, 18 carry networks (4 Propagate, 6 Generate, 4 Inverse Propagate and 4 Carry networks) | 85 |
| 3.6 | Optimized in-place circuit. The low $n-1$ bits of the carry string output are tucked into the interior of the circuit by bending the network. | 86 |

LIST OF FIGURES

| | | |
|-----|---|----|
| 3.7 | The optimized in-place MBQCLA circuit forms a diamond-like circuit. Hand optimization of the circuit reduced the size by $\approx 12\%$ | 87 |
| 3.8 | MBQCLA figure allowing the use of a graph state for entanglement and communication. | 88 |
| 4.1 | Cluster state initialization. | 91 |
| 4.2 | A schematic showing the contributions of this thesis and also for the future works. | 92 |
| C.1 | <i>Maple</i> codes for the <i>modified</i> atomic inversion. | 97 |
| C.2 | <i>Maple</i> codes for the solution of $\mathcal{D}(\sigma_1)$ | 98 |
| C.3 | <i>Maple</i> codes for the solution of $\mathcal{D}(\sigma_3)$ | 98 |
| C.4 | <i>Maple</i> codes for the modified atomic inversion in the case of $\mathcal{D}(\sigma_2)$ | 99 |
| C.5 | The scheme for obtaining the correlations between atomic inversion and Dirac potentials. | 99 |

Chapter 1

Introduction

It is probably true generally that in the history human thinking the most fruitful developments frequently take place at those points where two different lines of thought meet. These lines may have their roots in quite different parts of human culture, in different times or different cultural environments or different religious traditions; hence if they actually meet, that is, if they are at least so related each other that a real interaction can take place, than one may hope that a new interesting developments may follow.

Werner Heissenberg

1.1 History of quantum computation

Richard Feynman's argument that quantum effects can be used as resources for simulating physics in 1982^[2] marked the birth of a new concept, *quantum computation*. Since then, the idea has stimulated new directions in the scientific and engineering research^[3]. The symbiotic relation between quantum mechanics and the field of computer science and information theory also emerged. The curiosity that the computer science and information theory may influence the fundamental understanding of nature has been discussed intensively^[4].

Conventionally, the quantum computation is composed of three parts^[5]:

1. The input of data which is encoded in quantum binary digits or *qubits*.

1.1 History of quantum computation

2. A design of a quantum circuit consisting of *quantum gates* to perform unitary transformations.
3. *Measurement* on the output state in the computational basis of the individual qubits.

1.1.1 Quantum bit

Deutsch introduced the notion of a “*bit*” in quantum computation which was renamed as a “*qubit*” seven years later by Benjamin Schumacher^[6]. The similarity between classical and quantum binary digits is that information is encoded in the string of binary numbers. However, the qubit is represented in *Dirac notation* in which a vector,

$$|\Psi\rangle = \cos\frac{\phi}{2}|0\rangle_z + e^{i\theta}\sin\frac{\phi}{2}|1\rangle_z, \quad (1.1)$$

belongs to Bloch sphere in Fig. (1.1), thus it obeys the laws of a vector in a complex separable Hilbert space.

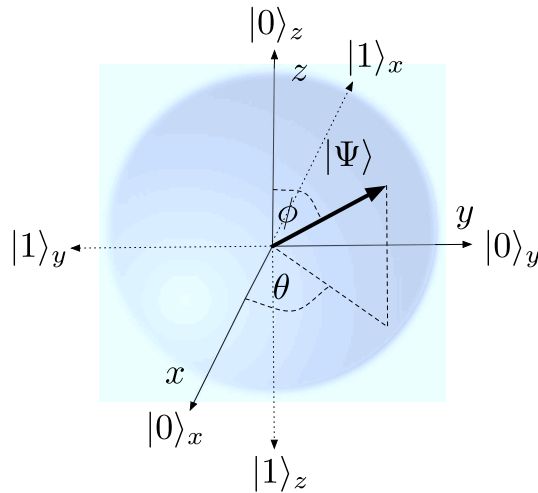


Figure 1.1: Bloch sphere.

Three properties of qubit which distinguishes from the conventional bit are:

1. *Superposition*. In the case of one bit, in contrast to the classical bit which encodes information in “1” or “0,” the representation of one qubit is *allowed*

1.1 History of quantum computation

in the linear combination, or *superposition*, of bases

$$|\Psi\rangle = a_0|0\rangle_\kappa + a_1|1\rangle_\kappa = \sum_{i=0}^1 a_i|i\rangle_\kappa, \quad (1.2)$$

in which the Eq. (1.2) has to fulfill the following normalization condition

$$\sum_i |a_i|^2 = 1, \quad (1.3)$$

where a_i , which can be a real or complex number, is an amplitude and $|i\rangle_\kappa$ is computational bases of qubit $|\Psi\rangle$. Subscript “ κ ” denotes the type of eigenbasis on the Bloch sphere as shown in Fig. (1.1), which can be $\{x, y, z\}$. The eigenbases are essentially eigenstates of Pauli matrices; therefore, they can be represented as following

- z -eigenbases

$$\{|0\rangle_z, |1\rangle_z\} = \left\{ \begin{pmatrix} 1 \\ 0 \end{pmatrix}, \begin{pmatrix} 0 \\ 1 \end{pmatrix} \right\}, \quad (1.4)$$

- x -eigenbases

$$\begin{aligned} \{|0\rangle_x, |1\rangle_x\} &= \left\{ \frac{1}{\sqrt{2}} \begin{pmatrix} 1 \\ 1 \end{pmatrix}, \frac{1}{\sqrt{2}} \begin{pmatrix} 1 \\ -1 \end{pmatrix} \right\} \\ &= \left\{ \frac{|0\rangle_z + |1\rangle_z}{\sqrt{2}}, \frac{|0\rangle_z - |1\rangle_z}{\sqrt{2}} \right\} \\ &= \{|+\rangle, |-\rangle\}, \end{aligned} \quad (1.5)$$

- y -eigenbases

$$\begin{aligned} \{|0\rangle_y, |1\rangle_y\} &= \left\{ \frac{1}{\sqrt{2}} \begin{pmatrix} 1 \\ i \end{pmatrix}, \frac{1}{\sqrt{2}} \begin{pmatrix} 1 \\ -i \end{pmatrix} \right\} \\ &= \left\{ \frac{|0\rangle_z + i|1\rangle_z}{\sqrt{2}}, \frac{|0\rangle_z - i|1\rangle_z}{\sqrt{2}} \right\}. \end{aligned} \quad (1.6)$$

A conventional way to symbolize the time evolution of a qubit is by simply horizontal line as the following

1.1 History of quantum computation

$$|\Psi\rangle \text{ ————— } |\Psi\rangle$$

in which the horizontal axis represents *time*.

2. *Entanglement*. A quantum system can be a composite of multiple qubits and it is called *a multipartite quantum system*^[7]. Mathematically, a *general* composite system, $|\Psi_g\rangle$, can be constructed by tensor products of n -number of pure states, $\{|\Psi_1\rangle, |\Psi_2\rangle, \dots, |\Psi_n\rangle\}$,

$$|\Psi_g\rangle = |\Psi_1\rangle \otimes |\Psi_2\rangle \otimes \dots \otimes |\Psi_n\rangle. \quad (1.7)$$

The multipartite state is symbolized as below

$$|\Psi_g\rangle \left\{ \begin{array}{c} |\Psi_1\rangle \text{ ————— } |\Psi_1\rangle \\ |\Psi_2\rangle \text{ ————— } |\Psi_2\rangle \\ \dots \quad \dots \quad \dots \quad \dots \\ |\Psi_n\rangle \text{ ————— } |\Psi_n\rangle \end{array} \right\} |\Psi_g\rangle$$

Figure 1.2: A multipartite quantum system.

In the case of two qubits, there are $2^2 = 4$ bases states which can be obtained by the following form

$$\{|x_0x_1\rangle | x_0, x_1 \in \{0, 1\}\} = \{|0\rangle, |1\rangle\} \otimes \{|0\rangle, |1\rangle\}, \quad (1.8)$$

and the arbitrary quantum state for 2-qubits is

1.1 History of quantum computation

$$\begin{aligned}
 |\Psi'\rangle &= |\Psi\rangle \otimes |\Psi\rangle & (1.9) \\
 &= a_{00}|00\rangle + a_{01}|01\rangle + a_{10}|10\rangle + a_{11}|11\rangle \\
 &= \sum_{i=0}^1 \sum_{j=0}^1 a_{ij}|ij\rangle.
 \end{aligned}$$

Therefore, one can generalize for n -qubits^[8]

$$|\Psi\rangle = \sum_{x \in \{0,1\}^j} a_x |x_1, \dots, x_j\rangle, \quad \sum_x |a_x|^2 = 1. \quad (1.10)$$

However, there are certain conditions in which the composite system is not fulfilled by Eq. (1.7) meaning that it is *inseparable*. This kind of system is called an *entangled* state, $|\Psi_\varepsilon\rangle$, and obeys

$$|\Psi_\varepsilon\rangle \neq |\Psi_1\rangle \otimes |\Psi_2\rangle \otimes \dots \otimes |\Psi_n\rangle. \quad (1.11)$$

There are various types of entangled states^[9]; the famous ones are Bell states^[10], Greenberger-Horne-Zeilinger (GHZ) states^[11], and cluster states^[12]. The understanding of the nature of entanglement may still in progress, however this concept is a pivot role in the development of quantum information and computation^[13].

3. *Phase*. In contrast to classical bit representation, an attribute of phase on a qubit is allowed in quantum computation. There are two types of phase:

- *Global phase*. Consider the following transformation of a quantum state

$$|\psi\rangle \rightarrow |\psi'\rangle = e^{i\theta}|\psi\rangle. \quad (1.12)$$

Where “ $e^{i\theta}$ ” is so-called *global phase factor*, $|\psi\rangle$ ($|\psi'\rangle$) is the old (new) quantum state, and θ is a real number.

1.1 History of quantum computation

- *Relative phase.* This kind of phase is indexed by the “+/-” sign on the qubits. As an example, consider the below transformations

$$|0\rangle_z \rightarrow |0\rangle_x = \frac{|0\rangle_z + |1\rangle_z}{\sqrt{2}}. \quad (1.13a)$$

$$|1\rangle_z \rightarrow |1\rangle_x = \frac{|0\rangle_z - |1\rangle_z}{\sqrt{2}}. \quad (1.13b)$$

As can be clearly seen that the relative phase distinguishes between “ $|0\rangle_x$ ” and “ $|1\rangle_x$ ”: the sign “+” on $|1\rangle_z$ in Eq. (1.13a) defining “ $|0\rangle_x$ ” while the sign “-” on $|1\rangle_z$ in Eq. (1.13b) defining “ $|1\rangle_x$ ”.

1.1.2 Quantum logic gates

The motivation of connecting between quantum mechanics and reversible computation comes from the fact that the nature of quantum physics is also reversible, since the unitary operator $U^{-1} = U^\dagger$ indicates that the reverse time evolution always takes place^[8]. Remarkably, this reconciliation is useful to define an universal quantum gate which is one of the classical problems in theory of computation^[7]. In classical computer science, **NAND**-gate alone can perform universal Boolean computation. Quantum universality for a single qubit implies ability to create any desired states on Bloch sphere which is known to be achievable with any entangling gate and arbitrary one-qubit rotations^[14]. While the universal quantum gate for n -qubits is defined by the ability of this gate to implement any unitary transformations. Below, starting from the universality of **TOFFOLI**-gate discussion, the story of how universal quantum logic gates emerges will be explained.

According to Ref.^[7,15], the original notion of reversible computation came from “*billiard ball computer*” which is coined by Edward Fredkin in 1981 and it is called *Fredkin gate* afterwards. Later, the idea was developed by Toffoli, Deutsch and Barenco *et. al* in 1995^[8] to deliver the definition of elementary quantum gates. The story of reversible computation and quantum mechanics reconciliation began from the following reversible gate

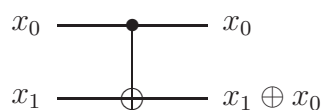


Figure 1.3: **Controlled-NOT** gate.

which is called **Controlled-NOT**-gate or **CNOT**-gate, since in this kind of gate the *first qubit*, x_0 , is used as *control* bit and the *second qubit*, x_1 , is as *target* bit, i.e., operation of **XOR**-gate is performed on the *second qubit* by the *first qubit*. In the case $x_0 = 1$, the second bit is operated with the **NOT**-gate.

1.1 History of quantum computation

The most astonishing result of reversible computation was coined by Toffoli which is called **Controlled-Controlled-NOT**-gate or **TOFFOLI**-gate which is in the following form

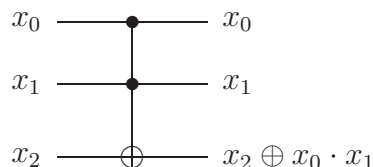


Figure 1.4: **Controlled-Controlled-NOT** gate.

If this gate is denoted by $\mathcal{F}_{\text{TOFFOLI}}(x_0, x_1, x_2) = (x_0, x_1, x_2 \oplus x_0 \cdot x_1)$, it is easy to obtain that **TOFFOLI** is an universal gate:

- $\mathcal{F}_{\text{TOFFOLI}}(1, 1, x_2) = \mathcal{F}_{\text{NOT}}(x_2)$.
- $\mathcal{F}_{\text{TOFFOLI}}(1, x_1, x_2) = \mathcal{F}_{\text{CNOT}}(x_1, x_2)$.
- $\mathcal{F}_{\text{TOFFOLI}}(x_0, x_1, 0) = \mathcal{F}_{\text{AND}}(x_0, x_1)$.
- $\mathcal{F}_{\text{TOFFOLI}}(x_0, x_1, 1) = \mathcal{F}_{\text{NAND}}(x_0, x_1)$.
- $\mathcal{F}_{\text{TOFFOLI}}(\mathcal{F}_{\text{TOFFOLI}}(x_0, x_0, 1), \mathcal{F}_{\text{TOFFOLI}}(x_1, x_1, 1), 1) = \mathcal{F}_{\text{OR}}(x_0, x_1)$
because $\mathcal{F}_{\text{NAND}}(\mathcal{F}_{\text{NAND}}(x_0, x_0), \mathcal{F}_{\text{NAND}}(x_1, x_1)) = \mathcal{F}_{\text{OR}}(x_0, x_1)$.

As can be seen above, Fredkin and Toffoli successfully showed how to emulate classical Boolean logic by three-bit gates of universal reversible computation; however, it does not enough to define an universal gate for quantum computation.

In quantum computation, every quantum circuit can be constructed by a quantum gate of a single qubit, which is a 2×2 unitary matrix, as provided in Table (1.1). The unique properties of quantum over the classical computation are that **NOT**-gate for σ_z -eigenbases, or to flip the qubit, can be done by Pauli- X matrix, while to flip the phase of $\{\sigma_x, \sigma_y\}$ -eigenbases can be performed by Pauli- Z matrix. The convention to symbolize a quantum gate is by $\bigwedge_n(U)$ ^[8] which has dimensions $2^{n+1} \times 2^{n+1}$ and processes 2^{n+1} qubits as shown in Table (1.2).

1.1 History of quantum computation

Under this scheme, a Toffoli gate is essentially a special case of a **Controlled-Controlled Unitary**-gate. If the unitary matrix in **Controlled-Controlled Unitary** gate is substituted by Phase gate, this kind of gate is called **TOFFOLI Phase-gate** (TPG) which is extensively used in this dissertation.

The first effort to construct universal quantum gates was coined by David Deutsch in 1989^[16], when he showed that an universal quantum gate can be accomplished by *modifying* the Toffoli gate which was well known for the universal gate in reversible computation^[15,17]. The modified Toffoli gate which is later known as **Deutsch-gate** is

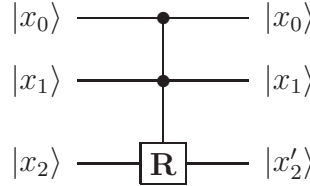


Figure 1.5: **Deutsch-gate**.

Here,

$$\mathbf{R} = -i\mathbf{R}_x(\phi) = -ie^{i\frac{\phi}{2}\sigma_x} = (-i) \left(\cos\frac{\phi}{2} + i\sigma_x \sin\frac{\phi}{2} \right). \quad (1.14)$$

However, the **Deutsch-gate** can be *decomposed* into the two-qubit gates as the following

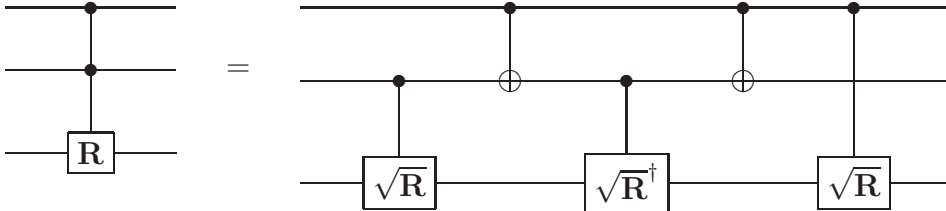


Figure 1.6: **Deutsch-gate** decomposition.

This decomposition distinguishes between the universality of quantum computation and reversible computation: in reversible computation, three-bit gates are

1.1 History of quantum computation

required for an universal gate, while in quantum computation, two-bit gates are adequate^[7].

1.1 History of quantum computation







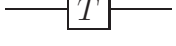
| Quantum gates on a single qubit | | |
|---------------------------------|--|---|
| Name | Matrix representation | Symbol |
| Identity | $\begin{pmatrix} 1 & 0 \\ 0 & 1 \end{pmatrix}$ |  |
| Hadamard | $\frac{1}{\sqrt{2}} \begin{pmatrix} 1 & 1 \\ 1 & -1 \end{pmatrix}$ |  |
| Pauli-X, σ_x | $\begin{pmatrix} 0 & 1 \\ 1 & 0 \end{pmatrix}$ |  |
| Pauli-Y, σ_y | $\begin{pmatrix} 0 & -i \\ i & 0 \end{pmatrix}$ |  |
| Pauli-Z, σ_z | $\begin{pmatrix} 1 & 0 \\ 0 & -1 \end{pmatrix}$ |  |
| Phase | $\begin{pmatrix} 1 & 0 \\ 0 & i \end{pmatrix}$ |  |
| $\frac{\pi}{8}$ | $\begin{pmatrix} 1 & 0 \\ 0 & e^{i\frac{\pi}{4}} \end{pmatrix}$ |  |

Table 1.1: Quantum logic gates of a single qubit.

1.1 History of quantum computation

| Dimensions | Quantum computation | Symbol |
|--------------------------|---------------------------------------|--|
| 2×2 | $\Lambda_0(U) x_0\rangle$ | $ x_0\rangle \text{ --- } \boxed{U} \text{ --- } x'_0\rangle$ |
| 4×4 | $\Lambda_1(U) x_0x_1\rangle$ | $ x_0\rangle \text{ --- } \bullet \text{ --- } x_0\rangle$ $ x_1\rangle \text{ --- } \boxed{U} \text{ --- } x'_1\rangle$ |
| 8×8 | $\Lambda_2(U) x_0x_1x_2\rangle$ | $ x_0\rangle \text{ --- } \bullet \text{ --- } x_0\rangle$ $ x_1\rangle \text{ --- } \bullet \text{ --- } x_1\rangle$ $ x_2\rangle \text{ --- } \boxed{U} \text{ --- } x'_2\rangle$ |
| ... | ... | ... |
| $2^{n+1} \times 2^{n+1}$ | $\Lambda_n(U) x_0, \dots, x_n\rangle$ | $ x_0\rangle \text{ --- } \bullet \text{ --- } x_0\rangle$ $ \dots\rangle \text{ --- } \boxed{\dots} \text{ --- } \dots\rangle$ $ x_n\rangle \text{ --- } \boxed{U} \text{ --- } x'_n\rangle$ |

Table 1.2: Quantum network notations.

$$|\psi\rangle = a_0|0\rangle + a_1|1\rangle \longrightarrow \boxed{\text{Measurement}} \longrightarrow \{|0\rangle, |1\rangle\}$$

Figure 1.7: Quantum measurement.

1.1.3 Quantum measurement

Unitary evolution in a quantum system occurs by assuming that the system is closed. When the observers measure the quantum system, it causes that the system is no longer closed, the evolution is no longer unitary, and the quantum state, $|\psi\rangle = \sum_{s=0}^1 a_s|s\rangle$, collapses into the classical state, $\{|0\rangle, |1\rangle\}$, as shown in Fig. (1.7).

A primitive way to explain the effect of *quantum measurement* is by introducing a set of measurement operators $\{\mathcal{M}_s\}$ which acts on the quantum system. Measurement operators, $\{\mathcal{M}_s\}$, are *idempotent matrices*; therefore, the operators fulfill the *completeness equation*

$$\sum_s \mathcal{M}_s^\dagger \mathcal{M}_s = I. \tag{1.15}$$

The new system state, which has already *collapsed* by measurement, is

$$|s\rangle = \frac{\mathcal{M}_s|\psi\rangle}{\sqrt{\langle\psi|\mathcal{M}_s^\dagger\mathcal{M}_s|\psi\rangle}}, \tag{1.16}$$

where the subscript “ s ” denotes the measurement outcomes; therefore the value is $s \in \{0, 1\}$. The probability of the measurement outcome, s , is

$$p(s) = \langle\psi|\mathcal{M}_s^\dagger\mathcal{M}_s|\psi\rangle. \tag{1.17}$$

“*Measurement*”, “*state space*”, and “*entanglement*” are the topics distinguishing quantum from classical physics. The facts that measurement outcomes of quantum system are classical and that the quantum system is composed by entangled state are the resource of quantum information science. By utilizing these two properties of quantum mechanics, one can gain the advantages of quantum information over classical information.

1.1 History of quantum computation

Equipped by the tools in quantum mechanics and reversible computation, quantum computation has proved that it can solve certain problems that cannot be solved by classical computation and provided new sights into the information theory.

1.1.4 Quantum logic gates and Schrödinger equation

The achievements in quantum computation^[18-21] and quantum information theory^[22] inspire experimentalists to realize a quantum computer which overwhelms Moore's Law^[23]. Realization of qubits spans from silicon^[24,25], photon^[26], trapped atoms, nuclear magnetic resonance, quantum dots, superconductors, to graphene^[27]. Conventional way to simulate quantum computers is by the use of Schrödinger equation^[28]. Below, Schrödinger equation for the case of nuclear magnetic resonance is briefly discussed.

Schrödinger equation reads

$$i\hbar \frac{\partial}{\partial t} |\Psi\rangle = \hat{\mathcal{H}} |\Psi\rangle, \quad (1.18)$$

where the general form of state $|\Psi\rangle$ is

$$|\Psi\rangle = c_0|0\rangle + c_1|1\rangle. \quad (1.19)$$

One can obtain the eigenfunction $|\Psi\rangle$ for the following Hamiltonian of magnetic interaction of a classical electromagnetic field with a two-state spin^[28]

$$\begin{aligned} \mathcal{H} &= -\vec{\mu} \cdot \vec{\mathcal{B}} \\ \mathcal{H} &= -\gamma \hbar \vec{\mathcal{S}} \cdot \vec{\mathcal{B}}, \end{aligned} \quad (1.20)$$

where γ is the gyromagnetic ratio, \hbar is reduced Planck constant, and $\vec{\mathcal{S}} = \mathcal{S}_x \hat{i} + \mathcal{S}_y \hat{j} + \mathcal{S}_z \hat{k}$ is a Pauli spin vector, where $\mathcal{S}_x = \frac{1}{2}(|0\rangle\langle 1| + |1\rangle\langle 0|)$, $\mathcal{S}_y = \frac{i}{2}(|0\rangle\langle 1| - |1\rangle\langle 0|)$, and $\mathcal{S}_z = \frac{1}{2}(|0\rangle\langle 0| - |1\rangle\langle 1|)$. The typical applied magnetic field $\vec{\mathcal{B}}$ is in the following form

$$\vec{\mathcal{B}} = \mathcal{B}_0(\hat{i}\cos(\omega t) - \hat{j}\sin(\omega t)) + \omega_0 \hat{k}, \quad (1.21)$$

1.1 History of quantum computation

where ω_0 is static and very large, while \mathcal{B}_0 is several orders of magnitude smaller than ω_0 in strength^[28]. The following notations hold;

$$\mathcal{B}_+ = \mathcal{B}_x + i\mathcal{B}_y = \mathcal{B}_0 e^{-i\omega t}, \quad (1.22a)$$

$$\mathcal{B}_- = \mathcal{B}_x - i\mathcal{B}_y = \mathcal{B}_0 e^{i\omega t}, \quad (1.22b)$$

$$\mathcal{S}_+ = \mathcal{S}_x + i\mathcal{S}_y = |0\rangle\langle 1|, \quad (1.22c)$$

$$\mathcal{S}_- = \mathcal{S}_x - i\mathcal{S}_y = |1\rangle\langle 0|. \quad (1.22d)$$

Therefore, it can be shown that the Schrödinger Hamiltonian of the system is

$$\mathcal{H} = -\gamma\hbar(\omega_0\mathcal{S}_z + \frac{1}{2}(\mathcal{B}_+\mathcal{S}_- + \mathcal{B}_-\mathcal{S}_+)). \quad (1.23)$$

If Eq. (1.21) is substituted into Eq. (1.23) followed by substitution into Eq. (1.18), one can find

$$i\frac{\partial(c_0|0\rangle + c_1|1\rangle)}{\partial t} = -\frac{\gamma}{2}((\omega_0 c_0(t) + \mathcal{B}_0 e^{i\omega t} c_1(t))|0\rangle + (\mathcal{B}_0 e^{-i\omega t} c_0(t) - \omega_0 c_1(t))|1\rangle). \quad (1.24)$$

The goal is to find the time evolution of the coefficient of the quantum state due to the magnetic field perturbation. To do so, the simplest way is by assuming $\omega = \frac{\gamma\omega_0}{2}$ and introducing $\Omega = \gamma\mathcal{B}_0$. It leads to

$$i\frac{\partial}{\partial t}(c_0(t)e^{-i\omega t}) = -\frac{\Omega}{2}c_1(t), \quad (1.25a)$$

$$i\frac{\partial}{\partial t}(c_1(t)e^{i\omega t}) = -\frac{\Omega}{2}c_0(t). \quad (1.25b)$$

The substitution of Eq. (1.25a) into Eq. (1.25b) or vice versa can generate the following linear homogeneous second-order ordinary differential equations^[29]

$$\ddot{c}_0 - i\omega\dot{c}_0 + \frac{\Omega^2}{4}c_0 = 0, \quad (1.26a)$$

$$\ddot{c}_1 + i\omega\dot{c}_1 + \frac{\Omega^2}{4}c_1 = 0. \quad (1.26b)$$

1.1 History of quantum computation

Therefore, the solutions of Eq. (1.26a) and Eq. (1.26b) which fulfill the normalization condition, $\sum_{i=0}^1 |c_i(0)|^2 = \sum_{i=0}^1 |c_i(t)|^2 = 1$, as mentioned in Eq. (1.3) are

$$\begin{pmatrix} c_0(t) \\ c_1(t) \end{pmatrix} = \begin{pmatrix} \cos\left(\frac{\xi t}{2}\right) & \sin\left(\frac{\xi t}{2}\right) \\ -\sin\left(\frac{\xi t}{2}\right) & \cos\left(\frac{\xi t}{2}\right) \end{pmatrix} \begin{pmatrix} c_0(0) \\ c_1(0) \end{pmatrix}. \quad (1.27)$$

where $\xi = \omega + \Omega\sqrt{\left(\frac{\omega}{\Omega}\right)^2 + 1}$. The quantum gates on a single qubit can be obtained by setting the frequency $\{\xi\}$: the **Identity**-gate can be performed if $t = \frac{4\pi n}{\xi}$, where $\{n = 0, 1, 2, \dots, N | N \in \mathfrak{R}\}$, while the **NOT**-gate can be obtained when $t = \frac{\pi}{\xi}$ or *so-called* π -pulse, with a phase factor of “-1” on $|1\rangle$.

As has been shown above for the case of one qubit, quantum computation proceeds with Schrödinger equation. However, computation with Schrödinger equation poses several challenges: *first*, one should solve exponential numbers of differential equations due to the increase number of qubits: n -qubits mean there are 2^n of differential equations which have to be solved^[28]. Usually, approximations are used to solve the problems, but there are physical phenomena that can not be explained by approximations. *Second*, Schrödinger equation fails if relativistic effect is taken into account; in this point, Dirac equation should be considered. Nevertheless, a growing interest to expand the application of Dirac equation beyond the case of quantum relativistic, which is *so-called supersymmetric quantum mechanics (SUSY QM)*^[30], is noticed. Nieto *et. al* showed that every property of a differential intertwiner for Schrödinger equation acquires its counterpart in the case of the Dirac equation^[31]. Two-dimensional (2D) Dirac equation is widely known to describe quantum relativistic; however, the application of 1D Dirac equation, in which uses Pauli spin matrices ($\sigma_1, \sigma_2, \sigma_3$) instead of Dirac matrices, is still unclear. The recent study shows that it can be used to explain nonrelativistic system such as conjugated molecules^[32].

Schrödinger and Dirac equations have the similarity that they can be transformed under Darboux transformations. The transformations has been widely used in enormous types of Schrödinger equation; however, previous applications of Darboux transformations on Dirac equations and especially in the area of quantum computation are rather limited.

1.2 Abstract quantum computation

The next problem is the physical realization of quantum computer. The implementation of quantum information processing must satisfy five criteria and two additional criteria for quantum communication which is *so-called the DiVincenzo criteria*^[33]. In general, recent simulations of quantum computers are based in the following two types of abstract quantum systems:

1. Non-nearest neighbor quantum computer (Fig. 1.8(a)),
2. Nearest neighbor quantum computer (Fig. 1.8(b)).

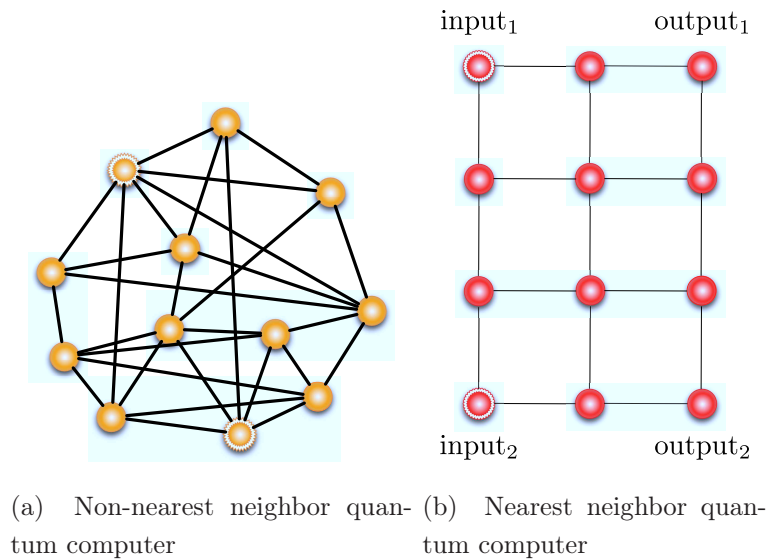


Figure 1.8: Comparison between non- and nearest neighbor quantum computers. The yellow and red balls represent the qubits. The lines between the qubits express the communications which are allowed.

In non-nearest neighbor architecture of abstract quantum computation, as shown in Fig. (1.8(a)), all qubits are programmed so that they can be arbitrarily connected by one another regardless the distance and order. Therefore it is allowed under this scheme, as shown in Fig. (1.3), that a qubit can communicate to non-adjacent qubit by skipping over the nearest neighbor qubits in order to perform unitary operations.

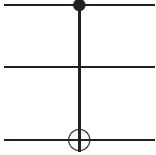
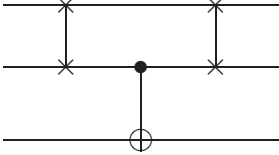
| Non-nearest neighbor | Nearest neighbor |
|---|--|
|  |  |

Table 1.3: Comparison between non- and nearest neighbor quantum computations.

In contrast, as illustrated in Fig. (1.8(b)), in nearest neighbor quantum computation, the distance and order of qubits are arranged in a certain manner. If the quantum circuit is restricted by adjacent computation only, meaning that the quantum information is propagated by nearest neighbor qubits, it will cost more depth and space of a quantum circuit, as illustrated in Fig (1.3). This kind of proposal of quantum computer class which is scalable in the nature may rely on a quantum system consisting of arrays of weakly coupled qubits^[34] as shown in Fig. (1.8). One of promising which fulfills this model is *so-called measurement-based quantum computation (MBQC)* and it is extensively discussed in the next Section.

1.3 Measurement-based quantum computation

A one-dimensional cluster state is in the form of

$$|\Phi_N\rangle = \frac{1}{2^{\frac{N}{2}}} \bigotimes_{a=1}^N (|0\rangle_a \sigma_\gamma^{(a+1)} + |1\rangle_a), \quad (1.28)$$

where $\sigma_\gamma^{(i)}$ is the Pauli operator operating on qubit i in the N -qubit cluster \mathcal{C} , a is the index of a qubit in cluster \mathcal{C} and γ which can be x , y , or z depending on the choice of interaction Hamiltonian between neighbors^[35] and with the convention $\sigma_\gamma^{N+1} = 1$. In general, the cluster state should obey the quantum correlation equation

$$\bigotimes_{\alpha,v} \sigma_v^{(\alpha)} |\Phi_{\{k\}}\rangle_{\mathcal{C}} = (-1)^{k_\alpha} |\Phi_{\{k\}}\rangle_{\mathcal{C}}, \quad (1.29)$$

where $\alpha = a, \{a + n | (a + n) \in \text{neighbors}\}$, $v = 0, x, y, z$, and $k_\alpha = \{0, 1\}$. The parameter $\{k\}$ is a set of index parameters specifying the cluster state. $|\Phi_{\{k\}}\rangle_{\mathcal{C}}$ expresses the cluster state before the measurement and $|\Psi_{\{k\}}\rangle_{\mathcal{C}(g)}$ represents the cluster state after a set of measurements in which a quantum gate g has been simulated on the cluster state.

The cluster state can be created in several ways, e.g., initializing every qubit to the $|+\rangle$ state and performing a Controlled-Z gate between each neighboring pair. With such a cluster state, Raussendorf *et al.* showed that a carefully chosen measurement pattern could impose any quantum gates on logical qubits.

Suppose we have an initial set of cluster state eigenvalue equations, $|\Phi_{\{k\}}\rangle_{\mathcal{C}}$, representing the cluster which is the union of the input cluster (\mathcal{C}_{input}), the machine cluster, ($\mathcal{C}_{machine}$) and the output cluster (\mathcal{C}_{output}). All of the qubits except the output cluster are measured by the projective measurement operators \mathcal{P} with certain measurement patterns \mathcal{M} , $\mathcal{P}_{\{s\}}^{(\mathcal{C})}(\mathcal{M}) = \bigotimes_{k \in \mathcal{C}} \frac{1 + (-1)^{k_a} \vec{r}_k \cdot \vec{\sigma}^{(k)}}{2}$, where the subscript $\{s\} \in \{0, 1\}$ denotes the measurement outcomes and the superscript $\{\mathcal{C}\}$ denotes that these sets of measurement acting upon the cluster states. The new m -qubits output register of the quantum logic network is the cluster state $|\Psi_{\{k\}}\rangle_{\mathcal{C}(g)}$ obeying $2m$ new eigenvalue equations:

$$\sigma_x^{(\mathcal{C}_{input}(g),i)} (U \sigma_x^{(i)} U^\dagger)^{(\mathcal{C}_{output}(g))} |\psi\rangle_{\mathcal{C}(g)} = (-1)^{\lambda_{x,i}} |\psi\rangle_{\mathcal{C}(g)} \quad (1.30)$$

1.3 Measurement-based quantum computation

$$\sigma_z^{(\mathcal{C}_{input}(g)^i)} (U \sigma_z^{(i)} U^\dagger)^{(\mathcal{C}_{output}(g))} |\psi\rangle_{\mathcal{C}(g)} = (-1)^{\lambda_{z,i}} |\psi\rangle_{\mathcal{C}(g)}, \quad (1.31)$$

where $\lambda_{x,i}, \lambda_{z,i} \in \{0, 1\}$ are the measurement outcomes.

Quantum computation in Pauli algebra form implicitly appears in the final set of eigenvalue equations after the measurements. A brief review is given in Subsection (1.3.1).

Several remarkable properties are follows^[36,37]:

- Measurement of qubits in the machine cluster in the σ_z -eigenbasis removes them from the main cluster and *disconnects* all of their bonds.
- Measurement of qubits in the machine cluster in the σ_x -eigenbasis removes them from the main cluster and creates *Bell pairs* between the qubits in the input cluster and the qubits in the output cluster.
- Measurement of qubits in the machine cluster in the σ_y -eigenbasis removes them from the main cluster and leaves an entangled state between the qubits in the input cluster and the qubits in the output cluster.

The measurement calculus is a convenient formalism for representing MBQC quantum gates^[38,39]. Danos *et al.* showed how to write an MBQC quantum gate \mathcal{U} in the form $\mathcal{U} := (\{\text{Resources}\}, \{\text{Input}\}, \{\text{Output}\}, \{\text{EMC}\})_{\mathcal{U}}$. Based on this definition, we introduce a notation $\mathcal{U}^{<n>}$ meaning a quantum gate in MBQC using n qubits. $\mathcal{CNOJ}^{<4>}$ refers to $\mathcal{CNOJ}^{<4>} := (\{1, 2, 3, 4\}, \{1, 4\}, \{3, 4\}, \{X_4^{s_3} Z_4^{s_2} Z_1^{s_2} M_3^x M_2^x E_{13} E_{23} E_{34}\})$. A fifteen-qubit form of the gates is

$$\begin{aligned} \mathcal{CNOJ}^{<15>} &= (\{\text{Resources}\}, \{\text{Input}\}, \{\text{Output}\}, \{\text{EMC}\})_{\mathcal{CNOJ}^{<15>}} \quad (1.32) \\ &:= (\{1, \dots, 15\}, \{1, 9\}, \{7, 15\}, \{\text{EMC}\})_{\mathcal{CNOJ}^{<15>}} \end{aligned}$$

as mentioned in Ref.^[21]. Recently, two types of Toffoli gate have been developed: $\mathcal{CCNOJ}^{<54>}$ ^[21] and $\mathcal{CCNOJ}^{<39>}$ ^[39]. Both Toffoli gates have similar numbers of adaptive measurements, but different numbers of qubit resources. $\mathcal{CCNOJ}^{<39>}$ must be connected into an arbitrary graph, while $\mathcal{CCNOJ}^{<54>}$ is appropriate for the Manhattan geometry cluster state. $\mathcal{CCNOJ}^{<54>}$ is illustrated in Fig. (1.10) in Subsection (1.3.1).

1.3 Measurement-based quantum computation

The physical implementation of MBQC requires a lattice system with an Ising-like interaction between qubits so that the quantum information can be propagated in the lattice due to measurements. Several physical implementations have been proposed; Meier *et al.* proposed the possibility of experimental realization to perform initialization, quantum gate operation and read-out in antiferromagnetic spin cluster quantum computing^[40]. Devitt *et al.* have described an all-optical implementation where the required number of photonic modules and chips only depends on the cross section length of the two-dimensional lattice (corresponding to the y -axis in our figures)^[41,42].

MBQC runs in two phases: preparation of the cluster state and measurement. Because the preparation step is completely generic, failure in coupling the qubits is not a problem. Mechanisms that succeed only probabilistically can be used, as long as failures are heralded, making optical QC suitable for MBQC.^[43]

1.3.1 MBQC gates and graphical notation

To illustrate MBQC, we detail the operation of the NOT gate, as shown in Fig. (1.9). In this Subsection we adopt the graphical notation first proposed by Raussendorf, Browne, and Briegel^[21]. The cluster contains 5 qubits where \mathcal{C}_{input} is qubit 1, $\mathcal{C}_{machine}$ is qubits 2, 3 and 4 and \mathcal{C}_{output} is qubit 5. We begin from the cluster state eigenvalue equations for 5 qubits:

$$\sigma_x^{(1)} \sigma_z^{(2)} |\phi\rangle_{\mathcal{C}(\mathbf{NOT})} = |\phi\rangle_{\mathcal{C}(\mathbf{NOT})} \quad (1.33)$$

$$\sigma_z^{(1)} \sigma_x^{(2)} \sigma_z^{(3)} |\phi\rangle_{\mathcal{C}(\mathbf{NOT})} = |\phi\rangle_{\mathcal{C}(\mathbf{NOT})} \quad (1.34)$$

$$\sigma_z^{(1)} \sigma_z^{(2)} \sigma_x^{(3)} \sigma_z^{(4)} |\phi\rangle_{\mathcal{C}(\mathbf{NOT})} = |\phi\rangle_{\mathcal{C}(\mathbf{NOT})} \quad (1.35)$$

$$\sigma_z^{(3)} \sigma_x^{(4)} \sigma_z^{(5)} |\phi\rangle_{\mathcal{C}(\mathbf{NOT})} = |\phi\rangle_{\mathcal{C}(\mathbf{NOT})} \quad (1.36)$$

$$\sigma_z^{(1)} \sigma_z^{(4)} \sigma_x^{(5)} |\phi\rangle_{\mathcal{C}(\mathbf{NOT})} = |\phi\rangle_{\mathcal{C}(\mathbf{NOT})} \quad (1.37)$$

1.3 Measurement-based quantum computation



Figure 1.9: NOT gate in MBQC. The input qubit and all pink qubits are measured in the σ_x -eigenbasis and the framed-green qubit is measured in an adaptive basis depending on the measurement outcome of qubit 2. A rotation measurement operator on xy -plane around z -axis with angle π on qubit 3 makes the qubit 3 not adaptive.

After obtaining the quantum correlation of the cluster state, two measurement steps are performed: *first*, the σ_x measurement on qubit 2 and qubit 4,

$$|\phi\rangle_{\mathcal{C}(\mathbf{NOT})} = \mathcal{P}_{x,s_2}^{(2)} \mathcal{P}_{x,s_4}^{(4)} |\phi\rangle_{\mathcal{C}(\mathbf{NOT})}. \quad (1.38)$$

This first measurement converts the initial quantum correlation to the eigenvalue equations:

$$\sigma_x^{(1)} \sigma_x^{(3)} \sigma_x^{(5)} |\phi\rangle_{\mathcal{C}(\mathbf{NOT})} = |\phi\rangle_{\mathcal{C}(\mathbf{NOT})} \quad (1.39)$$

$$\sigma_z^{(1)} \sigma_z^{(3)} |\phi\rangle_{\mathcal{C}(\mathbf{NOT})} = (-1)^{s_2} |\phi\rangle_{\mathcal{C}(\mathbf{NOT})} \quad (1.40)$$

$$\sigma_z^{(3)} \sigma_z^{(5)} |\phi\rangle_{\mathcal{C}(\mathbf{NOT})} = (-1)^{s_4} |\phi\rangle_{\mathcal{C}(\mathbf{NOT})}. \quad (1.41)$$

Furthermore, the eigenbasis of $\vec{r}_{xy}((-1)^{s_2}(-\eta)) \cdot \vec{\sigma}$, where $\vec{r}_{xy} \cdot \vec{\sigma} = \cos(\eta) \sigma_x + \sin(\eta) \sigma_y$, is chosen as the measurement basis on qubit 3 to realize the operation **NOT** by measurement pattern $\mathcal{M}(\mathbf{NOT})$. Mathematically, it can be expressed by:

$$|\psi\rangle_{\mathcal{C}(\mathbf{NOT})} = \mathcal{P}_{xy(\eta)}^{(3)} |\phi\rangle_{\mathcal{C}(\mathbf{NOT})}, \quad (1.42)$$

where $\mathcal{P}_{xy(\eta)}^{(3)} = \frac{1 + (-1)^{s_3} \vec{r}_k \cdot \vec{\sigma}^{(k)}}{2}$. This second measurement generates two eigenvalue equations from Eqs. (1.39), (1.40) and (1.41), which obey *Theorem 1* of Raussendorf et. al:

$$\sigma_x^{(1)} U^{(5)}[-\eta] \sigma_x^{(5)} U^{(5)\dagger}[\eta] |\psi\rangle_{\mathcal{C}(\mathbf{NOT})} = |\psi\rangle_{\mathcal{C}(\mathbf{NOT})} \quad (1.43)$$

1.3 Measurement-based quantum computation

$$\sigma_z^{(1)} U^{(5)} [-\eta] \sigma_z^{(5)} U^{(5)\dagger} [\eta] |\psi\rangle_{\mathcal{C}(\text{NOT})} = (-1)^{s_2+s_4} |\psi\rangle_{\mathcal{C}(\text{NOT})}. \quad (1.44)$$

By choosing $\eta = \pi$, these equations give a NOT-gate. This method can be broadened to perform quantum gates on a large-scale cluster state system. Similar to the work of Leung^[44], quantum computation can be achieved in cluster states depending on choice of measurement patterns.

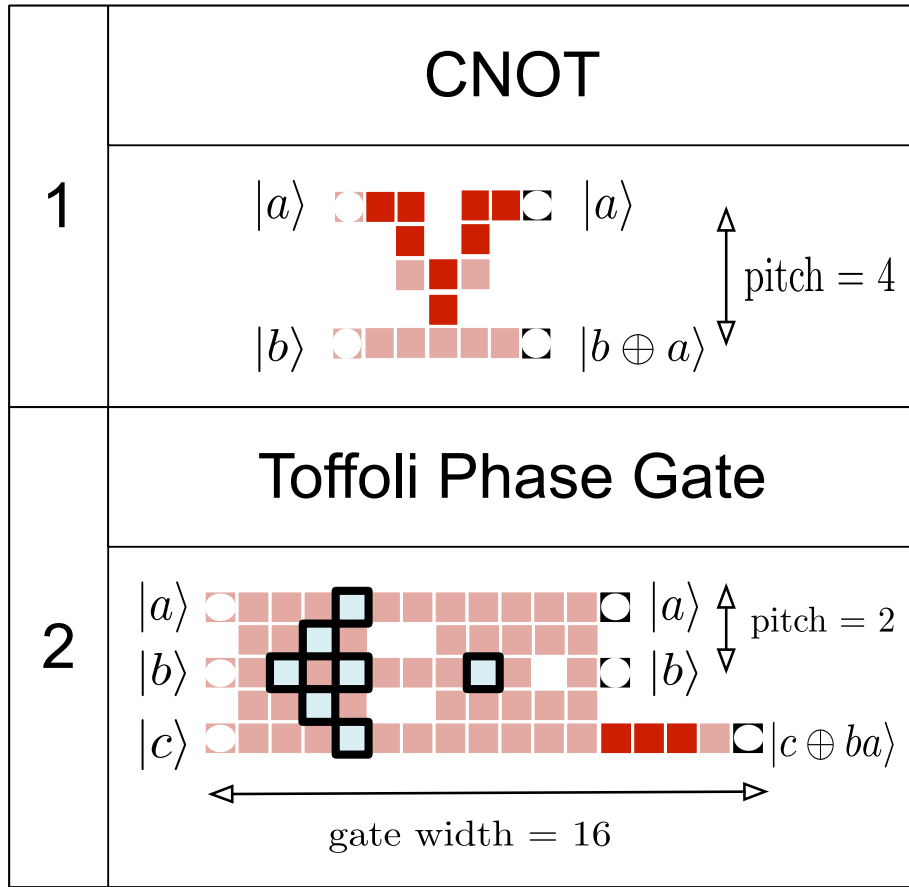


Figure 1.10: Quantum gates in measurement-based quantum computation. Due to the relationship between CCNOT and Toffoli Phase Gate (TPG), $\text{CCNOT} = H_t(\text{TPG})H_t^\dagger$, the target qubit can be chosen arbitrarily by putting a Hadamard gate on the chosen qubit. The Toffoli phase gate is $\text{CCNOT}^{<54>}$.

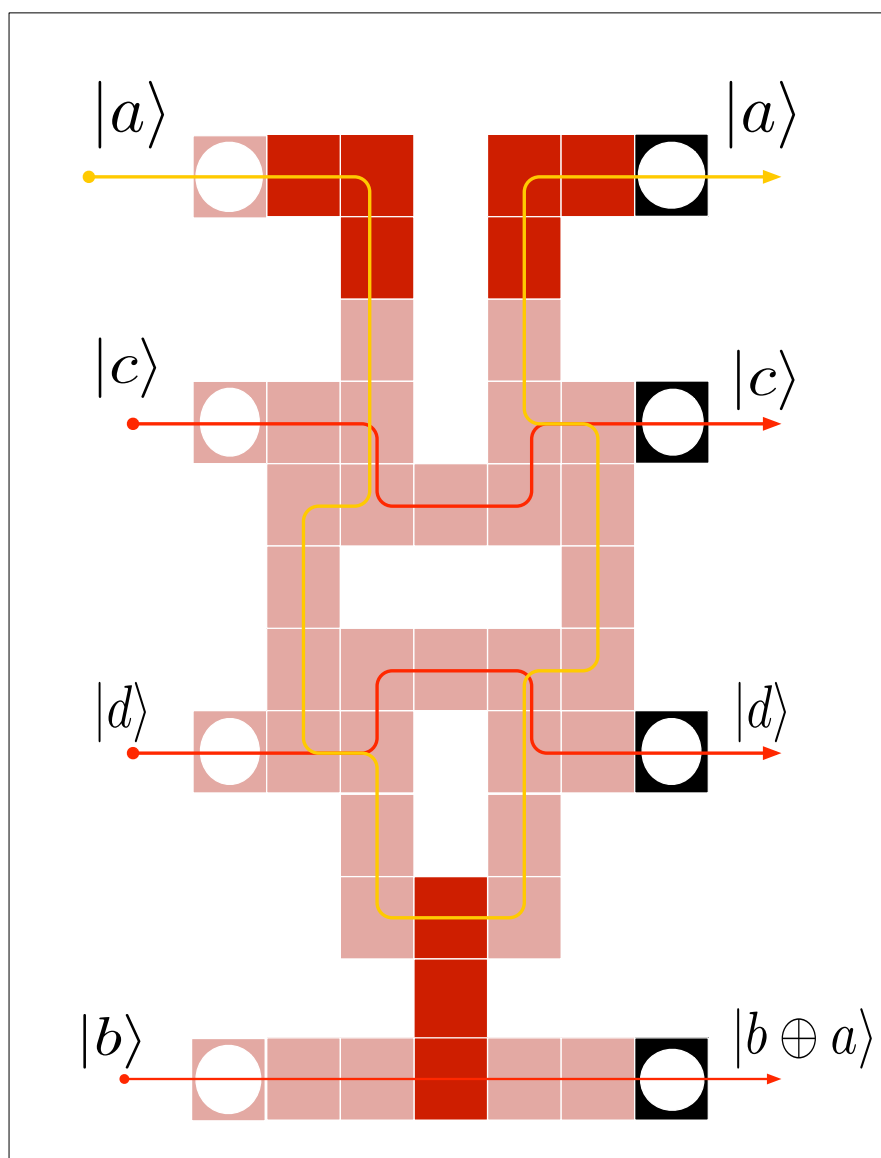


Figure 1.11: Non-adjacent computation. The implementation of four types SWAP gates to propagate the information up-to-down of non-adjacent qubits for performing CNOT. Qubit $|a\rangle$ acts as the control qubit and $|b\rangle$ is the target qubit.

Generally, every quantum gate contains C_l lattice qubits with m measurements, C_w width, and C_h height. In this dissertation, we will use a quantum gates model of Raussendorf *et al.*^[21]. As shown in Fig. (1.10) and Fig. (1.11), CNOT and the Toffoli Phase gate can be performed using measurement on 15 and 54 cluster qubits, respectively.

1.4 Darboux transformations

In 1882, Gaston Darboux introduced a method to solve Sturm-Liouville differential equation, which is called Darboux transformation afterwards^[45]. Remarkably, this transformation can solve not only Sturm-Liouville differential equation (another form of time-independent Schrödinger equation), but also the other forms of linear and non-linear differential equations, such as Korteweg-de Vries, Kadomtsev-Petviashvili, Sine-Gordon, and Non-linear Schrödinger equations. The following Section explains about Darboux transformation and its generalized form called Crum's theorem on Sturm-Liouville differential equation.

1.4.1 Darboux transformation and Crum theorem

Consider following Sturm-Liouville differential equation

$$-\psi_{xx} + u\psi = \lambda\psi \quad (1.45)$$

where u is function of x and λ is a constant. In the Schrödinger equation, u represents a potential. Darboux transformation is defined as follow^[45]

$$\begin{aligned} \psi[1] &= \left(\frac{d}{dx} - \sigma_1 \right) \psi = \psi_x - \frac{\psi_{1x}}{\psi_1} \psi \\ &= \frac{\psi_x \psi_1 - \psi_{1x} \psi}{\psi_1} = \frac{W(\psi_1, \psi)}{W(\psi_1)}. \end{aligned} \quad (1.46)$$

$W(\psi_1, \psi)$ expresses Wronskian determinant as defined below

$$W(\psi_1, \psi_2, \dots, \psi_N) = \begin{vmatrix} \psi_1 & \psi_2 & \dots & \psi_N \\ \psi_1^{(1)} & \psi_2^{(1)} & \dots & \psi_N^{(1)} \\ \dots & \dots & \dots & \dots \\ \psi_1^{(N-1)} & \psi_2^{(N-1)} & \dots & \psi_N^{(N-1)} \end{vmatrix} \quad (1.47)$$

where $\psi^{(n)}$ means ψ derivative for n -times and ψ_1 is the solution of ψ for $\lambda = \lambda_1$. If ψ is a solution, $\psi[1]$ is the solution for the following Sturm-Liouville differential equation then

$$-\psi_{xx}[1] + u[1]\psi[1] = \lambda\psi[1] \quad (1.48)$$

where $u[1]$ is a new function of u which has been transformed. It will be shown below that Darboux transformation acting on $\psi[1]$ influences the potential u , if $\psi[1]$ is invariant over Eq. (1.48).

From Eq.(1.46), one can obtain following relation

$$-\psi_{xx}[1] = -\psi_{xxx} + \sigma_{1xx}\psi + 2\sigma_{1x}\psi_x + \sigma_1\psi_{xx}. \quad (1.49)$$

Substitution of Eq.(1.46) and Eq.(1.49) into Eq.(1.48) results in

$$\begin{aligned} -\psi_{xxx} + \sigma_{1xx}\psi + 2\sigma_{1x}\psi_x + \sigma_1\psi_{xx} + u[1](\psi_x - \sigma_1\psi) \\ = \lambda(\psi_x - \sigma_1\psi). \end{aligned} \quad (1.50)$$

Using Eq.(1.45) to substitute ψ_{xx} results in

$$\begin{aligned} (u[1] - u + 2\sigma_{1x})\psi_x + \\ (-u_x + \sigma_{1xx} + \sigma_1u - \sigma_1u[1])\psi = 0. \end{aligned} \quad (1.51)$$

It is clear from Eq.(1.51), the following relations can be obtained

$$u[1] = u - 2\sigma_{1x} \quad (1.52)$$

$$\sigma_{1xx} - u_x + 2\sigma_1\sigma_{1x} = 0. \quad (1.53)$$

The Eq.(1.49) shows that the function u is also transformed due to ψ in Eq.(1.45). In other words, Sturm-Liouville equation in Eq.(1.45) is covariant under Darboux transformation action

$$\{u, \psi\} \rightarrow \{u[1], \psi[1]\}.$$

Interestingly, Darboux transformation can be recursively applied to Sturm-Liouville equation solution and consequently the potential is transformed to ensure that the solution belongs to the equation. Below will discuss the consequence if the solution in Eq.(1.45) is acted by Darboux transformation twice.

$$\psi[2] = \left(\frac{d}{dx} - \frac{\psi_{2x}[1]}{\psi_2[1]} \right) \left(\frac{d}{dx} - \frac{\psi_{1x}}{\psi_1} \right) \psi \quad (1.54)$$

1.4 Darboux transformations

where

$$\psi[2] = \psi_{2x} - \frac{\psi_{1x}}{\psi_1} \psi_2. \quad (1.55)$$

From the definition $\psi[1]$ and $\psi[2]$, $u[1]$, and $u[2]$, Crum proposed general form of Darboux transformation in the following form

$$\psi[N] = \frac{W(\psi_1, \dots, \psi_N, \psi)}{W(\psi_1, \dots, \psi_N)} \quad (1.56a)$$

$$u[N] = u - 2 \frac{\partial^2}{\partial x^2} \ln W(\psi_1, \dots, \psi_N) \quad (1.56b)$$

where $\psi[N]$ satisfies the equation

$$-\psi_{xx}[N] + u[N]\psi[N] = \lambda\psi[N]. \quad (1.57)$$

The Crum's theorem is based on the fact that Darboux transform acting N -times on a function can be written

$$\psi[N] = D[N]\psi = \psi^{(N)} + s_1\psi^{(N-1)} + \dots + s_N\psi. \quad (1.58)$$

Ansatz of Crum's theorem is that s_N is obtained from the following relation

$$\sum_{k=1}^N s_k \psi_j^{(N-k)} = -\psi_j^{(N)} \quad (1.59)$$

where $j=1, 2, \dots, N$. Eq. (1.59) can be explained and arranged in matrix representation by following

$$\begin{pmatrix} \psi_1^{(N-1)} & \psi_1^{(N-2)} & \dots & \psi_1 \\ \dots & \dots & \dots & \dots \\ \dots & \dots & \dots & \dots \\ \psi_N^{(N-1)} & \psi_N^{(N-2)} & \dots & \psi_N \end{pmatrix} \begin{pmatrix} s_1 \\ s_2 \\ \dots \\ s_N \end{pmatrix} = \begin{pmatrix} -\psi_1^{(N)} \\ -\psi_2^{(N)} \\ \dots \\ -\psi_N^{(N)} \end{pmatrix}. \quad (1.60)$$

By the use of Cramer's rule, one can obtain s_j for $j = 1, \dots, N$. For instance, s_1

$$s_1 = \frac{\begin{vmatrix} -\psi_1^N & \psi_1^{(N-2)} & \psi_1^{(N-3)} & \dots & \psi_1 \\ \dots & \dots & \dots & \dots & \dots \\ \dots & \dots & \dots & \dots & \dots \\ -\psi_N^N & \psi_N^{(N-2)} & \psi_N^{(N-3)} & \dots & \psi_N \end{vmatrix}}{\begin{vmatrix} \psi_1^{(N-1)} & \dots & \dots & \psi_1 \\ \dots & \dots & \dots & \dots \\ \dots & \dots & \dots & \dots \\ \psi_N^{(N-1)} & \dots & \dots & \psi_N \end{vmatrix}}$$

Since it was coined by Darboux about a century ago, it has been successfully applied in enormous types of differential equations. One of famous applications is in solving nonlinear Schrödinger equations in which it can be shown that nonlinear refractive index in fiber optics materials, which have Kerr-like medium characteristics, will compensate for the dispersive effect of electromagnetic wave propagating. The nonlinear evolution equation of electromagnetic wave due to the both effects can be solved by Darboux transformations^[46]. The advantage of Darboux transformation is that one can obtain multisoliton solution from a trivial solution. This transformation has the similar form with the other methods which is used to solve nonlinear differential equations, i.e. Cole-Hopf transformations.

1.5 Problem definition

Recently, the physical realization of MBQC is the issue that is still unclear. The MBQC requires not only the five criteria and two additional criteria for quantum communication of the DiVincenzo criteria^[33], but also requires the measurement schemes on a specific physical system implementing the quantum computation on the cluster state.

On the other side, the various types of *abstract* quantum computation implementation by cavity QED, such as the atoms^[47] or the light^[48] as the qubit, have been proposed. Scenarios of how to generate cluster states of cavity QED have been proposed in many efforts^[49-51]. However, the complete implementation of MBQC by the use of cavity QED which satisfies the Divincenzo criteria is rarely discussed^[52].

1.6 Contributions of this thesis

This thesis aims to contribute to the advancement of theory towards implementation of measurement-based quantum computers. Specifically, two issues are discussed in this dissertation: control of qubit coherence in order to prepare cluster states in cavity quantum electrodynamics and efficient circuits to perform carry-lookahead adder in cluster states. The first contribution may meet with the implementation of the DiVincenzo's second criterion of MBQC in cavity QED,

while the second one may contribute to the implementation of the measurement-based quantum computer in engineering field.

Following a previous proposal of a measurement-based quantum computer being constructed by the use of classical electromagnetic field to entangle qubits^[50], control of qubit level occupancies in a cavity quantum electrodynamics by the use of classical electromagnetic field is proposed. Related to the preparation of cluster states in cavity QED, there are already similar proposals^[53]. However, in the previous work, the analysis of atomic inversion in the context of cluster state preparation in cavity QED was not mentioned. It is discussed extensively in this thesis. For a measurement-based quantum computers consisting of a large number of qubits, an architecture covering the circuit design and qubit resources are discussed.

Therefore, the contribution of this thesis is two fold: *firstly*, this thesis proposes the DiVincenzo's second criterion of MBQC in cluster states by the classical field emission into the cavity QED. *Secondly*, the thesis also provides the circuit design and resource evaluation of a MBQC circuits consisting of a large number of qubits.

In Chapter (2), cavity quantum electrodynamics is represented in one-dimensional Dirac equation. Darboux transformations represent the perturbation on the system by introduction of *extra* classical electromagnetic fields into the cavity. It is shown in this chapter that the classical mechanics of electromagnetic fields can control the atomic inversion of cavity quantum electrodynamics. This method may contribute to the method for cluster state preparation and ensuring the coherency of qubit in the cluster state.

The design of quantum circuit based on classical measurements over cluster states is provided in the Chapter (3). It is presented in the Chapter that by the use of the method, the size and the depth of quantum circuit can be optimized.

Chapter 2

Correlation of Dirac potentials and atomic inversion in cavity quantum electrodynamics

2.1 Cavity quantum electrodynamics

Cavity quantum electrodynamics (QED), as illustrated in Fig. (2.1), is the study of the interaction between the two-level atoms and the electromagnetic field inside a small high finesse optical cavity. The conventional way to physically realize the cavity QED is by a Fabry-Perot cavity and Rydberg atoms, such as Alkali^[54]. The Fabry-Perot cavity consists of two plane parallel mirrors which partially reflects and also partially transmits the incident light into the cavity. Due to the cavity is high finesse, the light inside the cavity bounces back and forth between the silvered mirrors, therefore the light can interact several times with the atom; as the consequence, the transition of the atom can be driven by pulses of light^[7,28].

Rabi oscillations are the important features in the cavity QED and play a pivot role in the field of experimental quantum information, since the oscillations represent the coherence and decoherence of the qubits in various types of physical schemes of quantum computers^[55–58].

The Rabi oscillations are derived from the quantity associated as the atomic inversion, $W(t)$, defined as the variation in the excited- and ground-state popu-

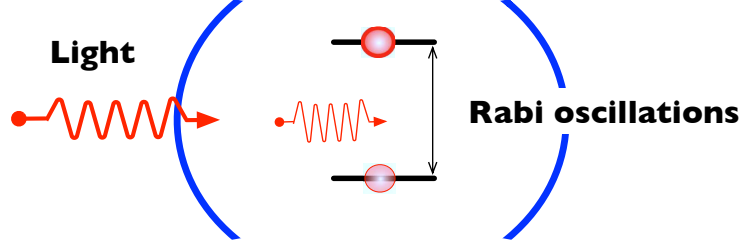


Figure 2.1: Cavity QED.

lations^[59]

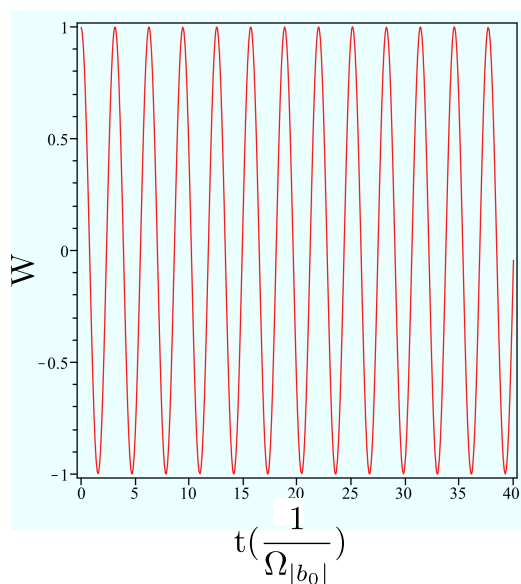
$$W(t) = P_e(t) - P_g(t). \quad (2.1)$$

When the electromagnetic field is classical, the oscillations in atomic inversion have constant amplitude. If the field is quantum, the oscillations consist of a sequence of collapses and revivals. The objective of the control of the time evolution of the population of two states in cavity is to formulate the Hamiltonian H , which represent the states of excited- and ground-levels^[54].

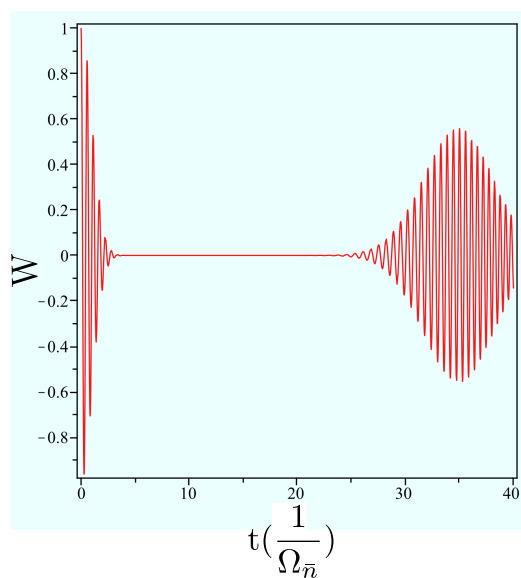
Following Ref. ^[59,60], the system of a two level atom and field in a single cavity mode, when the electromagnetic field is classical, is represented by $H = \hbar\omega_0 \frac{\sigma_z}{2} + \hbar\Omega[\sigma^+ b(t) + \sigma^- b(t)^\dagger]$ where $b(t) = b_0 e^{-i\omega t}$. Here, the Rabi frequency is $\Omega_{|b_0|} = \sqrt{\Omega^2(\kappa^2 + b_0^\dagger b_0)}$. One also can obtain the atomic inversion as illustrated in Fig. (2.2(a)) if the field is assumed classical by $W(t) = 1 - 2\Omega^2(b_0^\dagger b_0) \frac{\sin^2(\Omega_{|b_0|} t)}{\Omega_{|b_0|}^2}$.

When the electromagnetic field is quantum, the Hamiltonian is $H = \hbar\omega_0 \frac{\sigma_z}{2} + \hbar\omega \mathcal{B}^\dagger \mathcal{B} + \hbar\Omega[\sigma^+ \mathcal{B} + \sigma^- \mathcal{B}^\dagger]$, where \mathcal{B} (\mathcal{B}^\dagger) is an annihilation (creation) operator.

It is shown that the atomic inversion of Jaynes-Cummings Hamiltonian is represented by $W(t) = \frac{\langle \gamma, \uparrow | \sigma_z(t) | \gamma, \uparrow \rangle}{\langle \gamma, \downarrow | \sigma_z(0) | \gamma, \downarrow \rangle} = e^{-|\gamma|^2} \sum_{n=0}^{\infty} \frac{|\gamma|^{2n}}{n!} \left(1 - 2\Omega^2(n+1) \frac{\sin^2(\Omega_n t)}{\Omega_n^2} \right)$, where $\Omega_n = \sqrt{\Omega^2(\kappa^2 + n + 1)}$ is the Rabi frequency, $\kappa = \frac{\Delta}{2\Omega}$, in which Ω is the coupling constant atom-field interaction, $|\gamma|^2$ is the average photon number (\bar{n}), and $\Delta = \omega_0 - \omega$ is the detuning, i.e., resonant condition between atomic transition- and field frequency. The time unit of atomic inversion depends on the



(a) Semiclassical Rabi oscillations.



(b) Quantum Rabi oscillations for $\bar{n} = 30$.

Figure 2.2: Comparison between semiclassical and quantum Rabi oscillations on resonance ($\Delta = 0$).

physical system, because the *Rabi cycle* period of the two-level system, which is

the time needed for one-cycle process for an atom (or other two-level system) to absorb photons so the excitation occurs, and followed by the stimulated emission to re-emit the photons during the relaxation of the atom to the ground state, differs from one system to another system¹. In general case, the time unit for atomic inversion is $\frac{1}{\Omega_{Rf}}$, since its periodicity is $(\frac{\pi}{\Omega_{Rf}})$, where Ω_{Rf} is the Rabi frequency². In this Chapter, we restrict the cavity system in the non-resonant condition and is a bad cavity, i.e., the atom-field coupling constant is weaker than the decay rate, by the use³ of $\Delta = 2\sqrt{2}$, and $\Omega=1$. Since in recent experiment the quantum effect in cavity can be realized in the small number of photon, here we use $\bar{n} = |\gamma|^2=30$. The atomic inversion under this scheme is given in Fig. (2.2(b)); as can be clearly seen that this kind of atomic inversion consists of sequence of oscillations and collapses. The initial oscillations are caused by the absorption of the quantum light by the atom, while the collapses are due to the emissions of the light by the atom.

2.2 Problem definition

Recent research on quantum theory scrutinizes the reconciliation between quantum and classical physics, and it attempts to take the advantages from the classical side for constructing new theories^[62]. For instance, the quantum teleportation between sender and receiver involves classical information transmission based on the joint measurement of EPR pair^[63]. In experimental research on quantum information, notions of Coulomb and photon blockades represent the influence of classical physics on quantum physics^[64,65]. Here, we show that concurrent condition of the electromagnetic field behaving classically and quantumly in cavity

¹In the recent achievement of microwave cavity quantum electrodynamics^[61], the atomic transition (ω_0) and field (ω) frequencies units are in order of GHz, while the Rabi oscillations unit is in order of μs .

²The time unit for the classical Rabi oscillation is $\frac{1}{\Omega_{|b_0|}}$ and the time unit for the quantum Rabi oscillation is $\frac{1}{\Omega_{\bar{n}}}$, where $\Omega_{\bar{n}} = \sqrt{\Omega^2(\kappa^2 + \bar{n} + 1)}$. Therefore, in the case of $\Omega = 1$, $\kappa = \sqrt{2}$, and $\bar{n} = 30$, $\Omega_{\bar{n}}$ is 5.75. The time unit for *modified* atomic inversion in this thesis is $\frac{1}{\Omega_{\bar{n}}^m}$, where $\Omega_{\bar{n}}^m$ is the *modified* Rabi frequency as defined in Eq. (2.3).

³The condition can be achieved by setting the atomic transition energy depends on the number of certain photon number, n' , and atom-field coupling constant, $\hbar\Delta = 2\hbar\Omega\sqrt{n'+1}$. In this dissertation, the fixed photon number is $n' = 1$, in which $n' \neq n$.

QED provides the conditions for steering the dynamics of collapses and revival sequences of Rabi oscillations.

In the recent years, there have been several efforts to control the collapses and revivals^[66-69], in order to damp out^[70-72] or to ensure the stability^[73], of the oscillations by considering the trade-off of physical constraints in the related quantum computer schemes. Nevertheless, the general theory of how to control the atomic inversion is poorly comprehended.

On the theoretical side, Darboux transformations contributions to the wide range of physics fields have been widely known over centuries^[45]. Different from the other transforms such as the Fourier and Laplace transforms, the action of Darboux transform does not change the *domain* of the potential and state of the system, but it creates the new potential and state of the system. The output of Darboux transform is a set of new potential and state of the physical system. For instance, in nonlinear Schrödinger equation, Darboux transform generates the new solutions of the equation^[45]. The Darboux transform is very useful to describe the evolution of a physical system due to the change of its Hamiltonian potential as found in wide range of nonlinear physics. However, its contribution to the field of quantum computation is still poorly understood.

Recently, there are several efforts in order to apply Darboux transformations to quantum computation. Samsonov *et al.*, followed by Hussin *et al.*^[74], propose a novel technique to apply Darboux transformations into Jaynes-Cumming Hamiltonian^[75]. Bagrov *et al.* coined a Darboux transformation which does not violate the two-level system equation structure^[76]. These processes can be done by using the method of intertwining on the exactly solvable Dirac potentials which are equivalent to the Darboux transformations between Schrödinger potentials^[77].

The application of Darboux transformations to one-dimensional Dirac equation is performed by intertwining the Hamiltonian in Dirac equation

$$\hat{L}h_0 = h_1\hat{L}, \tag{2.2}$$

where \hat{L} is intertwining operator and h_0 (h_1) is the old (new) Dirac Hamiltonian. In the sense of perturbation theory, h_0 (h_1) is unperturbed (perturbed) Dirac Hamiltonian, where $h_1 = h_0 + V(\alpha, \beta)$, in which $\{\alpha, \beta\}$ contributing into the

perturbation terms. Recently, it has been shown that numerous problems in quantum mechanics can be solved using this technique^[31].

To date, the theoretical result relevant to the experiment was only successfully performed by Samsonov *et al.* by showing the contribution of pseudosymmetry potential in controlling the qubit dynamics of superconducting circuits based on Josephson tunnel junctions^[78]. In this chapter, we show that it is possible to control Rabi oscillations in cavity QED by considering the presence of extra classical electromagnetic fields. It emerges the perturbation effect on the system and can be represented by one fold Darboux transformations on one-dimensional Dirac equation. The results suggest that there is a correlation between Dirac potentials and atomic inversion.

For our purpose, we *modify* the Rabi frequency by involving additional term representing the classical effect of electromagnetic field. The modified Rabi frequency is

$$\Omega_n^m = \sqrt{\Omega^2(\kappa^2 + b^\dagger b + n + 1)}. \quad (2.3)$$

The superscript ‘*m*’ denotes the modification. Eq. (2.3) represents the condition that the electromagnetic field *concurrently* behaves classically and quantumly : the term $\sqrt{b^\dagger b}$ corresponds to classical field and $\sqrt{n + 1}$ is the consequence of quantum effect of the field. This term can be easily derived from a Hamiltonian driven by a classical light source as mentioned in Ref.^[79]. The *modified* atomic inversion is

$$W(t) = \frac{\langle \gamma, \uparrow | \sigma_z(t) | \gamma, \uparrow \rangle^m}{\langle \gamma, \downarrow | \sigma_z(0) | \gamma, \downarrow \rangle} = e^{-|\gamma|^2} \sum_{n=0}^{\infty} \frac{|\gamma|^{2n}}{n!} \left(1 - 2(\Omega)^2 \sqrt{b^\dagger b + n + 1} \frac{\sin^2(\Omega_n^m t)}{(\Omega_n^m)^2} \right). \quad (2.4)$$

Darboux transformation contributes to the $b^\dagger b$ term. For N -fold Darboux transformations, $b^\dagger b \rightarrow b_i[1]^\dagger b_i[1] \rightarrow \dots \rightarrow b_i^\dagger[N] b_i[N]$, where subscript i corresponds to the choice of Pauli matrix in the intertwining operator.

The chapter is organized as follows: in Subsection (2.2.1), we introduce the method proposed by Bagrov *et al.* and generalize the methods : Pauli matrix in operator B is not constrained in σ_3 , but the use of $\{\sigma_1, \sigma_2\}$ is also considered. Moreover, the potential is not only restricted in (pseudo)-scalar form, but also

we allow the potential in the form of vector where the Pauli matrices act as the potential basis and the function as the potential coefficient. Subsection (2.1) contains introduction of the mathematical model of atom-field interaction in cavity QED. Here, the Rabi frequency and oscillations of a fully-quantum mechanical model are modified due to the presence of the *extra* classical effect of electromagnetic field. Section (2.3) provides the elucidation of the implementation of BBGS-Darboux transformations to semiclassical Rabi model. The outcome is to obtain the parameters in BBGS-Darboux transformations : $\alpha(t)$, $\beta(t)$, and $|V(t)|$. The section covers two types of procedures: *first* one is reformulation of the equation from Schrödinger equation into Dirac equation. Here, the representation of data is changed, but we do not control anything. *Second* one is the action of Darboux transformation on the Dirac equation. In this step, we perturb the system to control the potential and state of the system. In Section (2.4), it is shown that the choice of Pauli matrices in BBGS-Darboux transformations relates to the type of one-dimensional stationary Dirac potential of electromagnetic field : $\{\sigma_1\}$ generates the parabolic potential and $\{\sigma_2, \sigma_3\}$ yields the harmonic oscillator potential. The trade-off between the quantum and light predominances are discussed in Section (2.5).

2.2.1 BBGS-Darboux transformations

In this Subsection, we introduce (Bagrov, Baldiotti, Gitman, and Shamshutdinova) BBGS-Darboux transformations^[76] which has the notation $\mathcal{D}(\sigma_i)$. The symbol σ_i is the Pauli matrix in element of intertwining operator $\hat{L} = A \frac{d}{dt} + B$, $A = \sigma_0 = \begin{pmatrix} 1 & 0 \\ 0 & 1 \end{pmatrix}$, and $B = \alpha_i(t) + (f(t) - \beta_i(t))\sigma_i$.

The action of $\mathcal{D}(\sigma_i)$ on a set of potential and state of a Hamiltonian is defined by $\mathcal{D}(\sigma_i)[N] \{V, \Psi\} = \{V[N], \Psi[N]\}$ transforming the old Hamiltonian $\hat{h}(V)\Psi = \varepsilon_0\Psi \rightarrow \hat{h}(V[1])\Psi[1] = \varepsilon_1\Psi[1] \rightarrow \dots \rightarrow \hat{h}(V[N])\Psi[N] = \varepsilon_N\Psi[N]$. The potential is a vector in three dimensional Euclidean Bloch sphere using Pauli matrices as the basis and it can be extended into n -dimensions^[80]. The transformations affect the potential from $V(t) = \sum_j \sigma(j)^j f_j(t) \rightarrow V[1](t) = \sum_j \sigma(j)^j f'_j(t)$, where $f'_j(t) = f_j(t) + \Delta f_j(t)$ and $\sigma(j) \in \{\sigma_1, \sigma_2, \sigma_3\}$. Based on this formulation, the magnitude of potential is transformed $|V(t)| = \sum_j |f_j(t)| \rightarrow |V_i[N](t)| = \sum_j |f'_j(t)|$. The effect of the transformations to the state is $\Psi \rightarrow \hat{L}\Psi = \Psi[N]$. In order to

2.3 Rabi model under BBGS-Darboux transformation

obtain the coefficients $\alpha_i(t)$ and $\beta_i(t)$, intertwining operation, $\hat{L}\hat{h}_{\text{old}} = \hat{h}_{\text{new}}\hat{L}$, between the old and the new Hamiltonian is needed. For N -fold BBGS-Darboux transformations, $\hat{L}\hat{h}_0 = \hat{h}_1\hat{L} \rightarrow \hat{L}\hat{h}_1 = \hat{h}_2\hat{L} \rightarrow \dots \rightarrow \hat{L}\hat{h}_{N-1} = \hat{h}_N\hat{L}$.

After the above definitions, we can now express the following theorem.

Theorem 1. *Let $\{V, \Psi\}$ represents a physical system and $\mathcal{D}(\sigma_i)[N]$ is a BBGS-Darboux transformation operator. The open-loop control mechanism can be constructed, where the BBGS-Darboux transformation operator can be assumed as a controller, $\{V, \Psi\}$ as the initial system, $\{V[N], \Psi[N]\}$ as the final system, and the eigenvalues $\varepsilon_N(\sigma_i)$ are the output variables.*

Proof. Let $\{V, \Psi\}$ is the initial condition of a physical system, in which the initial eigenvalues ε_0 are belong to the system.

The action of BBGS-Darboux transformation on this system is $\mathcal{D}(\sigma_i)[N]\{V, \Psi\} = \{V[N], \Psi[N]\}$, in which the eigenvalues $\varepsilon_N(\sigma_i)$ are belong to the new eigenstates $\Psi[N]$.

The complete proofs of the above theorem are given in Section (2.3) and Section (2.4). In this chapter, we only consider $N = 1$ or one fold Darboux transformations.

2.3 Rabi model under Darboux transformations

In this Section, we present the theoretical explanation underlying the perturbation effects of atomic-field in a cavity due to the presence of the classical fields. The perturbation causes the emergence of new potential in which it is perturbed on y -axis of Bloch sphere. It is accomplished by two steps: *first*, the representation of the system is changed from Schrödinger equation into one-dimensional Dirac equation. The motivation of this change of representation is based on an one-dimensional Dirac equation is considered more appropriate than Schrödinger equation, since one-dimensional Dirac equation admitting vectors in their potential, instead of Schrödinger equation which its potential is in the scalar form only^[31]. *Second*, the action of Darboux transform is applied on the Dirac equation, corresponds to the physical system being perturbed so that the potential and the state of the system becomes controllable.

2.3 Rabi model under BBGS-Darboux transformation

In our evaluation of BBGS-Darboux transformations in the context of Rabi model, results are substituted into the modified Rabi frequency to obtain the dynamics of Rabi oscillation. The evaluation of BBGS-Darboux transformations in Rabi model involves three Pauli matrices : $\{\sigma_1, \sigma_2, \sigma_3\}$. The outcomes of this evaluation are : *first*, the perturbation terms, i.e., the coefficients $\alpha_i(t)$ and $\beta_i(t)$ which are required to obtain the transformations operator, B ; *second*, the new Dirac potential of field, $|V_i[1](t)|$. We further find that Homotopy Perturbation Method (HPM)^[81] is necessary when solving the coupled-nonlinear Riccati differential equations problem for $\mathcal{D}(\sigma_1)[N = 1]$.

2.3.1 Rabi model in one-dimensional Dirac equation

The first procedure, i.e., the change of representation from Schrödinger equation to Dirac equation, is given in this Subsection. Rewriting Schrödinger equation into one-dimensional stationary Dirac equation of Rabi model

$$\hat{h}\Psi = \varepsilon_0\Psi, \quad (2.5)$$

where $\hat{h} = (i\hbar\sigma_z\frac{d}{dt} + V)$, $V = -\hbar\Omega(\sigma^+b(t) - \sigma^-b^\dagger(t))$ and ε_0 is $\frac{\hbar\omega_0}{2}$. We also use the following assumption $b(t) = b_0e^{-i\omega t}$ and

$$b_i[1](t) = 2\beta_i(t) - b(t). \quad (2.6)$$

Because b_0 is a constant and real, i.e., $b_0^\dagger = b_0$.

The Dirac potential¹ in Eq. (2.5) can be easily changed into

$$V(t) = i\hbar\Omega b_0(\sigma_x \sin(\omega t) - \sigma_y \cos(\omega t)),$$

meaning that the potential is in a vector form using Pauli matrices as orthogonal basis.

Although the idea of representing the physical system with an one-dimensional Dirac equation may be better than Schrödinger equation: the atomic excitation term in the Hamiltonian vanishes in the new representation. This means a new representation may be valuable to explain the phenomenon in which coupling is much stronger than atomic excitation observed in Ref.^[82].

¹The time unit of Dirac potential is $\frac{1}{\omega}$.

2.3.2 The action of BBGS-Darboux transformation on Rabi model in one-dimensional Dirac equation

Next topic is an action of Darboux transformation on the new representation. Below, the procedure is elucidated in depth.

The one fold BBGS-Darboux transformations can be changed as

$$\begin{aligned}
 V(t) &= \sum_{j=1}^2 \sigma_j f_j = \sigma_1 f_1(t) + \sigma_2 f_2(t) \\
 &= -\hbar\Omega(\sigma^+ b(t) - \sigma^- b^\dagger(t)) \\
 &= i\hbar\Omega b_0(\sigma_x \sin(\omega t) - \sigma_y \cos(\omega t)) \\
 \rightarrow V_i[t] &= \sum_{j=1}^2 \sigma'_j f'_j = \sigma'_1 f'_1(t) + \sigma'_2 f'_2(t) \\
 &= -\hbar\Omega(\sigma^+ b_i[1](t) - \sigma^- b_i^\dagger[1](t)) \\
 &= -i\hbar\Omega(\sigma_y(2\beta_i(t) - b_0 \cos(\omega t)) + \sigma_x(b_0 \sin(\omega t))).
 \end{aligned}$$

It is clear that the transformations change the initial electromagnetic field in the y -direction on the Bloch sphere to the magnitude $2\beta_i(t)$. Due to the transformations, the potential magnitude changes as

$$\begin{aligned}
 |V(t)| &= (\hbar\Omega|b_0|) \rightarrow \\
 |V_i[1](t)| &= 4|\beta_i(t)| - 4\beta_i(t)b_0 \cos(\omega t) + |b_0|.
 \end{aligned} \tag{2.7}$$

One can find in the similar manner that for Jaynes-Cummings model, the Dirac potential is $V(t) = -\hbar((\Omega\sqrt{n+1})\sigma_0 + (\omega n)\sigma_z)$ and its magnitude is $|V(t)| = \hbar\Omega\sqrt{(n+1) - (n\frac{\omega}{\Omega})^2}$.¹

From intertwining operation $\hat{L}\hat{h} = \hat{h}_1\hat{L}$, one can obtain the following equation:

$$\begin{aligned}
 i\sigma_z \dot{B} + \hbar\Omega(\sigma^+ b_i[1](t) + \sigma^- b_i^\dagger[1](t))B - \hbar\Omega(B\sigma^+ b(t) + \\
 B\sigma^- b^\dagger(t)) - \hbar\Omega(\sigma^+ \dot{b}(t) + \sigma^- \dot{b}^\dagger(t)) = 0.
 \end{aligned} \tag{2.8}$$

¹The remarkable feature under this representation is that the border between quantum and classical is simply $|b_0| = \sqrt{(n+1) - (n\frac{\omega}{\Omega})^2}$. This term comes from the condition of the atom-field interaction energy in semi-classical is equal to the energies of field and also the atom-field interaction in quantum. In Ref.^[83], it is assumed that the atom-field interaction energy in semi-classical is equal to the atomic transition and field energies in quantum on resonance to obtain the term $|b_0| = \sqrt{n + \frac{1}{2}}$.

2.3 Rabi model under BBS-Darboux transformation

This is the master equation for the following Subsections.

2.3.2.1 $\mathcal{D}(\sigma_1)$

First, we consider $\mathcal{D}(\sigma_1)$ to determine $\alpha_1(t)$, $\beta_1(t)$, and $|V_1[1](t)|$. By substituting $B = \alpha_1(t) + i(b(t) - \beta_1(t))\sigma_1$ into Eq. (2.8), the coupled nonlinear Riccati differential equations are produced as following

$$\frac{\dot{\alpha}_1(t)}{2\hbar\Omega} - \beta_1^2(t) + \beta_1(t)(e^{i\omega t} + b_0 e^{-i\omega t}) + b_0 = 0, \quad (2.9a)$$

$$\begin{aligned} & -\dot{\beta}_1(t) + i\omega b_0 e^{-i\omega t}(\hbar\Omega - 1) + 2\alpha_1(t)\hbar\Omega \\ & \times (\beta_1(t) - \cos(\omega t)) = 0, \end{aligned} \quad (2.9b)$$

which are subject to the following initial conditions $\beta_1(0) = (\beta_1)_0 = b_0$ and $\alpha_1(0) = (\alpha_1)_0 = \frac{i\omega b_0(1-\hbar\Omega)}{2\hbar\Omega(b_0-1)}$. In order to obtain the exact solution of these equations, we follow the method of employing the Homotopy Perturbation Method (HPM)^[81].

HPM is considered as a promising tool to solve exactly coupled nonlinear equations since the method successfully reconciles the homotopy theory in conjunction with perturbation theory^[84]. Prior to their amalgamation, it was generally difficult to obtain exact solutions of coupled nonlinear equations using separately homotopy theory or perturbation theory. Most perturbation methods face problems with parameters: the methods admit the existence of small parameters, despite the fact that there is no small parameter in frequent nonlinear problems. Most homotopy methods fail in defining the deformation of coupled nonlinear differential equations into simpler equations due to their complexities.

As pointed out by Sweilam *et al.*, the *modified* HPM is an effort to overcome some drawbacks in conventional HPM. In conventional HPM, the solution is truncated in a series that often coincides with the Taylor series. The problems arise since the series has a very slow convergent rate. A new idea in the modified method involves Padè approximant to enlarge the domain of convergence of the solution.

To do so, the truncated solution in Taylor series as found in conventional HPM is transformed by Laplace transformation, finding the Padé approximant,

2.3 Rabi model under BBS-Darboux transformation

and taking the inverse Laplace transform to obtain a more accurate solution of the problem. We try to apply similar procedures in order to obtain the exact solutions of Eq. (2.9). The complete algorithms are given in Appendix (A).

Starting from solving the system with Eq. (2.9) by using conventional HPM, one can find that the linear equations in terms of p , which is an embedding parameter, of these two equations are

$$p^0 : \frac{(\dot{\alpha}_1)_0[t]}{2\Omega\hbar} = 0, \quad (2.10a)$$

$$-(\dot{\beta}_1)_0[t] = 0, \quad (2.10b)$$

$$p^1 : \frac{(\dot{\alpha}_1)_1[t]}{2\Omega\hbar} = b_0 + (\beta_1)_0[t] \\ \times (e^{i\omega t} + e^{-i\omega t}b_0) + ((\beta_1)_0[t])^2, \quad (2.11a)$$

$$(\dot{\beta}_1)_1[t] = ie^{-i\omega t}\omega(\Omega\hbar - 1)b_0 \\ + 2(\alpha_1)_0[t]\hbar\Omega((\beta_1)_0[t] - \cos[\omega t]), \quad (2.11b)$$

$$p^2 : \frac{(\dot{\alpha}_1)_2[t]}{2\Omega\hbar} = (e^{i\omega t} + e^{-i\omega t}b_0)(\beta_1)_1[t] \\ + 2(\beta_1)_0[t](\beta_1)_1[t], \quad (2.12a)$$

$$(\dot{\beta}_1)_2[t] = 2\Omega\hbar(\alpha_1)_1[t]((\beta_1)_0[t] - \cos[\omega t]) \\ + 2\Omega\hbar(\alpha_1)_0[t](\beta_1)_1[t]. \quad (2.12b)$$

Furthermore, the series of solutions obtained by using the N -th order perturbation of HPM can be truncated as following

$$\alpha_1(t) \cong \sum_{i=0}^N (\alpha_1)_i(t) = \frac{i\omega b_0(1 - \hbar\Omega)}{2\hbar\Omega(b_0 - 1)} - 2\hbar\Omega(b_0^2 - b_0)\left(t + i\frac{(1 - e^{i\omega t})}{\omega}\right) + \\ \mathcal{O}(t^2), \quad (2.13a)$$

2.3 Rabi model under BBS-Darboux transformation

$$\beta_1(t) \cong \sum_{i=0}^N (\beta_1)_i(t) = b_0 + (\hbar\Omega - 1)((1 - e^{-i\omega t}) + \frac{i\omega b_0}{(b_0 - 1)}(\frac{\sin(\omega t)}{\omega} - b_0 t)) + \mathcal{O}(t^2). \quad (2.13b)$$

Then, the procedures involving Laplace transforms lead to $\mathcal{L}[\alpha_1(t)] = \hat{\alpha}_1(s)$ and $\mathcal{L}[\beta_1(t)] = \hat{\beta}_1(s)$ in which s is replaced by $\frac{1}{t}$. The definition of Laplace transform $\mathcal{L}[\alpha_1(t)] = \hat{\alpha}_1(s)$ can be found in the Appendix (A). These procedures yield

$$\alpha_1(t) \cong \sum_{i=0}^N (\alpha_1)_i(t) = \frac{i\omega b_0(1 - \hbar\Omega)}{2\hbar\Omega(b_0 - 1)}t - 2\hbar\Omega(b_0^2 - b_0)t^2(1 + i\frac{i\omega}{(1 - \omega t)}) + \mathcal{O}(t^3), \quad (2.14a)$$

$$\beta_1(t) \cong \sum_{i=0}^N (\beta_1)_i(t) = b_0 t + (\hbar\Omega - 1)t^2(\frac{\omega}{1 + \omega t} + \frac{i\omega b_0}{(b_0 - 1)}(\frac{1}{1 + \omega^2 t^2} - b_0 t^2)) + \mathcal{O}(t^3). \quad (2.14b)$$

Padé approximant, $\left[\frac{M}{N}\right]_{\{\alpha(t), \beta(t)\}}$ (t) with $\{M, N\} > 0$ and $M+N < 6$, is applied on Eqs. (2.14) to enlarge the convergence of these solutions followed by replacing the $\frac{1}{t}$ by s . The last step is obtaining the inverse Laplace transforms, $\mathcal{L}[\{\hat{\alpha}_1(s), \hat{\beta}_1(s)\}] = \{\alpha_1(t), \beta_1(t)\}$, to obtain the true solutions as following

$$\alpha_1(t) \approx \frac{1}{12}(b_0 - b_0^2)\hbar\Omega(3i\omega(4it\omega + t^2\omega^2 - 2)(\hbar\Omega - 1) + 4\hbar\Omega^2(b_0 - 1)^2t(9it\omega + t^2\omega^2 - 12)) + \mathcal{O}(t^3), \quad (2.15)$$

$$\beta_1(t) \approx \frac{\frac{2i(2b_0-1)(\hbar\Omega-1)}{\omega} - \frac{i(3b_0-2)e^{-i\omega t}(\hbar\Omega-1)}{\omega} - \frac{ib_0e^{i\omega t}(\hbar\Omega-1)}{\omega} - ib_0^2t^2\omega(\hbar\Omega-1)}{2(b_0-1)} + \frac{2(b_0-1)t(b_0+\hbar\Omega-1)}{2(b_0-1)} + \mathcal{O}(t^3). \quad (2.16)$$

The Dirac potential of this transformation can be obtained by substituting Eq. (2.16) into Eq. (2.7). The plots of Rabi oscillations and potential versus time of this transformation are shown in Fig. (2.10).

For the following Subsections, we find that the differential equations are easier and similar.

2.3 Rabi model under BBGS-Darboux transformation

2.3.2.2 $\mathcal{D}(\sigma_3)$

Second, we evaluate $\mathcal{D}(\sigma_3)$ to obtain $\alpha_3(t)$, $\beta_3(t)$, and $|V_3[1](t)|$. By replacing $B = \alpha_3(t) + i(b(t) - \beta_3(t))\sigma_3$ into Eq. (2.8), it yields

$$\dot{\beta}_3(t) + i\dot{\alpha}_3(t) + i\omega b_0 e^{-i\omega t} = 0, \quad (2.17a)$$

$$\begin{aligned} & 2\hbar\Omega(\alpha_3(t)(\beta_3(t) - b_0 \cos(\omega t)) - ib_0\beta_3(t)(\cos(\omega t) + e^{-i\omega t})) \\ & + i(\beta_3(t))^2 + \frac{ib_0}{2}(b_0(1 + e^{-i2\omega t}) + b_0\omega(\sin(\omega t) + \cos(\omega t))) \\ & = 0 \end{aligned} \quad (2.17b)$$

2.3.2.3 $\mathcal{D}(\sigma_2)$

Third, we examine $\mathcal{D}(\sigma_2)$ and determine $\alpha_2(t)$, $\beta_2(t)$, and $|V_2[1](t)|$. By changing $B = \alpha_2(t) + i(b(t) - \beta_2(t))\sigma_2$ into Eq. (2.8) results in

$$\begin{aligned} & 2\hbar\Omega((\beta_2(t))^2 - \beta_2(t)b_0 e^{-i\omega t}) + i\dot{\alpha}_2(t) \\ & - (i\omega b_0 e^{-i\omega t} + \dot{\beta}_2(t)) = 0, \end{aligned} \quad (2.18a)$$

$$\begin{aligned} & -\hbar\Omega b_0(i\omega)(\sin(\omega t) + \cos(\omega t)) \\ & + \hbar\Omega\alpha_2(t)(2\beta_2(t) - b_0 e^{i\omega t}) - \hbar\Omega\alpha_2(t)b_0 e^{-i\omega t} = 0. \end{aligned} \quad (2.18b)$$

Eqs. (2.17) and (2.18) are ordinary differential equations that are solvable. However, one needs theorem as given in Appendix (C) to simplify the solutions. From Eqs. (2.17) and (2.18), $\alpha(t)_{\{\{2,3\}\}}$ and $\beta(t)_{\{\{2,3\}\}}$ for $\mathcal{D}(\{\sigma_2, \sigma_3\})[N = 1]$ can

2.3 Rabi model under BBGS-Darboux transformation

be obtained.

For $\alpha_2(t)$, one can find

$$\begin{aligned} \alpha(t) = & 3b_0 - \cos(2\omega t) - b_0 \sin(2\omega t) + 1/2 \sqrt{2} \sqrt{\sqrt{(1 - 6b_0 + 9b_0^2 + (2 + 6b_0) \cos(2\omega t))} \\ & \frac{+(1 - b_0^2) \cos(4\omega t) - (6b_0^2 + 2b_0) \sin(2\omega t) + 2b_0 \sin(4\omega t))^2 + ((6b_0^2 + 2b_0) \cos(2\omega t) + (2 + 6b_0) \sin(2\omega t)} \\ & \frac{-2b_0 \cos(4\omega t) + (1 - b_0^2) \sin(4\omega t))^2 + 1 - 6b_0 + 9b_0^2 + (2 + 6b_0) \cos(2\omega t) + (1 - b_0^2) \cos(4\omega t)} \\ & \frac{-(6b_0^2 + 2b_0) \sin(2\omega t) + 2b_0 \sin(4\omega t)} + i \left((6b_0^2 + 2b_0) \cos(2\omega t) + (2 + 6b_0) \sin(2\omega t) - 2b_0 \cos(4\omega t) \right. \\ & \left. + (1 - b_0^2) \sin(4\omega t) + 1/2 \sqrt{2} \sqrt{\sqrt{(1 - 6b_0 + 9b_0^2 + (2 + 6b_0) \cos(2\omega t) + (1 - b_0^2) \cos(4\omega t) - (6b_0^2 + 2b_0) \sin(2\omega t)} \right. \\ & \frac{+ 2b_0 \sin(4\omega t))^2 + ((6b_0^2 + 2b_0) \cos(2\omega t) + (2 + 6b_0) \sin(2\omega t) - 2b_0 \cos(4\omega t) + (1 - b_0^2) \sin(4\omega t))^2}{-1 + 6b_0 - 9b_0^2 - (2 + 6b_0) \cos(2\omega t) - (1 - b_0^2) \cos(4\omega t) + (6b_0^2 + 2b_0) \sin(2\omega t) - 2b_0 \sin(4\omega t)} \end{aligned}$$

and for $\alpha_3(t)$ holds

$$\begin{aligned} \alpha(t) = & 3b_0 - \cos(2\omega t) - b_0 \sin(2\omega t) + 1/2 \sqrt{2} \sqrt{\sqrt{(1 - 6b_0 + 9b_0^2 + (2 + 6b_0) \cos(2\omega t) + (1 - b_0^2) \cos(4\omega t) - (6b_0^2} \\ & \frac{+ 2b_0) \sin(2\omega t) + 2b_0 \sin(4\omega t))^2 + ((6b_0^2 + 2b_0) \cos(2\omega t) + (2 + 6b_0) \sin(2\omega t) - 2b_0 \cos(4\omega t) + (1 - b_0^2) \sin(4\omega t))^2}{+ 1 - 6b_0 + 9b_0^2 + (2 + 6b_0) \cos(2\omega t) + (1 - b_0^2) \cos(4\omega t) - (6b_0^2 + 2b_0) \sin(2\omega t) + 2b_0 \sin(4\omega t)} \\ & \frac{+ i \left((6b_0^2 + 2b_0) \cos(2\omega t) + (2 + 6b_0) \sin(2\omega t) - 2b_0 \cos(4\omega t) + (1 - b_0^2) \sin(4\omega t) \right)} \\ & \left. - 1/2 \sqrt{2} \sqrt{\sqrt{(1 - 6b_0 + 9b_0^2 + (2 + 6b_0) \cos(2\omega t) + (1 - b_0^2) \cos(4\omega t) - (6b_0^2 + 2b_0) \sin(2\omega t) + 2b_0 \sin(4\omega t))^2} \right. \\ & \frac{+ ((6b_0^2 + 2b_0) \cos(2\omega t) + (2 + 6b_0) \sin(2\omega t) - 2b_0 \cos(4\omega t) + (1 - b_0^2) \sin(4\omega t))^2}{-1 + 6b_0 - 9b_0^2 - (2 + 6b_0) \cos(2\omega t) - (1 - b_0^2) \cos(4\omega t) + (6b_0^2 + 2b_0) \sin(2\omega t) - 2b_0 \sin(4\omega t)} \end{aligned}$$

The term of $\beta_{(2,3)}$ can be obtained by the substitution of $\alpha_{(2,3)}$ into Eqs. (2.18) and (2.17), respectively. The potentials can be obtained by substituting those parameters into Eq. (2.7). The plots of the Rabi oscillations and the potentials versus time are given in Figs. (2.9) and (2.6), respectively.

2.4 Correlations of the one-dimensional stationary Dirac field potential and the Rabi oscillations

The calculations in previous Section resulted in $\beta_i(t)$ which were useful to obtain the transformations from $b^\dagger b \rightarrow b_i^\dagger[1]b_i[1]$ as defined by Eq. (2.6). The evolution of these new classical fields are illustrated in Fig. (2.3). Furthermore, these new classical fields, $\{b_1^\dagger[1]b_1[1], b_2^\dagger[1]b_2[1], b_3^\dagger[1]b_3[1]\}$, are substituted into the *modified* Rabi frequency¹ as expressed by Eq. (2.3). Consequently, it influences the modified atomic inversion in Eq. (2.4). The illustration of these schemes can be found in Fig. (C.5) in the Appendix (C).

Initially, the atom-field system has the potential, $V(t)$, whose magnitude is $(\hbar\Omega)|b_0|$ in the semiclassical Rabi model and $\hbar((\Omega\sqrt{n+1})\sigma_0 + (\omega n)\sigma_z)$ for the Jaynes-Cummings model. Then, it is transformed into several types of new potentials. The results can be divided into two parts : *first*, the transformation by $\mathcal{D}(\sigma_1)$ results in the parabolic potential; *second*, the transformations by $\mathcal{D}(\{\sigma_2, \sigma_3\})$ yield the harmonic oscillator potentials. We provide in the Appendix (C) the detailed of computational methods for producing the graphs in this Section.

2.4.1 The parabolic potential

The choice of σ_1 corresponds to circumventing the atomic population into the equilibrium condition.

As can be seen in Fig. (2.4(a)), the absence of Dirac potential causes the atom to occupy the ground state: during the potential is turned off ($t < 10$) the oscillations stay negative meaning that initially the atoms occupy ground state, $|g\rangle|n\rangle$.

¹It is assumed in this work that the *modified* Rabi frequency (Ω_n^m) can be achieved to the electromagnetic field frequency (ω) due to the presence of classical electromagnetic field, or $\Omega_n^m = \omega$. If the physical system requires the detuning field frequency in GHz, it means the time units for atomic inversion and Dirac potential are in *ns*.

2.4 Correlations of the one-dimensional stationary Dirac field potential and the Rabi oscillations

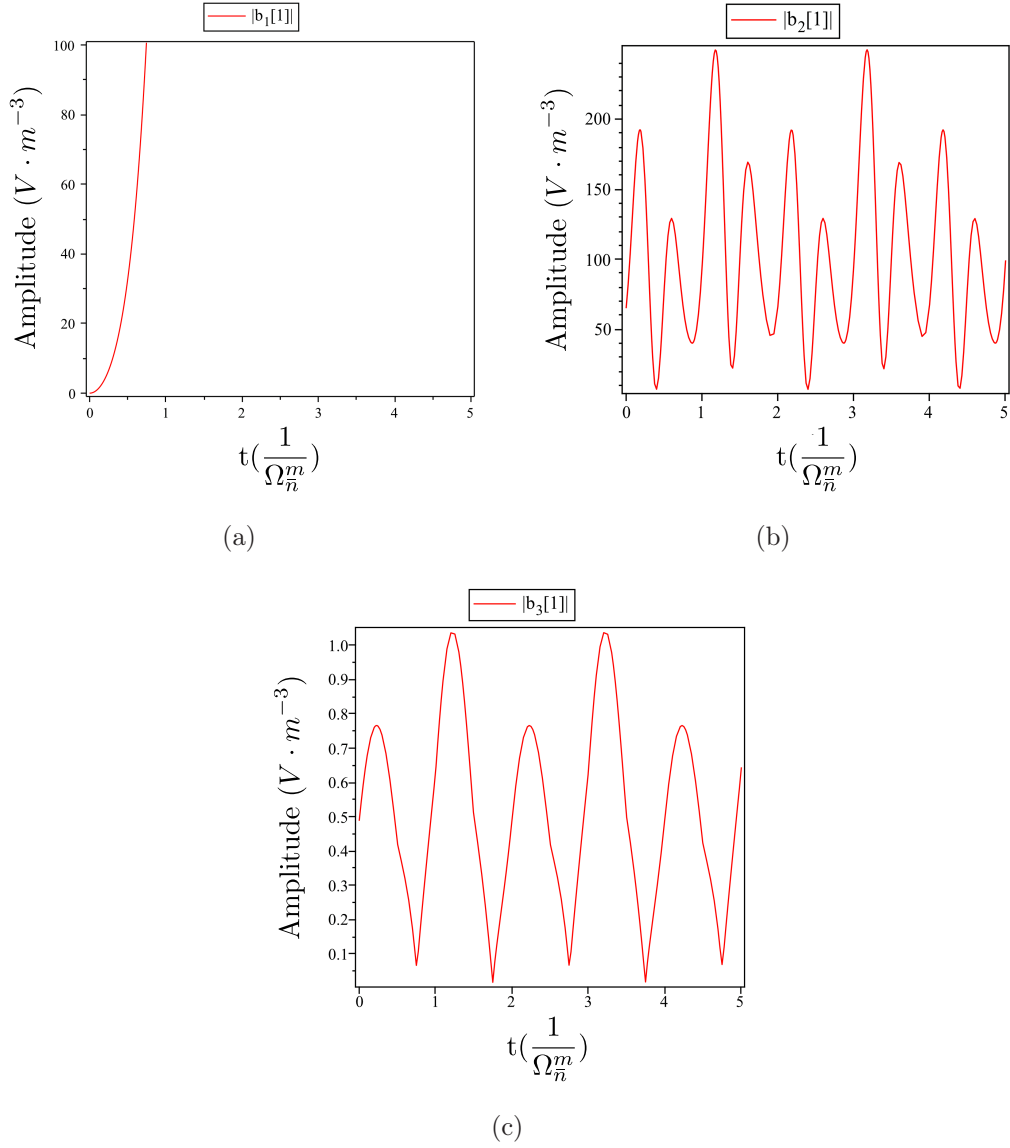
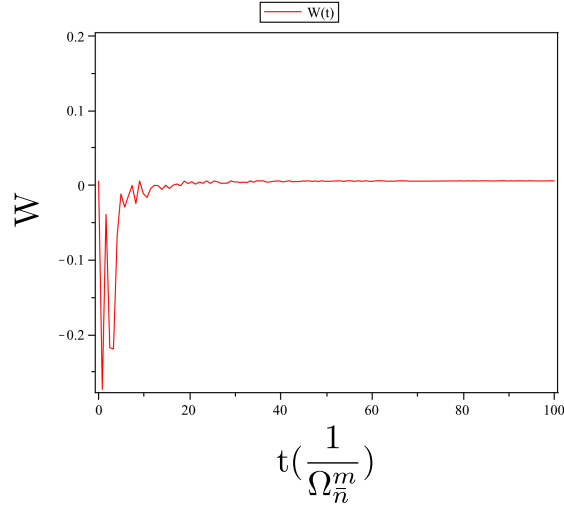
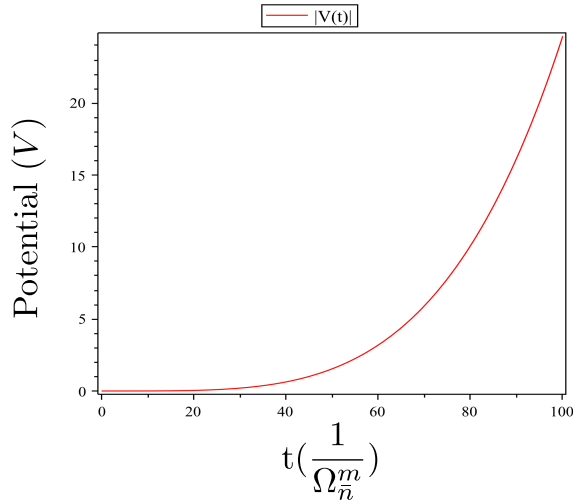


Figure 2.3: The evolution of classical electromagnetic field intensity of (a). $|b_1[1]|$, (b). $|b_2[1]|$, and (c). $|b_3[1]|$, from initial value of $|b|$ is 1.

2.4 Correlations of the one-dimensional stationary Dirac field potential and the Rabi oscillations



(a)

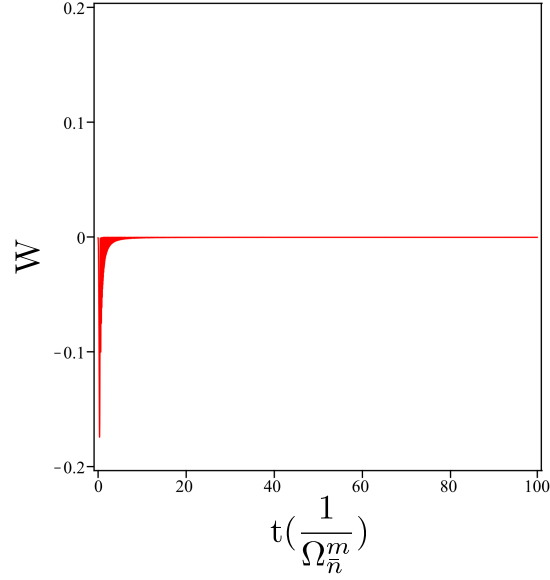


(b)

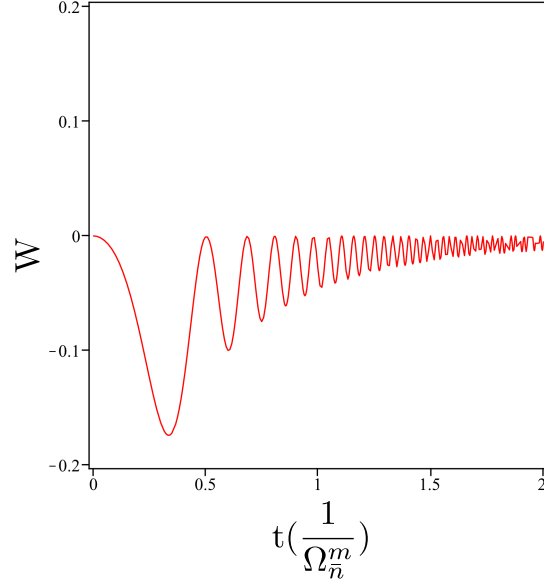
Figure 2.4: The time evolution of the population of two states (a) and the time evolution of Dirac potential (b) in cavity quantum electrodynamics of $\mathcal{D}(\sigma_1)$ for $t = 100$.

Next is a situation where the potential is turned on after $t = 10$. It causes that the atomic population in the ground state is gradually vanished and coherently sharing of the atomic populations between the excited- and ground-states emerges. Under this circumstance, the Rabi oscillations are collapsed and damped

2.4 Correlations of the one-dimensional stationary Dirac field potential and the Rabi oscillations



(a)



(b) The expansion of Fig. (2.5(a)).

Figure 2.5: The time evolution of the population of two states (a) for t is from 0 to 10 and for t is from 0 to 2 (b) in cavity quantum electrodynamics of $\mathcal{D}(\sigma_1)$. These figures are simulated for 6000 data points.

2.4 Correlations of the one-dimensional stationary Dirac field potential and the Rabi oscillations

out to a monotonous line.

This phenomenon is similar to the previous results in Ref.^[85] and Ref.^[86]: driven by the classical field; the population is shared coherently between the states $|g, 0\rangle$ and $|l, 1\rangle$, where $|l, 1\rangle = \frac{(|e, 0\rangle + |g, 1\rangle)}{2}$. However, they cannot show the appearance of several oscillations in ground state before the monotonous line.

Fig. (2.4(a)) shows that the Rabi oscillation is $\sim \frac{e^{-kt}}{t}$. This oscillation can be generated if the Dirac potential is parabolic as shown in Fig. (2.4(b)).

The results may be important for the future of quantum information. The choice of σ_1 causes the coherent sharing between the excited- and ground-states. It means that in the case of interaction with classical field being much greater than atomic excitation in cavity quantum electrodynamics, the parabolic Dirac potential can change the qubit basis from σ_z -eigenbasis into σ_x -eigenbasis.

2.4 Correlations of the one-dimensional stationary Dirac field potential and the Rabi oscillations

2.4.2 The harmonic oscillator potentials

Fig. (2.6(a)) shows that $\mathcal{D}(\sigma_3)$ generates the sequences of peaks in negative regime. This means that the population is driven into the ground state. The sequences of peaks in Rabi oscillations can be created by adjusting fast oscillations of the Dirac potential in the positive regime as shown in Fig. (2.6(b)). Under this scheme, the sharpness of peaks in atomic inversion is directly proportional to the oscillations of Dirac potential. For instance, when $t \sim 2000$, the extremely sharp peaks are produced if the fast oscillations of Dirac potential occur. Contrarily, when $t \sim 6000$, peaks becomes unsharp because oscillations of Dirac potential are smooth and slow.

The emergence of these peaks in Rabi oscillations and the correlations with the Dirac potentials may be relevant in the case of *circuit* quantum electrodynamics consisting of two superconducting qubits coupled to an on-chip coplanar waveguide (CPW) that explore the power dependence of the heterodyne transmission as shown in Ref.^[87]. Bishop *et al.* showed that the emergences of peaks identified as a multiphoton-transmon qubit transition from the ground state to an excited Jaynes-Cummings state occurred due to the large driving of heterodyne transmission. In contrast with our results, the transition begins to saturate as the power increases.

Furthermore, the choice of (σ_2) produces Rabi oscillations which are proportional to the oscillations of Dirac potential.

It is shown in Fig. (2.9(a)) that initially the atom is in the excited state. The atomic population is gradually driven into the ground state along with the oscillations of potential. Due to the presence of the oscillations of Dirac potential as illustrated in Fig. (2.9(b)), the atomic inversion has the sequences of oscillations and collapses which is like quantum Rabi oscillations.

Therefore, it is possible to ensure the coherency of the qubits by tuning the Dirac potential in the oscillations form as shown in Fig. (2.9(b)).

As a conclusion, the following Figures (Fig. (2.11(a)) and Fig. (2.11(b))) give an illustration how the Darboux transformations change the amplitude and the periodicities of the initial quantum Rabi oscillations.

2.4 Correlations of the one-dimensional stationary Dirac field potential and the Rabi oscillations

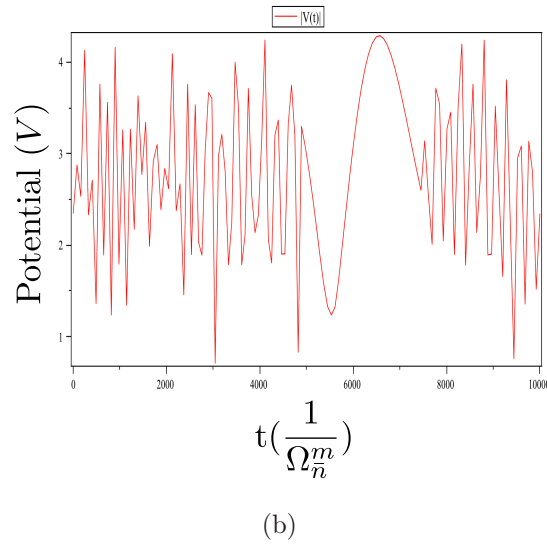
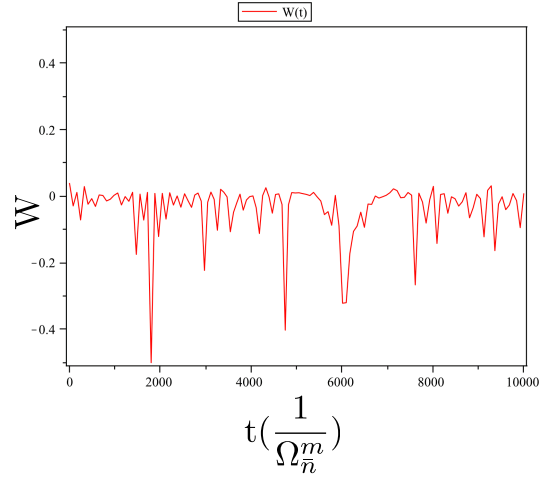
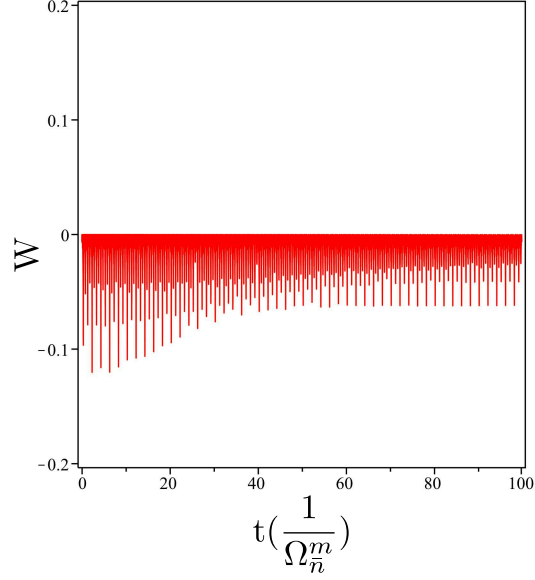
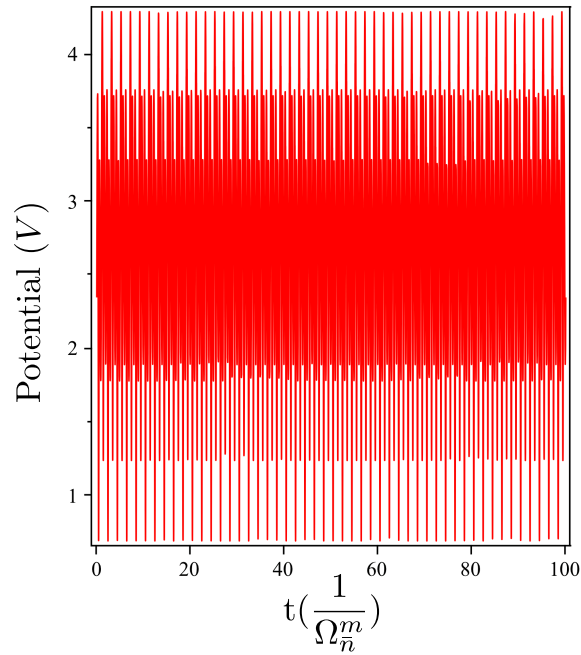


Figure 2.6: The time evolution of the population of two states (a) and the time evolution of Dirac potential (b) in cavity quantum electrodynamics of $\mathcal{D}(\sigma_3)$ for $t = 10^5$.

2.4 Correlations of the one-dimensional stationary Dirac field potential and the Rabi oscillations



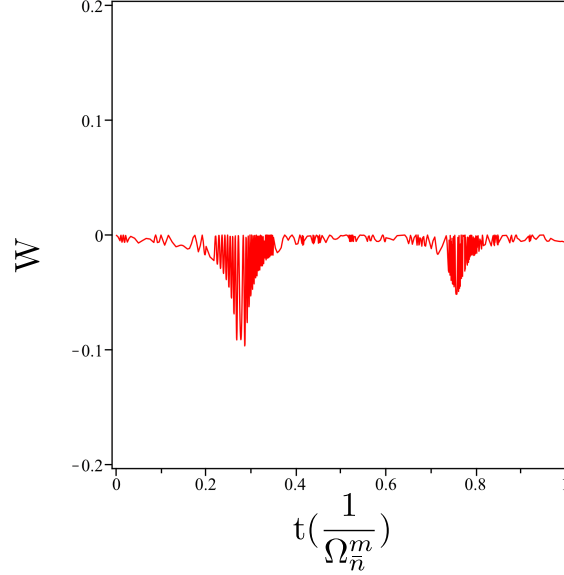
(a)



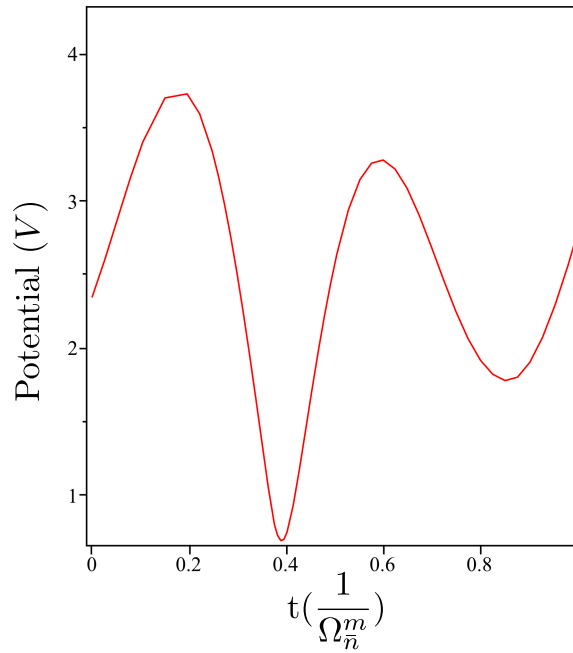
(b)

Figure 2.7: The time evolution of the population of two states (a) and the time evolution of Dirac potential (b) in cavity quantum electrodynamics of $\mathcal{D}(\sigma_3)$ for t is from 0 to 100. These figures are simulated for 6000 data points.

2.4 Correlations of the one-dimensional stationary Dirac field potential and the Rabi oscillations



(a) The expansion of Fig. (2.7(a)).



(b) The expansion of Fig. (2.7(b)).

Figure 2.8: The time evolution of the population of two states (a) and the time evolution of Dirac potential (b) in cavity quantum electrodynamics of $\mathcal{D}(\sigma_3)$ for t is from 0 to 1. These figures are simulated for 6000 data points.

2.4 Correlations of the one-dimensional stationary Dirac field potential and the Rabi oscillations

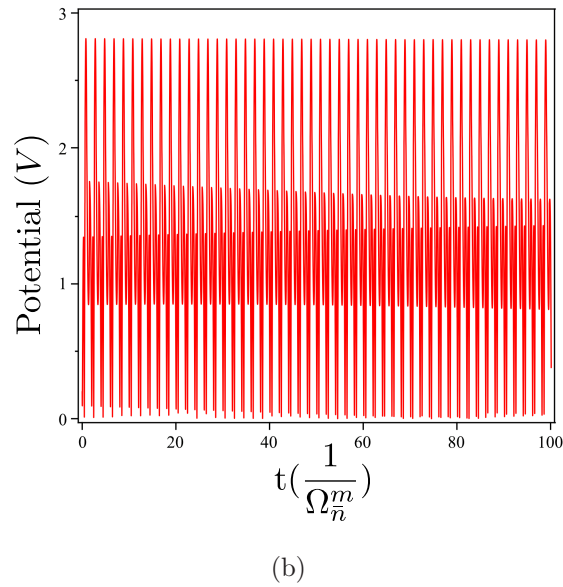
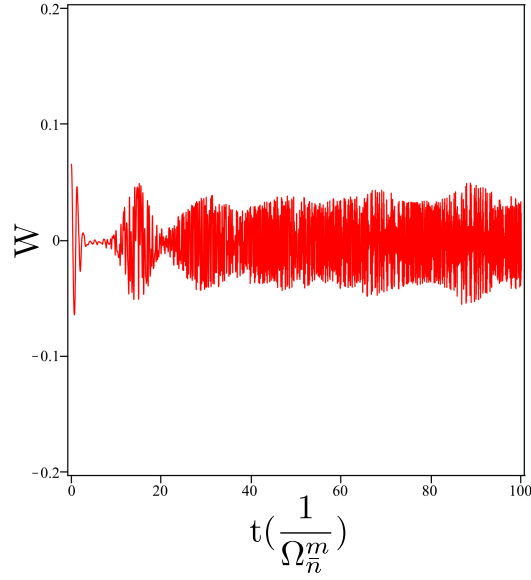


Figure 2.9: The time evolution of the population of two states (a) and the time evolution of Dirac potential (b) in cavity quantum electrodynamics of $\mathcal{D}(\sigma_2)$ for t is from 0 to 100. These figures are simulated for 6000 data points.

2.4 Correlations of the one-dimensional stationary Dirac field potential and the Rabi oscillations

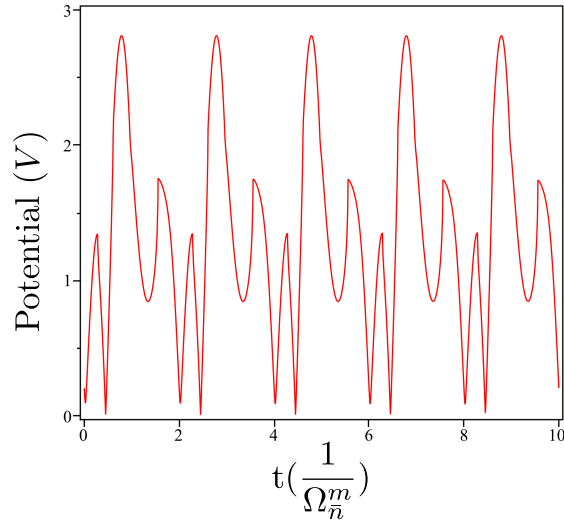
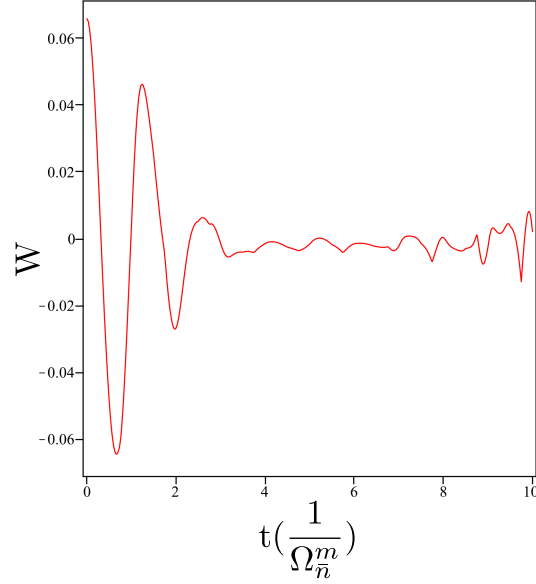
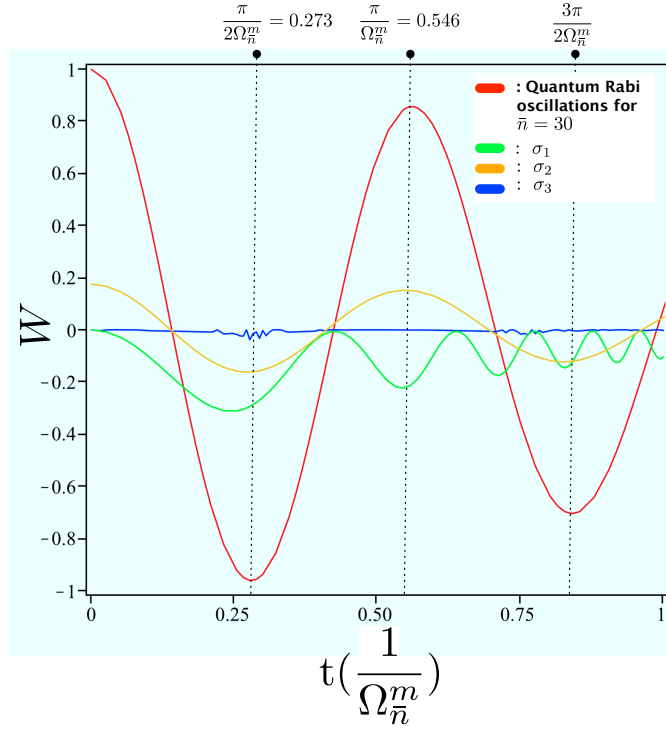
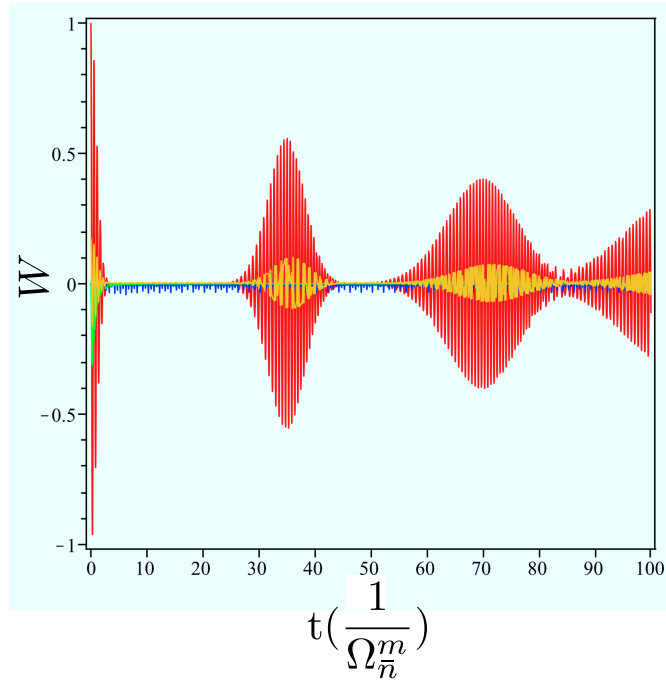


Figure 2.10: The time evolution of the population of two states (a) and the time evolution of Dirac potential (b) in cavity quantum electrodynamics of $\mathcal{D}(\sigma_2)$ for t is from 0 to 10. These figures are simulated for 6000 data points.

2.4 Correlations of the one-dimensional stationary Dirac field potential and the Rabi oscillations



(a)



(b) The extension of Fig. (2.11(a)).

Figure 2.11: The comparison between the quantum Rabi oscillations and the changes due to the Darboux transformations.

2.5 The trade-off between quantum and classical light

The analyses in the previous sections are based on a certain number of $|b_i[1]|$ (classical part) and n (quantum part) of light. However, these approaches cannot give a general picture of the influence of quantum and classical light predominances to the atomic inversion evolution. Therefore, in this section, the trade-off between quantum and classical light and their influence into the atomic inversion is discussed. By the use of this scheme, the nature behavior of atomic inversion due to the determinacy of classical and quantum light can be seen clearly.

In the case of $\mathcal{D}(\sigma_1)$, the presence of pure classical light and the absence of quantum light causes the atomic inversion in pure monotonous line. The Fig (2.12(a)) shows the extreme condition of predominance of classical light in cavity causing the coherent share of excited and ground states. If the predominance of quantum light is increased, the oscillation near the ground state will occur. Figs. (2.12(b)), (2.12(c)), and (2.12(d)) show that the number of oscillations are increased due to the increase of quantum light inside the cavity. The strong oscillations in the ground state can be generated if the light is predominantly quantum. Fig. (2.12(e)) shows the case of the light being purely quantum. In the last case, as shown in Fig. (2.12(f)), the number of classical and quantum lights are balanced and very strong, i.e, it is chosen that the value of $|b_1[1]|$ and n is 1000. The result is that there are several oscillations near the ground state before the monotonous line in the atomic inversion.

Our simulations show that the unexpected results are found in the case of $\mathcal{D}(\sigma_2)$. Fig. (2.13(a)) shows quantum Rabi oscillations when light is predominantly quantum. If the classical predominance is increased, as illustrated in Figs. (2.13(b)), (2.13(c)), and (2.13(d)), the quantum Rabi oscillations are changed into the other type of oscillations in which there are several extreme peaks that appears regularly. Due to the quantum light predominance, the atoms occupy near the excited state. By increasing the classical light predominance, the atomic population is driven into the ground state; it can be seen in Fig. (2.13(e)) that the atoms occupy the ground state due to the presence of classical light and the absence of quantum light. If the predominance of quantum and classical light is

2.5 The trade-off between quantum and classical light

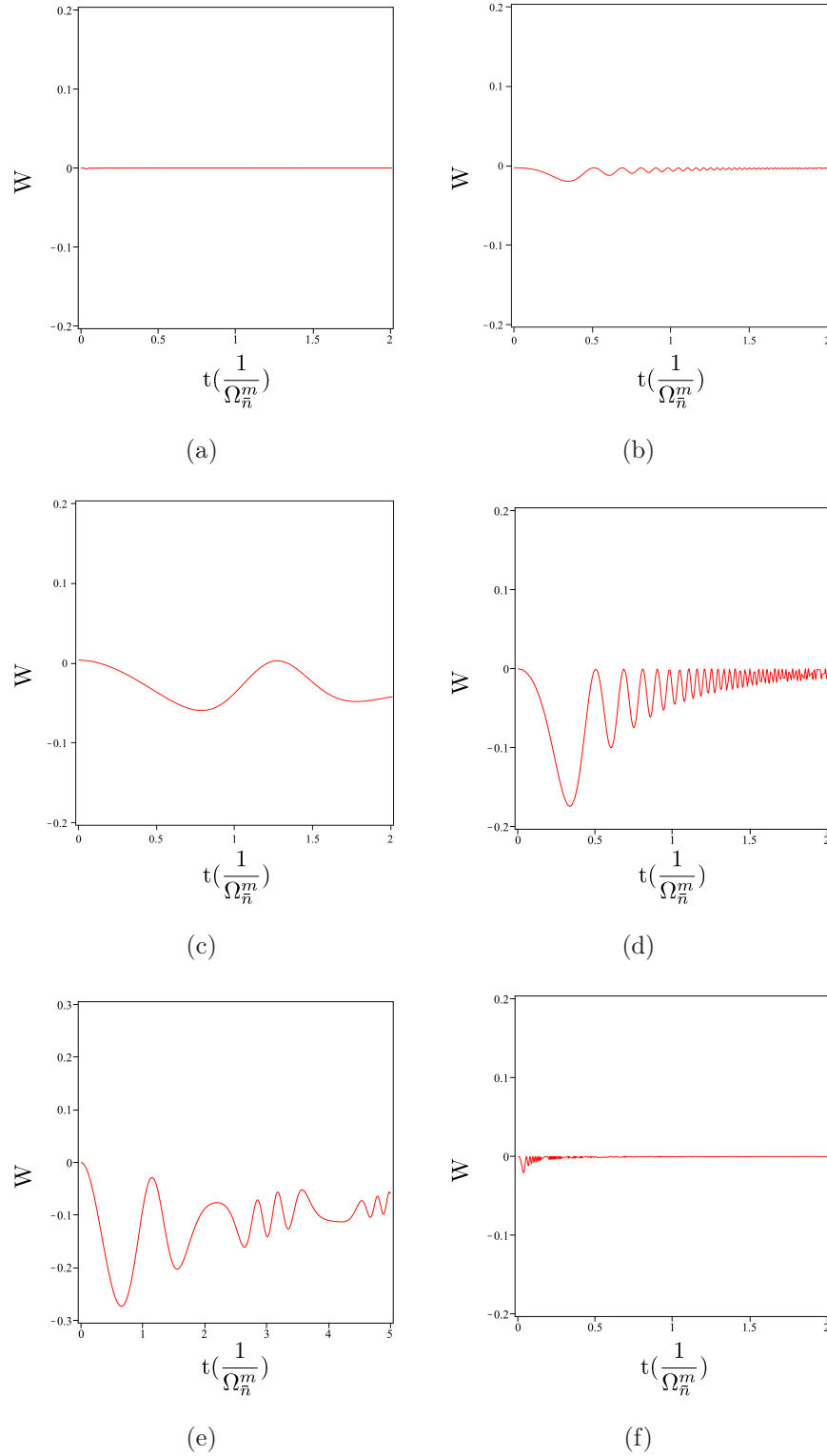


Figure 2.12: (a). $|b_1| = 1000, n = 0$, (b). $|b_1| = 10, n = 1$; (c). $|b_1| = 0, n = 1$; (d). $|b_1| = 10, n = 100$; (e). $|b_1| = 0, n = 1000$; (f). $|b_1| = 1000, n = 1000$.

2.5 The trade-off between quantum and classical light

balanced, as shown in Fig. (2.13(f)), it is found that atomic population is in the excited state.

In the situation of $\mathcal{D}(\sigma_3)$, it is found that the full predominance of quantum light, as shown in Fig. (2.14(a)), i.e, for $|b_3[1]|=0$ and $n = 1000$, causes the atoms to occupy the ground state. Figs. (2.14(a)) and (2.14(b)) show that in this circumstance that the atoms oscillate *like* quantum Rabi oscillations, but near the ground state only. Figs. (2.14(c)), (2.14(d)), and (2.14(e)) show the change of the Rabi oscillations due to the decrease of quantum light predominance and the increase of classical light predominance. The disappearance of oscillations in the atomic inversion is due to the increase of the classical light predominance. The existence of quantum light in the cavity keeps the coherent sharing between excited- and ground states; if the light is fully classical, as shown in Fig. (2.14(f)), the atoms occupy the ground state without any oscillations.

This section enriches the previous results that controlling the time evolution of atomic inversion not only can be realized by the choose of the intertwining operator input in Eq. (2.2), which is a Pauli matrix, but also by the combination between the input and the predominance of quantum and classical light. The predominance of quantum light causes the appearance of oscillations while the classical light predominance is related to the monotonous line in the Rabi oscillations.

2.5 The trade-off between quantum and classical light

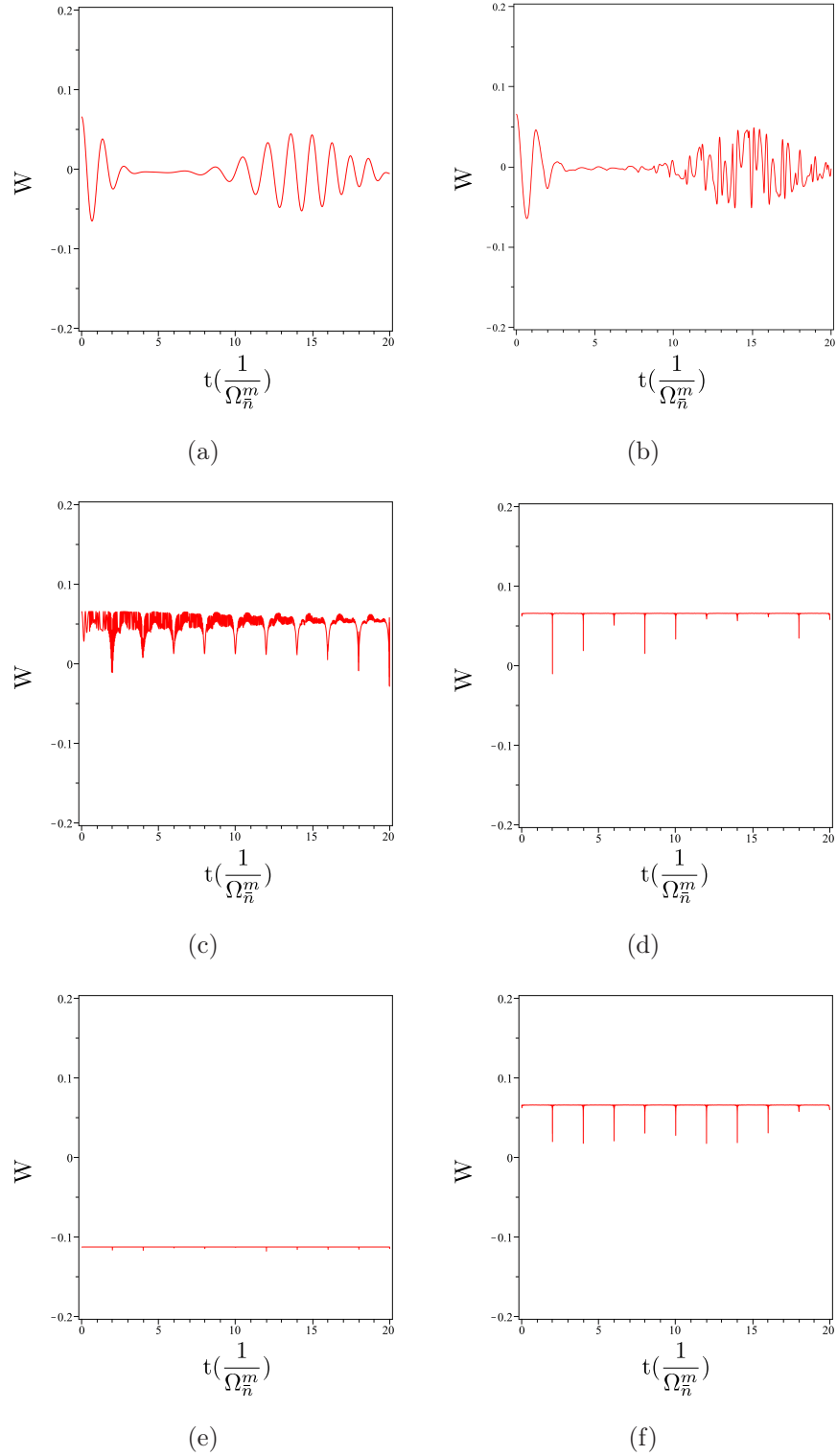
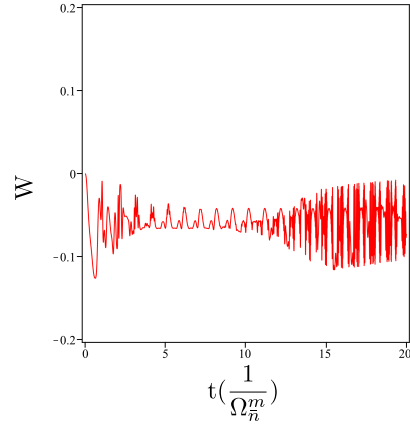
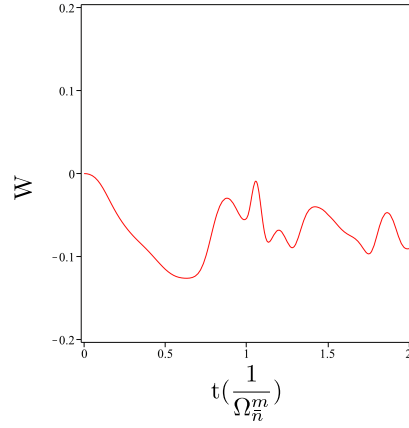


Figure 2.13: (a). $|b_2| = 0, n = 1000$; (b). $|b_2| = 0, n = 10$; (c). $|b_2| = 10, n = 1000$; (d). $|b_2| = 1000, n = 10$; (e). $|b_2| = 1000, n = 0$; (f). $|b_2| = 1000, n = 1000$.

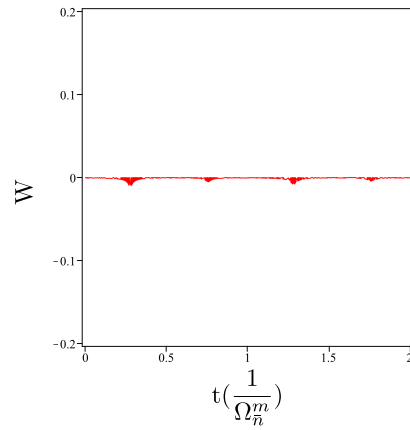
2.5 The trade-off between quantum and classical light



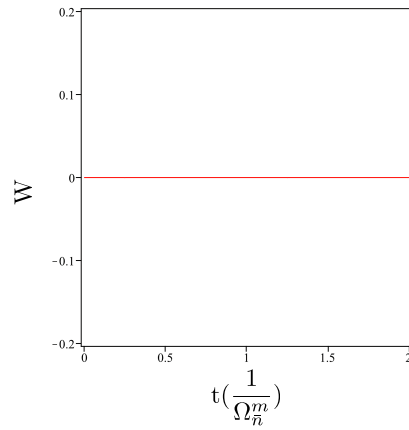
(a)



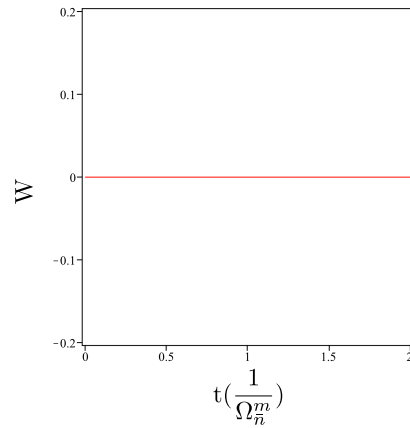
(b) The expansion of Fig. (2.14(a)).



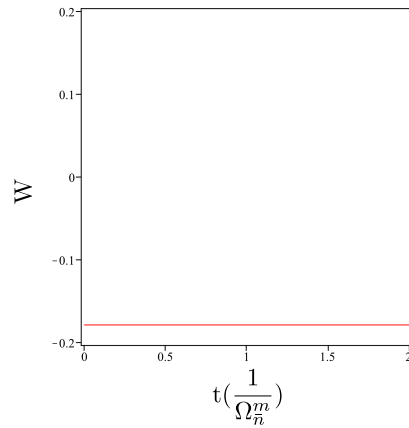
(c)



(d)



(e)



(f)

Figure 2.14: (a) and (b). $|b_3| = 0$, $n = 1000$; (c). $|b_3| = 10$, $n = 1000$; (d). $|b_3| = 1000$, $n = 10$; (e). $|b_3| = 500$, $n = 500$; (f). $|b_3| = 0$, $n = 1000$.

2.6 Physical implementation

The proposed method suggests that the scheme is working under the apparatus in which the electromagnetic fields *concurrently* behave quantumly and classically. The one of possibilities to perform this is by involving the extra device in the cavity that generates the field behaving classically. Another possibility is involving an instrument performing external forces behaving as *artificial* classical field.

In the recent research of photons in cavities, the state can be excited by photon transmission followed by the photon blockade of an optical cavity resulting in trapping one ion in the regime of strong atom-cavity coupling^[65]. A single atomic path is also controllable by the feedback of photon-by-photon^[88]. However, it is not clear how photon, the quantum of the electromagnetic field, contributes to control the excitation and decay of the atomic population.

The next constraint is the classical field $\sim \sqrt{b^\dagger b}$ contribution to the *modified* Rabi oscillations. An experiment of classical field driving the atomic population in cavity may be related to the experimental effort to realize the Keldysh picture^[89]. Recent explorations demonstrate that controlling the electronic motion is enabled in ultrafast laser sources in the mid-infrared region^[90].

2.7 Limitation and future works

1. **Qubit phase.** This work shows how to manipulate the amplitude of a qubit so that it can be used for quantum information processing. However, the technique of how to control the qubit phase on Bloch sphere is still unclear under this scheme. This aspect needs to be explored.
2. **The border between classical and quantum regimes based on the number of photons is not clear.** It is assumed in this work that the number of quantum and classical light is independent. The future works shall consider the condition distinguishing the quantum and classical lights.
3. **Energy of classical and quantum light is undistinguishable.** The energy of quantum and classical light is assumed to be in the same level. However, there should be a difference between them since there are photons whose energy is absorbed by the atoms for the case of quantum light.

Chapter 3

Circuit design for a measurement-based quantum carry-lookahead adder

3.1 Introduction

Measurement-based quantum computation (MBQC) is a new paradigm for implementing quantum algorithms using a quantum cluster state^[12,21,36,91]. A cluster state is a highly entangled state of qubits which can serve as the resource for universal quantum computation. By subsequent single-qubit measurements, quantum gates are effected on the logical qubits encoded in the cluster state. Quantum information propagation in a cluster is driven by the pattern of measurement bases, regardless of the measurement outcomes. MBQC is attractive because cluster states are considered to be easy to create on systems ranging from the polarization state of photons^[35] to Josephson junction qubits^[92].

A cluster state can be built on a two-dimensional rectangular lattice with Manhattan geometry, in which nodes in the interior of the plane have four neighbors, north, east, south, and west. Some of the qubits in the cluster state are data qubits, while the rest are created in a generic entangled state. Employing quantum correlations for quantum computation, quantum gates on the data qubits can be executed by measuring lattice qubits in a particular basis. All gates in the Clifford group, including CNOT, can be performed in one time step via

a large number of concurrent measurements. Remarkably, because both wires and SWAP gates are in the Clifford group, MBQC supports long-distance gates in a single time step even when the cluster state is built on a physical system permitting only nearest-neighbor interactions.¹

The Toffoli Phase gate, which is not in the Clifford group, can be executed in two time steps, where the measurement basis for the second step is selected depending on previous measurement outcomes. This adaptive process, which must be cascaded through most interesting quantum circuits, determines the overall performance of many algorithms.

Thus, a cluster state can be used to execute arbitrary quantum algorithms. MBQC algorithms are often created by mapping known quantum circuits onto the cluster state. The challenge is to find application algorithms that match the strengths of MBQC. Here, we choose to address the problem of integer addition.

Addition is a critical subroutine for algorithms such as Shor’s algorithm for factoring large numbers^[93-96]. Addition can be executed in many ways, with its performance being primarily dependent on carry propagation, which is normally limited by the physical architecture^[97,98]. The simplest method is ripple-carry addition, which has depth of $\Theta(n)$ ^[94,95,99,100] to add two n -bit numbers. In a ripple-carry adder, carry information is propagated from the low-order qubits to the high order qubits one step at a time.

The goal of our work is to reduce the execution time of addition on MBQC. Raussendorf *et al.* successfully mapped the VBE ripple-carry adder to MBQC bending the circuit layout to reduce the spatial resources^[21,94]. However, a ripple-carry adder does not take good advantage of the strengths of MBQC. By unifying the quantum carry-lookahead adder (QCLA)^[101] with MBQC, we have designed a much faster circuit for large n . In this chapter, we present our design for the MBQCLA and evaluate the design in terms of its execution speed and resource requirements. The depth and spatial optimizations are also discussed. Several results which are analytically shown are the physical resources formulation of the

¹In this chapter, we focus on the quantum rather than classical aspects of the system; a Pauli frame correction based on measurement results may be necessary and will be limited by classical signal propagation time. Thus, single time step wires depend on the assumption that classical signal propagation is fast compared to quantum measurements and gates.

circuits and the circuit models and designs, while the resources comparison and the size of the circuits for n -qubits are numerically derived.

The chapter is organized as follows: the basic notion of quantum carry-lookahead adder are given in Section (3.2). Section (3.3) contains the implementation of MBQC form for QCLA circuits. Here, the out-of-place, in-place, and the optimized version of in-place circuits are discussed to obtain their performances and requirements. Subsection (1.3.1) gives a detailed exposition of a NOT gate in cluster state and the graphical notation used in this chapter, which was created by Raussendorf, Browne, and Briegel^[21]. Subsection (3.2.2) contains the procedures to implement the out-of-place and in-place QCLAs in abstract quantum circuit form. Subsection (3.3.3) provides the requirements and performance for MBQCLA circuits. The limitations and future works are provided in Section (3.4).

3.2 Background

Our proposed circuits build on two concepts: (a) measurement-based quantum computation (as explained in Subsection (1.3.1)), and (b) the quantum carry-lookahead adder. In this Section, we will present a short review of quantum carry-lookahead adder.

3.2.1 Quantum carry-lookahead adder

The Quantum Carry-Lookahead Adder (QCLA) was designed by Draper *et al.*^[101] The quantum carry-lookahead adder is potentially more efficient than a quantum ripple-carry adder since its depth is $\Theta(\log(n))$. A carry-lookahead adder uses three phases, the “Generate” (G), “Propagate” (P), and “Kill” (K) networks, each of which progressively doubles the length of its span in each time step, to calculate the complete “Carry” values (C). In practice, the networks are somewhat redundant, and Draper *et al.* defined their circuit using only the P and G networks to calculate the final carry C. The out-of-place form of the QCLA performs the unitary transformation $|a, b, 0\rangle \longrightarrow |a, b, a + b\rangle$, and the in-place form calculates $|a, b\rangle \longrightarrow |a, a + b\rangle$ where $|a\rangle, |b\rangle$ and $|a + b\rangle$ are n -qubit registers, and we number the low-order qubit 0 and the the high-order qubit $n-1$.

The carry-lookahead adder starts with an initial addition round, consisting of a half adder for each qubit in the logical register. Starting from the basic idea of the carry-lookahead adder originally designed for classical binary logic^[102], the carry is propagated from bit to bit $i \rightarrow j \rightarrow k$, where $i \leq j \leq k$, so carry equations or majority blocks are represented by:

$$c_j = g[i, j] \oplus p[i, j] \wedge c_i \quad (3.1)$$

$$c_k = g[j, k] \oplus p[j, k] \wedge c_j \quad (3.2)$$

By straightforward substitution of these equations, we have the equation:

$$c_k = g[j, k] \oplus p[j, k] \wedge (g[i, j] \oplus p[i, j] \wedge c_i) \quad (3.3)$$

or

$$c_k = g[j, k] \oplus p[j, k] \wedge g[i, j] \oplus p[i, j] \wedge p[j, k] \wedge c_i. \quad (3.4)$$

Substituting $c_k = g[j, k] \oplus p[j, k] \wedge c_i$ into Eq.(3.4) gives:

$$g[i, k] = g[j, k] \oplus p[j, k] \wedge g[i, j]. \quad (3.5)$$

A circuit that performs this computation in a lookahead adder is called the Generate network. Similarly, a circuit that implements the equations

$$p[i, k] = p[i, j] \wedge p[j, k] \quad (3.6)$$

for any $i < j < k$ is called the Propagate network. The implementation of these networks in reversible computation is realized by the following steps where n is logical qubits, t is the round number and m is the index of qubits in the register:

1. *P*-rounds. For $t=1$ to $\lfloor \log n \rfloor - 1$: for $1 \leq m < \lfloor n/2^t \rfloor$. Then the connection between the steps in this round is expressed by: $P_t[m] \oplus = P_{t-1}[2m] P_{t-1}[2m+1]$.
2. *G*-rounds. For $t=1$ to $\lfloor \log n \rfloor$: for $0 \leq m < \lfloor n/2^t \rfloor$. The relation between the steps in the round is: $G[2^t m + 2^t] \oplus = G[2^t m + 2^{t-1}] P_{t-1}[2m+1]$.
3. *C*-rounds. For $t = \lfloor \log 2n/3 \rfloor$ down to 1: for $1 \leq m < \lfloor (n-2^{t-1})/2^t \rfloor$. The connection between the steps in the round is represented by: $G[2^t m + 2^{t-1}] \oplus = G[2^t m] P_{t-1}[2m]$.

These networks will be applied to out-of-place and in-place QCLA circuits. Those circuits are explained in more detail in below.

3.2.2 Out-of-place and in-place procedures for abstract quantum carry-lookahead adder

Here we summarize the QCLA circuits as proposed by Draper *et al.*^[101]. The circuit for out-of-place addition has the form:

1. For $0 \leq i < n$, $Z[i+1] \oplus = A[i]B[i]$ setting $Z[i+1] = g[i, i+1]$.
2. For $0 \leq i < n$, $B[i] \oplus = A[i]$ setting $B[i] = p[i, i+1]$ for $i > 0$ needed to run out-of-place addition circuit.
3. Run the circuit of the P,G, and C networks. Upon completion, $Z[i] = c_i$ for ≥ 1 .
4. For $1 \leq i < n$, $Z[i] \oplus = B[i]$. Now for $i > 0$, $Z[i] = a_i \oplus b_i \oplus c_i = s_i$. For $i=0$, $Z[i] = b_i$.
5. Set $Z[0] \oplus = A[0]$. For $1 \leq i < n$, $B[i] \oplus = A[i]$. This fixes $Z[0]$, and resets B to initial value.

The addition circuit for in-place operation has form:

1. For $0 \leq i < n$, $Z[i+1] \oplus = A[i]B[i]$ setting $Z[i+1] = g[i, i+1]$.
2. For $0 \leq i < n$, $B[i] \oplus = A[i]$ setting $B[i] = p[i, i+1]$ for $i > 0$ and $B[0] = s_0$.
3. Run the circuit of the P,G, and C networks. Upon completion, $Z[i] = c_i$ for ≥ 1 .
4. For $1 \leq i < n$, $B[i] \oplus = Z[i]$. Now $B[i] = s_i$.
5. For $0 \leq i < n-1$, $\neg B$ contains s' .
6. For $1 \leq i < n-1$, $B[i] \oplus = A[i]$.
7. Run the P, G, and network in reverse. Upon completion, $Z[i+1] = a_i s'_i$ for $0 \leq i < n-1$, and $B = a_i \oplus s'_i$ for $1 \leq i < n$.
8. For $1 \leq i < n-1$, $B[i] \oplus = A[i]$.
9. $0 \leq i < n-1$, $Z[i+1] \oplus = A[i]B[i]$.

10. $0 \leq i < n-1, \neg B$.

The resources for each quantum gates in the abstract in-place QCLA circuit is provided in the below table:

| Quantum Gate | Resource |
|--------------|---|
| NOT | $2n-2$ |
| CNOT | $4n-5$ |
| TPG | $10n-3w(n)-3w(n-1)-3\lfloor \log(n) \rfloor - 3\lfloor \log_2(n-1) \rfloor - 7$ |

Table 3.1: Logic gates resources in abstract in-place QCLA. CNOT is **Controlled-NOT** gate and TPG is Toffoli Phase gate as described in Subsection (1.1.2).

3.2.3 MBQC as solution for long-distance communication in nearest-neighbor architectures

The QCLA circuit explained above is one example of a circuit design that assumes communication between non-adjacent qubits is allowed. However, scalable quantum computers may allow only nearest-neighbor interactions^[34]. The depth complexity of a circuit on a Nearest-Neighbor (NN) architecture may be larger than non-NN architectures. Under some circumstances, MBQC gives us a trade off between depth and space complexity^[103]: one can reduce the circuit depth by adding a number of measurements, entanglements, and byproduct operations in the quantum circuit.

The out-of-place and in-place QCLA respectively have the overall depth $\lfloor \log_2(n) \rfloor + \lfloor \log_2(n/3) \rfloor + 4$ and $\lfloor \log_2(n) \rfloor + \lfloor \log_2(n-1) \rfloor + \lfloor \log_2(n/3) \rfloor + \lfloor \log_2 \frac{n-1}{3} \rfloor + 8$. However, these abstract quantum circuits assumed unrealistic conditions: interactions between non-adjacent qubits can be perfectly implemented. When application qubits are assigned positions in a quantum computer, some qubits we wish to interact may be widely separated; examining the circuit diagram for QCLA shows many long-distance gates crossing over many other qubits. In a nearest-neighbor architecture, we must swap qubits, step by step, until our desired qubits

become neighbors. On a single line, the $\Theta(\log_2(n))$ time steps for QCLA expands to $\Theta(n)$.^[98]

3.3 Quantum carry-lookahead adder for measurement-based quantum computation

This section explains the implementation of QCLA for MBQC. The performance and requirements for both out-of-place and in-place MBQCLA circuits schemes are evaluated. First we describe our metrics for evaluating circuits. The exposition of direct mapping on both schemes is given, followed by the optimization for the in-place circuit. The optimization is done by adjusting the border between the rounds of the circuit, then removing the unnecessary lattice sites between the quantum gates, reducing the communication costs in the circuit. For comparison, a graph state form of QCLA is also presented. More detailed results are presented in Subsection (3.3.3).

3.3.1 Evaluating algorithms executed using MBQC

Logical quantum circuits can be evaluated based on the execution time, or *circuit depth* (usually measured in numbers of Toffoli gates), number of qubits used, and total number of gates executed. The number of logical qubits is the number of required input qubits plus the number of ancillae required in the circuit representation of the algorithm.

We propose the use of (a) the number of qubits in the cluster state, (b) the number of clustering operations, (c) circuit area, and (d) circuit depth as measures of performance and cost for algorithms executed using MBQC. The number of cluster operations is the number of successful interactions needed. The circuit area is the height of the cluster times its width, assuming a regular rectangular lattice. All of these measures can be expressed in terms of problem size; in our case, in terms of n , the length of each of the logical registers being added.

The goal of this chapter is to minimize the execution time (d), while the other three (a-c) are measures of the cost. These costs, as shown in Fig. (3.1), can be divided into two categories: *first*, *computational resources*, i.e., the

3.3 Quantum carry-lookahead adder for measurement-based quantum computation

number of cluster qubits required for Toffoli Phase, CNOT and NOT gates. *Second, communication resources*, i.e., the number of cluster qubits required for SWAP gates and wires. A circuit which uses no communication resources is called an **optimal circuit**. As noted above, MBQC requires a measure-adapt-measure cycle to implement non-Clifford gates. The execution time is the number of rounds of measurement, followed by computation of the adaptive bases for the next round.

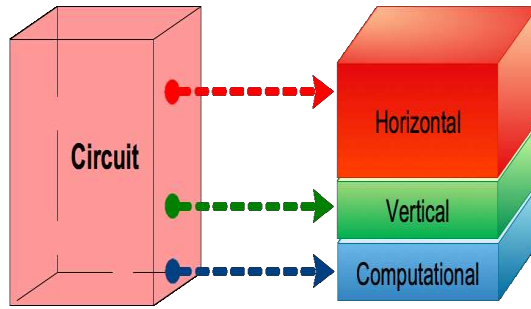


Figure 3.1: Illustration for circuit costs for MBQCLA. On a two-dimensional Manhattan grid, the costs contain computational and communication costs. The resources for communication costs can be separated into two types of resources: horizontal (wires) and vertical (SWAP gates).

In general, the optimal circuit resources can be determined by summing the resources consumed by the various types of computational gates. Thus, it is expressed by

$$\sum_{i \in \text{Quantum Gate}} \mathcal{X}_i \mathcal{R}_i \quad (3.7)$$

where

- \mathcal{X}_i = Number of quantum gates of type i
- \mathcal{R}_i = Qubit resources for an i gate

Because the QCLA is structured in a set of rounds, each of which contains only gates of a single type (e.g. Toffoli Phase Gate), we can discuss the cost in those terms. The cost of a null circuit would simply be the number of logical

3.3 Quantum carry-lookahead adder for measurement-based quantum computation

qubits multiplied by the cost of a horizontal wire. In an actual circuit, we replace some Sections of horizontal wire with logical gates, and add vertical wires with SWAP gates as necessary to implement the logic. Thus, each round in the QCLA, when mapped onto the cluster state, is as wide as necessary to accommodate the necessary gate type.¹

By considering the number of SWAP, Toffoli and CNOT gates in the initial addition circuit and in P,G and C networks as shown above, we can approximate the physical resources needed for an n -qubit out-of-place MBQCLA following this expression:

$$Size \approx \sum_i (\mathcal{V}(n) \times \mathcal{B}_i(n) \times \mathcal{T}_i + \mathcal{X}_i(n) (\mathcal{R}_i - \mathcal{E}_i \times \mathcal{T}_i)) + \mathcal{R}_{SWAP} \times \mathcal{S}_{SWAP} \quad (3.8)$$

where $i \in \{\text{Toffoli Phase, CNOT, and NOT Gates}\}$, $\mathcal{V}(n)$ = number of logical qubits, $\mathcal{B}_i(n)$ = number of rounds for the gate of type i , $\mathcal{X}_i(n)$ = number of gates of type i , \mathcal{T}_i = width of the i -gate (in lattice sites), \mathcal{R}_i = number of lattice qubits in an i -gate, \mathcal{E}_i = number of logical qubits in an i -gate (generally, one to three), \mathcal{R}_{SWAP} is the number of lattice qubits in a cluster state SWAP gate and \mathcal{S}_{SWAP} = number of SWAP gates in a QCLA circuit, which is dependent on the mapping of the logical qubits to positions on the lattice.

In Eq. (3.8), $\sum_i (\mathcal{V}(n) \times \mathcal{B}_i \times \mathcal{T}_i)$ is the cost of a lattice large enough to hold all of the circuit rounds that use type i -gates (that is horizontal communication costs). $-\sum_i \mathcal{E}_i \times \mathcal{X}_i \times \mathcal{T}_i$ is an adjustment for replacing wires with logic gates. $\mathcal{R}_{SWAP} \times \mathcal{S}_{SWAP}$, which depends on type of rounds in QCLA circuit, is the vertical communication in the circuit, which is entirely SWAP gates resources.

Proposed implementations of cluster state quantum computing in solid-state technologies, which need an Ising-like Hamiltonian^[40,92,104–106], operate on a fixed 2-D lattice. Hence, they require wires for communication between the rounds, which means those proposals will use our optimized circuit. A photonic-based quantum computer^[41,42] will require no wires for communication between the rounds, allowing the optimal circuits or graph state form to be used more or less directly.

¹Usually the width of a Toffoli gate.

3.3.2 Out-of-place measurement-based quantum carry-lookahead adder

Our design for a 10-bit form of the out-of-place QCLA on MBQC is shown in Fig. (3.2). The input qubits are on the left (top in the rotated figure) and output states are on the right. In the figures in this chapter, a pink square qubit represents a cluster qubit measured in the σ_x -eigenbasis, a green qubit is for π -rotation on σ_x -eigenbasis measurement, a red qubit is for σ_y -eigenbasis measurement and a blue qubit is for σ_z -eigenbasis measurement^[21], as described in Subsection (1.3.1). The propagation pattern of one logical qubit is highlighted in yellow. Our logical qubits are spaced with a pitch of four lattice sites to accommodate the necessary spacing between gates. Each large box outlines one round in the P, G or C networks. The circuit is presented in unoptimized form for clarity.

This circuit is essentially a direct mapping of the abstract out-of-place QCLA to MBQC. The logical gates used are those described in Fig. (1.10) in Subsection (1.3.1). As noted above, in addition to the computational resources, we must add wires and SWAP gates. The long distance gates from the abstract out-of-place QCLA are executed using the scheme for non-adjacent computation Fig. (1.11). To completely characterize the circuit, we need to know how many SWAP gates and wire segments are added to complete the circuit. The exact cost depends on the layout of logical qubits. Below we calculate the number of SWAP gates required assuming the data layout of Fig. (3.2).

The abstract circuit consists of addition and carry computation circuits. For adding two n -qubit registers, the addition circuit is built from n Toffoli gates and $3n-1$ CNOT gates while the carry computation machinery consists of $4n-3w(n)-3\lfloor \log_2(n) \rfloor - 1$ Toffoli gates. The number of Toffoli gates in this circuit can be obtained by adding the number of Toffolis in the addition, P, G, and C networks. For the out-of-place QCLA circuit, we have $n-w(n)-\lfloor \log_2(n) \rfloor$ Toffoli gates for the P network, $n-w(n)$ Toffoli gates for the G network and $n-\lfloor \log_2(n) \rfloor - 1$ for C network, where $w(n)$ is the Hamming weight of the binary representation of n . Furthermore, the number of SWAP gates, which is the vertical communication resources, can be obtained as follows:

3.3 Quantum carry-lookahead adder for measurement-based quantum computation

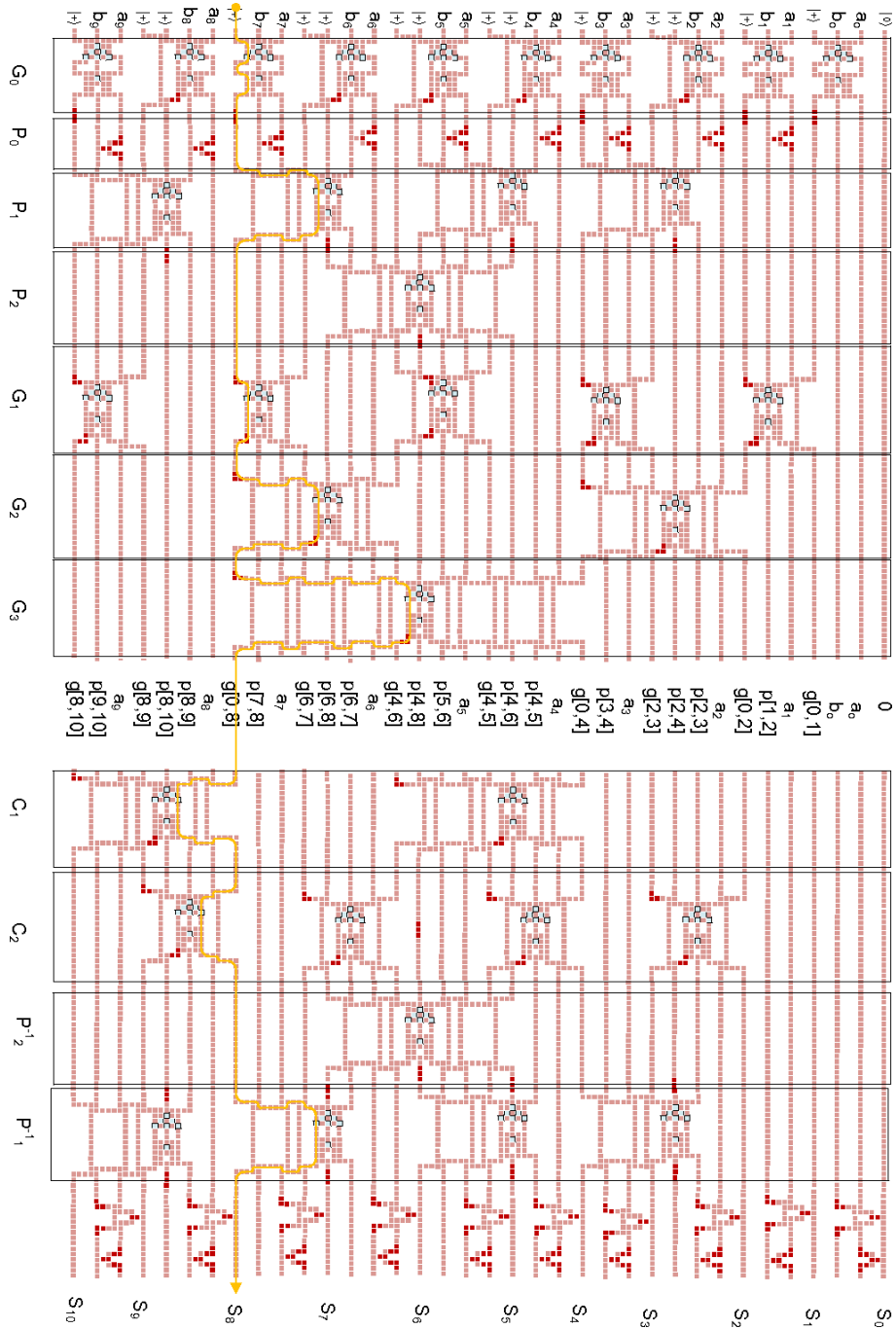


Figure 3.2: Out-of-place MBQCLA. For $n=10$, the circuit consists of: 4 addition blocks, 9 rounds of gates for the carry networks (2 Propagate, 3 Generate, 2 Inverse Propagate and 2 Carry networks). For explanation of the colors, see Subsection (1.3.1).

3.3 Quantum carry-lookahead adder for measurement-based quantum computation

- The initial addition round needs

$$\mathcal{S}_{Ad} = 4n - 2w(n) - 2\lfloor \log_2(n) \rfloor \quad (3.9)$$

SWAP gates. For $n=10$, we need 30 SWAP gates consuming 360 lattice qubits.

- The propagate network needs 28 SWAP gates for $n=10$. This number can be obtained from the number of Toffoli gates for each round, $\lfloor n/2^{t_p} \rfloor - 1$ where t_p is the round number in the propagate network, $1 \leq t_p \leq \lfloor \log_2(n) \rfloor - 1$. There are 4 Toffoli gates in the first P round with 16 SWAP gates and 1 Toffoli gate in the second P round with 12 SWAP gates. The vertical communication in P networks is

$$\mathcal{S}_p = \sum_{t_p=1}^{\log_2(n)-1} 2n - 2^{t_p+1} \quad (3.10)$$

- Similarly, the generate network requires 58 SWAP gates for $n=10$. The number of Toffoli gates for each round is $5n + w(n) + 2\lfloor \log_2(n) \rfloor$. As formulated by $\lfloor n/2^{t_g} \rfloor$, we have three rounds of generate networks; the first round consists of 5 Toffoli gates with 12 SWAP gates, the second round needs 2 Toffoli gates with 20 SWAP gates and the third round requires 1 Toffoli gate with 26 SWAP gates. The SWAP gates resources in the G network can be approximated by

$$\mathcal{S}_g = \sum_{t_g=1}^{\log_2(n)} 4\lfloor \log_2(n) \rfloor + 2^{t_g+1}\lfloor \log_2(t_g) \rfloor \quad (3.11)$$

where t_g is the round in the G network.

- The number of Toffoli gates in the carry network is $\lfloor \frac{n-2^{t_c}-1}{2^{t_c}} \rfloor$. Therein, the first Carry round has 4 Toffoli gates with 16 SWAP gates and its second round has 22 SWAP gates. The resources of SWAP gates in the C network is

$$\mathcal{S}_c = \sum_{t_c=1}^{\lfloor \log_2 \frac{2n}{3} \rfloor} 2n - 2\lfloor \log_2(t_c) \rfloor \quad (3.12)$$

where t_c is the round number in the C network.

3.3 Quantum carry-lookahead adder for measurement-based quantum computation

Following Eq. (3.8), \mathcal{S}_{SWAP} is the sum of Eqs. (3.9), (3.10), (3.11), and (3.12)

$$\mathcal{S}_{SWAP} = \mathcal{S}_{Ad} + \mathcal{S}_p + \mathcal{S}_g + \mathcal{S}_e. \quad (3.13)$$

For the out-of-place MBQCLA, we see that the depth is reduced to $\lfloor \log_2(n) \rfloor + \lfloor \log_2(n/3) \rfloor + 7$ compared to $\approx 3n$ for the VBE ripple-carry. However, this circuit costs more in physical resources, $\approx 901n + 224n \times \lfloor \log_2(n) \rfloor$ compared to $\approx 304n$ for the VBE ripple-carry. The comparison of size and depth between MBQC VBE and MBQCLA is shown in Fig. (3.3).

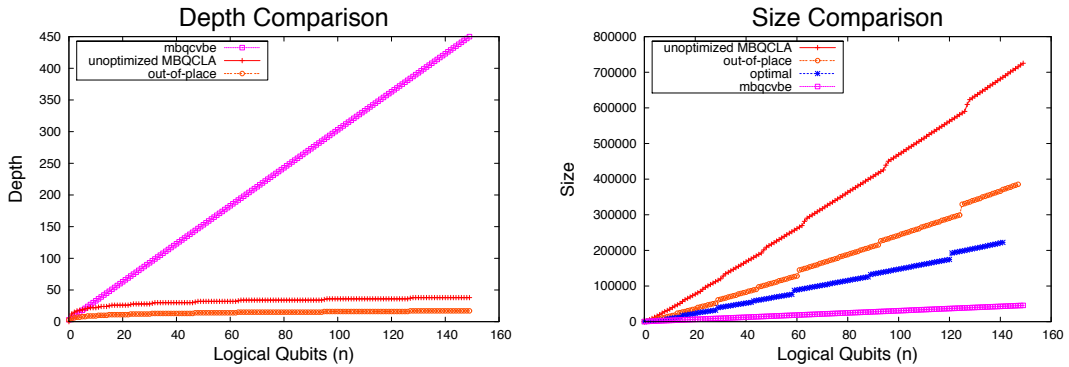


Figure 3.3: Size and depth comparison between MBQC VBE and MBQCLA. “+”, “✱”, “o” and “□” marks are for in-place, optimized in-place, out-of-place and MBQC VBE circuits, respectively.

3.3.3 In-place Measurement-based quantum carry-lookahead adder

The next step is obtaining the performance and requirements of the in-place quantum carry look-ahead adder. Following the scheme in Ref.^[101], the erasure (uncomputation) of the low-order $n-1$ bits of the carry string c requires additional circuitry. The algorithm for the in-place form is more complex than out-of-place and uses about twice as many Toffoli gates.

The subsequent procedures, as provided in Subsection (3.2.2), give in-place MBQCLA circuit horizontal resources, as summarized in Table (3.3) (Subsection

3.3 Quantum carry-lookahead adder for measurement-based quantum computation

(3.3.3)). As shown in the previous Section, the vertical communication resources can be estimated by counting the number of SWAP gates in the circuit. Because the in-place circuit uses more ancillae, which we interleave with the other qubits, the number of SWAP gates for the initial round of half-adders increases to $6n-4w(n)-4\lfloor\log n\rfloor-2$. The other SWAP gate resources can be obtained by examining the Propagate, Generate, and Carry networks. In the in-place circuit we need both for computing and uncomputing the carry status, meaning $8n+14\lfloor\log n\rfloor+2$ SWAP gates are needed for non-adjacent quantum computation. Straightforwardly, the physical resources for in-place circuit are

$$\approx 2896n + 64n\lfloor\log_2(n)\rfloor. \quad (3.14)$$

Also, by the use of Eqs. (3.9), (3.10), (3.11), and (3.12) for the out-of place circuit, the vertical communication resources (SWAP gates), or \mathcal{S}_{SWAP} for in-place MBQCLA circuit is

$$\mathcal{S}_{SWAP} = \mathcal{S}_{Ad} + \mathcal{S}'_{Ad} + 4\mathcal{S}_p + 2\mathcal{S}_g + 2\mathcal{S}_c \quad (3.15)$$

where $\mathcal{S}'_{Ad} = \sum_{i=1}^n 2(n-1)$, is an additional column required to perform an in-place circuit.

It is also useful to calculate the optimal in-place MBQCLA circuit resources. According to Eq. (3.7),

$$\mathcal{S}_{optimal} = \mathcal{X}_{TPG}\mathcal{R}_{TPG} + \mathcal{X}_{CNOT}\mathcal{R}_{CNOT} + \mathcal{X}_{NOT}\mathcal{R}_{NOT}. \quad (3.16)$$

By the use of Table (3.1), one can obtain

$$\mathcal{S}_{optimal} = 162(w(n) + \lfloor\log_2(n-1)\rfloor + \lfloor\log_2(n)\rfloor - w(n-1)) + 542n - 395. \quad (3.17)$$

To summarize, the following tables are the quantitative expressions for out-of-place and in-place MBQCLA circuits:

3.3 Quantum carry-lookahead adder for measurement-based quantum computation

| Parameter | Value |
|---------------------------------------|--|
| Pitch | 4 |
| Variables (Logical Qubits) | $\mathcal{V}(n) = 4n - \lfloor \log_2 n \rfloor + 1$ |
| Width | $Width(n) = 15 \times (\lfloor \log_2(n) \rfloor + \lfloor \log_2(n/3) \rfloor) + 85$ |
| Height | $Height(n) = 4 \times (4n - w(n) - \lfloor \log_2 n \rfloor + 1) - 3$ |
| Area | $Height(n) \times Width(n) =$ $(4 \times (4n - w(n) - \lfloor \log_2 n \rfloor + 1) - 3) \times$ $(14 \times (\lfloor \log_2(n) \rfloor + \lfloor \log_2(n/3) \rfloor) + 85)$ |
| Number of Clustering Operations | $(4n - w(n) - \lfloor \log_2 n \rfloor + 1) \times$ $(15 \times \lfloor \log_2(n) \rfloor + \lfloor \log_2(n/3) \rfloor + 85) - 1) +$ $(15 \times \lfloor \log_2(n) \rfloor + \lfloor \log_2(n/3) \rfloor + 85) \times$ $(4n - w(n) - \lfloor \log_2 n \rfloor)$ |
| Circuit Depth | $\lfloor \log_2(n) \rfloor + \lfloor \log_2(n/3) \rfloor + 7$ |
| Size (Number of Qubits) | $-3271 + 899n - 419w(n) - 377 \lfloor \log_2(n) \rfloor + 56n \lfloor \log_2(2n/3) \rfloor - 14w(n) \lfloor \log_2(2n/3) \rfloor$ $+ 42n \lfloor \log_2(n) \rfloor + 168n \lfloor \log_2(n) \rfloor - 14 \lfloor \log_2(2n/3) \rfloor \lfloor \log_2(n) \rfloor - 42 \lfloor \log_2(n) \rfloor^2$ $+ 6 \times (2n + \sum_{t_p=1}^{\log_2(n-1)} 2(n-2^{t_p}) + \sum_{t_g=1}^{\log_2(n)} 2(2(\lfloor \log_2(n) \rfloor) + (2^{t_g})(\lfloor \log_2(t_g) \rfloor))$ $+ \sum_{t_c=1}^{\lfloor \log_2 \frac{2n}{3} \rfloor} 2(n - \lfloor \log_2(t_c) \rfloor))$ |

Table 3.2: Requirements and performance of the out-of-place MBQCLA

3.3 Quantum carry-lookahead adder for measurement-based quantum computation

| Parameter | Value |
|---------------------------------|--|
| Pitch | 4 |
| Variables (Logical Qubits) | $\mathcal{V}(n) = 4n - \lfloor \log_2 n \rfloor + 1$ |
| Width | $Width(n) = 15 \times (\lfloor \log_2 n \rfloor + \lfloor \log_2(n-1) \rfloor + \lfloor \log_2 \frac{n}{3} \rfloor + \lfloor \log_2 \frac{n-1}{3} \rfloor) + 157$ |
| Height | $Height(n) = 4 \times (4n - w(n) - \lfloor \log_2 n \rfloor + 1) - 3$ |
| Area | $Height(n) \times Width(n) =$ $(4 \times (4n - w(n) - \lfloor \log_2 n \rfloor + 1) - 3) \times$ $15 \times (\lfloor \log_2 n \rfloor + \lfloor \log_2(n-1) \rfloor + \lfloor \log_2 \frac{n}{3} \rfloor + \lfloor \log_2 \frac{n-1}{3} \rfloor) + 157$ |
| Number of Clustering Operations | $(4n - w(n) - \lfloor \log_2 n \rfloor + 1) \times$ $(15 \times (\lfloor \log_2 n \rfloor + \lfloor \log_2(n-1) \rfloor + \lfloor \log_2 \frac{n}{3} \rfloor + \lfloor \log_2 \frac{n-1}{3} \rfloor) + 156) +$ $(15 \times (\lfloor \log_2 n \rfloor + \lfloor \log_2(n-1) \rfloor + \lfloor \log_2 \frac{n}{3} \rfloor + \lfloor \log_2 \frac{n-1}{3} \rfloor) + 157) \times$ $(4n - w(n) - \lfloor \log_2 n \rfloor)$ |
| Circuit Depth | $\lfloor \log_2 n \rfloor + \lfloor \log_2(n-1) \rfloor + \lfloor \log_2 \frac{n}{3} \rfloor + \lfloor \log_2 \frac{n-1}{3} \rfloor + 14$ |
| Size (Number of Qubits) | $-3068 + 2896n - 138w(n-1) - 162w(n) + 16 \lfloor \log_2 \frac{n-1}{3} \rfloor$ $+ 64n \lfloor \log_2 \frac{n-1}{3} \rfloor - 146 \lfloor \log_2(n-1) \rfloor$ $+ 64n \lfloor \log_2(n-1) \rfloor + 16 \lfloor \log_2(n/3) \rfloor + 64n \lfloor \log_2(n/3) \rfloor$ $+ 21 \lfloor \log_2(n) \rfloor + 64n \lfloor \log_2(n) \rfloor$ $- 16 \lfloor \log_2(n-1) \rfloor \lfloor \log_2(n) \rfloor - 16 \lfloor \log_2 \frac{n}{3} \rfloor \lfloor \log_2(n) \rfloor - 16 \lfloor \log_2(n) \rfloor^2 +$ $6 \times (4n - 1 + 4 \sum_{t_p=1}^{\log_2(n-1)} 2^{(n-2^{t_p})} + 2 \sum_{t_g=1}^{\log_2(n)} 2^{(2(\lfloor \log_2(n) \rfloor) +$ $(2^{t_g})(\lfloor \log_2(t_g) \rfloor) + 2 \sum_{t_c=1}^{\lfloor \log_2 \frac{2n}{3} \rfloor} 2^{(n - \lfloor \log_2 t_c \rfloor)})$ |

Table 3.3: Requirements and performance of the in-place MBQCLA

3.3.4 MBQCLA latencies

As discussed in Section (3.2.3), a carry-lookahead addition in MBQC can reach $O(\log n)$ time due to the constant scale depth of primitive gates in MBQC. The depth of a Toffoli gate in MBQC is 2, and our circuit does not change the original behavior. In addition to the Toffoli-dependent rounds, the QCLA requires a small number rounds of CNOTs and NOTs, each of which adds one to the circuit depth, giving a total of out-of-place and in-place MBQCLA depths of $2(\lfloor \log_2(n) \rfloor + \lfloor \log_2 \frac{2n}{3} \rfloor) + 13$ and $2(\lfloor \log_2(n) \rfloor + \lfloor \log_2(n-1) \rfloor + \lfloor \log_2 \frac{n}{3} \rfloor + \lfloor \log_2 \frac{n-1}{3} \rfloor + 14)$, respectively.

3.3.5 Optimized in-place MBQCLA

We can optimize the MBQCLA spatial resources in several ways. First, by relaxing the Manhattan constraints on the physical geometry, we can use a graph state, which requires fewer communication resources if it can be physically implemented. The graph state adder will be presented in Section (3.3.6).

In this Section, we retain the Manhattan constraint but optimize the circuit. The idea of the bent network^[21], imagining that logical qubits are propagated through traces on a single-layer two-dimensional surface, is used to reduce the horizontal resources of MBQCLA.

3.3.5.1 Bent network in quantum carry-lookahead adder

Contrary to the usual quantum circuit assumption that the horizontal axis relates to logical time, in a “bent” network the temporal axis flows freely in the spatial layout. The consequence is that a more compact circuit can be constructed.

If we apply this bent network method to MBQCLA, we also find that we can reduce the horizontal size of the circuit. The bent form of VBE is purely rectangular, but MBQCLA is not as regular. The horizontal size for every logical qubit position will depend on the number of quantum gates, since it will vary along the register as shown in Fig. (3.6). The illustration of a bent network implementation for $n=10$ is given in Fig. (3.7).

3.3 Quantum carry-lookahead adder for measurement-based quantum computation

3.3.5.2 Optimized circuit formulation

To optimize the circuit, we take small groups of qubits, or subregisters, and slide them toward the middle of the circuit. As can be seen in Fig. (3.7), bending the network can reduce the cluster resources required near qubits $a_0, a_1, a_2, a_3, a_4, a_6, a_8,$ and a_9 by the amount:

$$\sum_{i=0}^{n-1} (\mathcal{C}_i \mathcal{A}_i \mathcal{W}) \quad (3.18)$$

where n = number of logical qubits, \mathcal{C}_i = the number of rounds (columns) that i th-subregister moves, \mathcal{A}_i = number of logical qubits in the i th-subregister (usually 3, sometimes 4), and \mathcal{W} = width of Toffoli Phase Gate. For $n=10$, this manual optimization of horizontal communication results in a reduction of $\approx 12\%$ for spatial resources, or ≈ 3822 qubits.

3.3.6 Graph state quantum carry-lookahead adder (GSQ-CLA)

In the previous Sections, we presented cluster state adders. Here, we present a graph state adder. The GSQCLA is simpler and follows more directly from the original QCLA definition. For MBQC in graph states, we assume that the restriction to Manhattan physical geometry is lifted, and arbitrary entanglement operations between qubits are allowed. The vertices follow the graphical notation of MBQC in cluster states but with the three additional types of vertices: {measured input qubits in an arbitrary angle, $-\frac{\pi}{4}$, and $\frac{\pi}{4}$ } and there are two types of edges : entanglement and input/output information flows. We choose $\mathcal{CNOJ}^{<4>}$ and $\mathcal{CCNOJ}^{<39>}$ for running QCLA. When two GSQC quantum gates are concatenated, the output qubits of one become the input of the other. The bird's eye view of the in-place GSQCLA is given in Fig. (3.8).

The circuit depth of graph state is identical to that of MBQC, so we focus here on the number of qubits and entanglement operations.

Concatenating quantum gates in graph states can reduce the number of qubits whilst the number of entanglement operations is invariant^[39]. The number of

3.3 Quantum carry-lookahead adder for measurement-based quantum computation

entanglement operations in GSQCLA is

$$\sum_k E_k \mathcal{X}_k \quad (3.19)$$

Where $k \in \{\text{Toffoli Phase, CNOT, and NOT Gates}\}$, E_k = the number of entanglement operations in type k gates, and \mathcal{X}_k = the number of gates of type k .

The number of qubit resources before the removal of unnecessary measurement is given by Eq.3.7. After the adjustment, the qubits resources is

$$\sum_m \mathcal{X}_i \mathcal{R}_i - \sum_l \mathcal{N}_l(\mathcal{Q}_P, \mathcal{Q}_G, \mathcal{Q}_C, \mathcal{Q}_{add}) \quad (3.20)$$

where $i \in \{\text{Toffoli Phase, CNOT, and NOT Gates}\}$, \mathcal{N}_l = number of removed qubits of type l circuit and $\mathcal{Q}_P = \sum_{t_p=1}^{\lfloor \log_2(n) \rfloor - 1} 2(\lfloor \frac{n}{2^{t_p}} \rfloor - 1)$, $\mathcal{Q}_G = \sum_{t_g=1}^{\lfloor \log_2(n) \rfloor} 3\lfloor \frac{n}{2^{t_g}} \rfloor$, $\mathcal{Q}_C = \sum_{t_c=1}^{\lfloor \log_2(\frac{2n}{3}) \rfloor - 1} 3\lfloor \frac{(n-2^{t_c-1})}{2^{t_c}} \rfloor$, and \mathcal{Q}_{add} are the number of removed qubits in the P , G , C , and addition rounds in the circuit, respectively. The formulation of \mathcal{Q}_{add} varies depending on the type of circuit.

We know from Table (3.1) that QCLA requires $10n-3w(n)-3w(n-1)-3\lfloor \log_2(n) \rfloor - 3\lfloor \log_2(n-1) \rfloor - 7$ Toffoli Phase Gates and that the Toffoli Phase Gate uses 39 qubits and 43 entangling operations. Therefore, based on the above formulations, the number of entanglement operations for the out-of-place GSQCLA is

$$224n - 129(w(n) - \lfloor \log_2(n) \rfloor) - 46. \quad (3.21)$$

The number of qubits for this circuit is

$$\begin{aligned} & 201n - 117(w(n) - \lfloor \log_2(n) \rfloor) - 2 \sum_{t_p=1}^{\lfloor \log_2(n) \rfloor - 1} 2(\lfloor \frac{n}{2^{t_p}} \rfloor - 1) \\ & - \sum_{t_g=1}^{\lfloor \log_2(n) \rfloor} 3\lfloor \frac{n}{2^{t_g}} \rfloor - \sum_{t_c=1}^{\lfloor \log_2(\frac{2n}{3}) \rfloor - 1} 3\lfloor \frac{(n-2^{t_c-1})}{2^{t_c}} \rfloor - 43, \end{aligned} \quad (3.22)$$

or roughly $201n$ for large n . This formulation is obtained after concatenating the GSQCLA quantum gates and adjusting their qubits resources to form the circuit. Similarly, the in-place GSQCLA has

$$444n - 129(w(n) - w(n-1) - \lfloor \log_2(n) \rfloor - \lfloor \log_2(n-1) \rfloor) - 318 \quad (3.23)$$

3.3 Quantum carry-lookahead adder for measurement-based quantum computation

entanglement operations. The number of qubits for the in-place GSQCLA is

$$410n - 117(w(n) - w(n-1) - \lfloor \log_2(n) \rfloor - \lfloor \log_2(n-1) \rfloor) -$$

$$4 \sum_{t_p=1}^{\lfloor \log_2(n) \rfloor - 1} 2(\lfloor \frac{n}{2^{t_p}} \rfloor - 1) - 2 \sum_{t_g=1}^{\lfloor \log_2(n) \rfloor} 3\lfloor \frac{n}{2^{t_g}} \rfloor - 2 \sum_{t_c=1}^{\lfloor \log_2(\frac{2n}{3}) \rfloor - 1} 3\lfloor \frac{(n - 2^{t_c - 1})}{2^{t_c}} \rfloor - 261, \quad (3.24)$$

about twice the size of the out-of-place version.

3.3.7 Resource comparison

Fig. (3.4) plots the resources required for the in-place MBQCLA, as derived in Eqs. (3.15), (3.17), and (3.14). The red area, which represents the horizontal communication costs of MBQCLA, is $\approx 77\%$ of the qubits in the cluster. The light green area, showing the costs of MBQCLA circuit vertical communication, consumes $\approx 11\%$. The cost of the computational circuit shown by the light blue area is $\approx 12\%$ of the spatial resources. The light yellow area represents the qubits resources for the in-place GSQCLA which costs $\approx 9\%$ in spatial resources.

3.3 Quantum carry-lookahead adder for measurement-based quantum computation

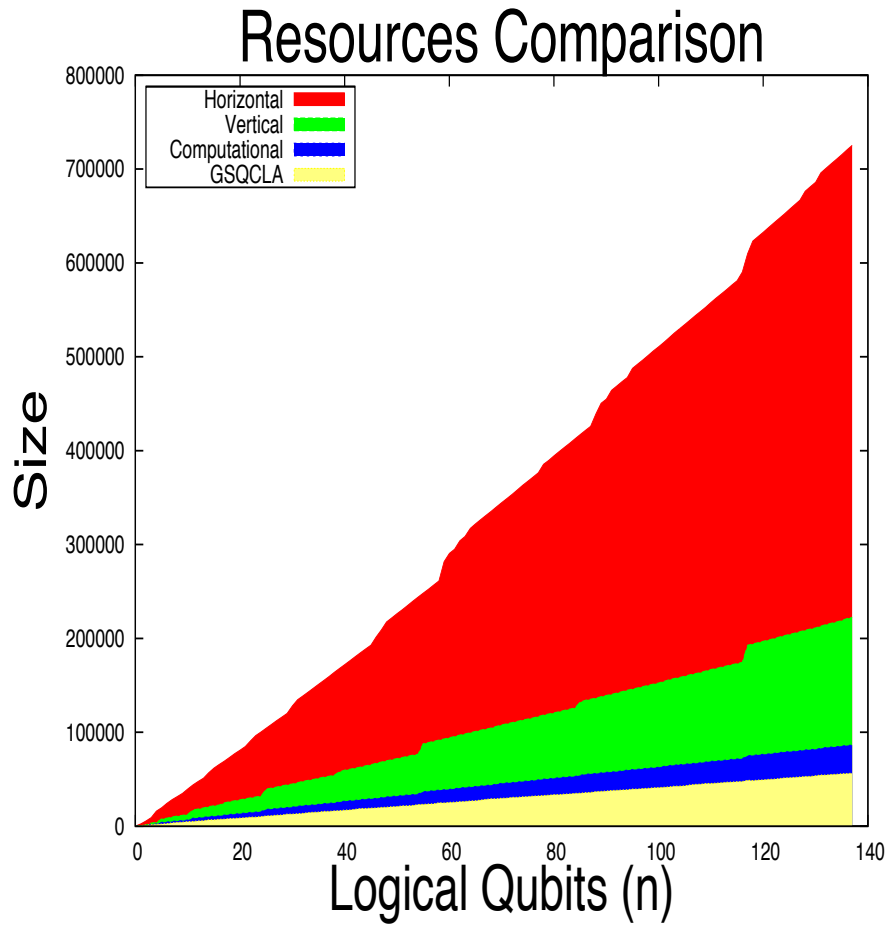


Figure 3.4: Comparison of computational and communication resources in in-place MBQCLA circuit. The bottom line on the graph represents the ideal circumstance for the computational resource and the other two show the circuit with additional resources for the horizontal and the vertical communications.

3.3 Quantum carry-lookahead adder for measurement-based quantum computation

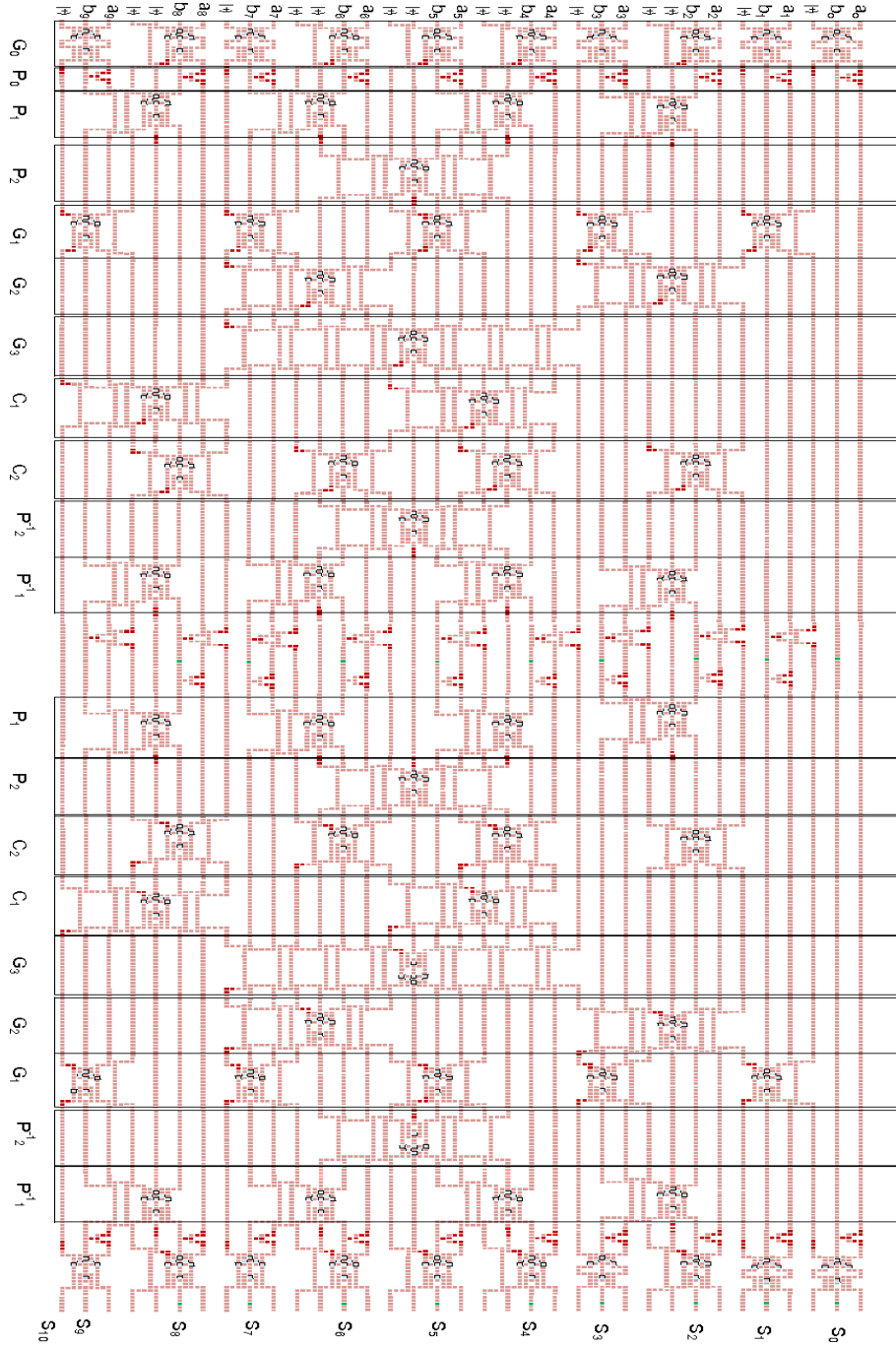


Figure 3.5: In-place MBQCLA. For $n=10$, the circuit consists of:8 addition circuits, 18 carry networks (4 Propagate, 6 Generate, 4 Inverse Propagate and 4 Carry networks)

3.3 Quantum carry-lookahead adder for measurement-based quantum computation

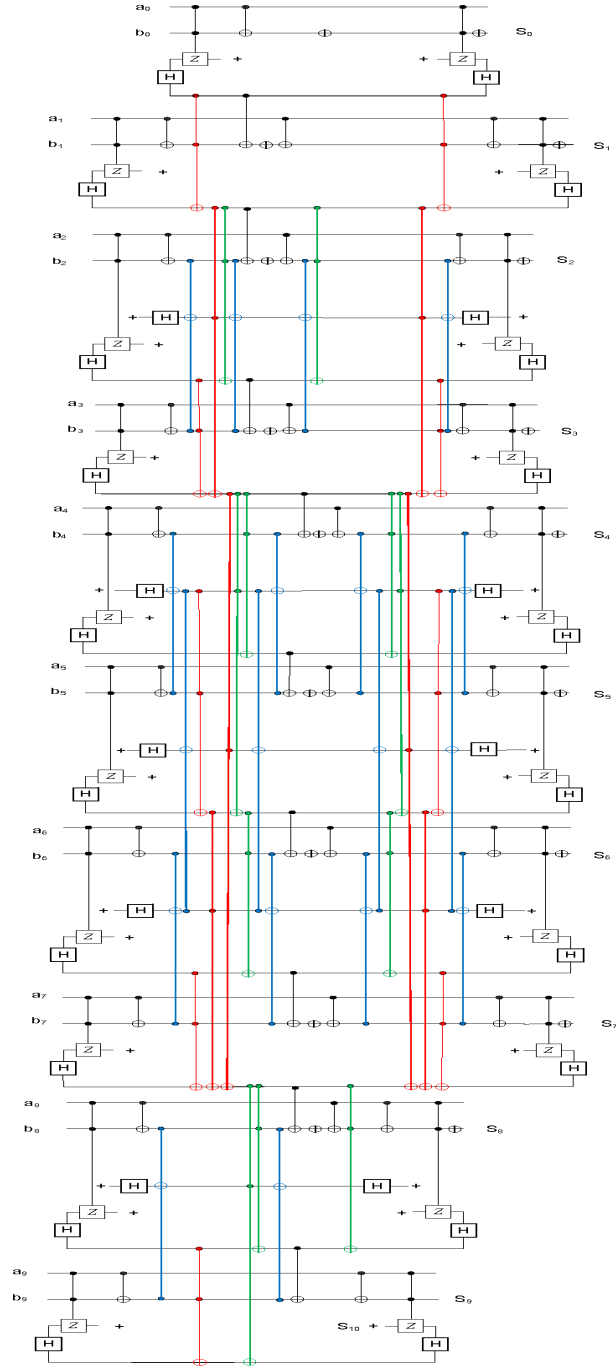


Figure 3.6: Optimized in-place circuit. The low $n-1$ bits of the carry string output are tucked into the interior of the circuit by bending the network.

3.3 Quantum carry-lookahead adder for measurement-based quantum computation

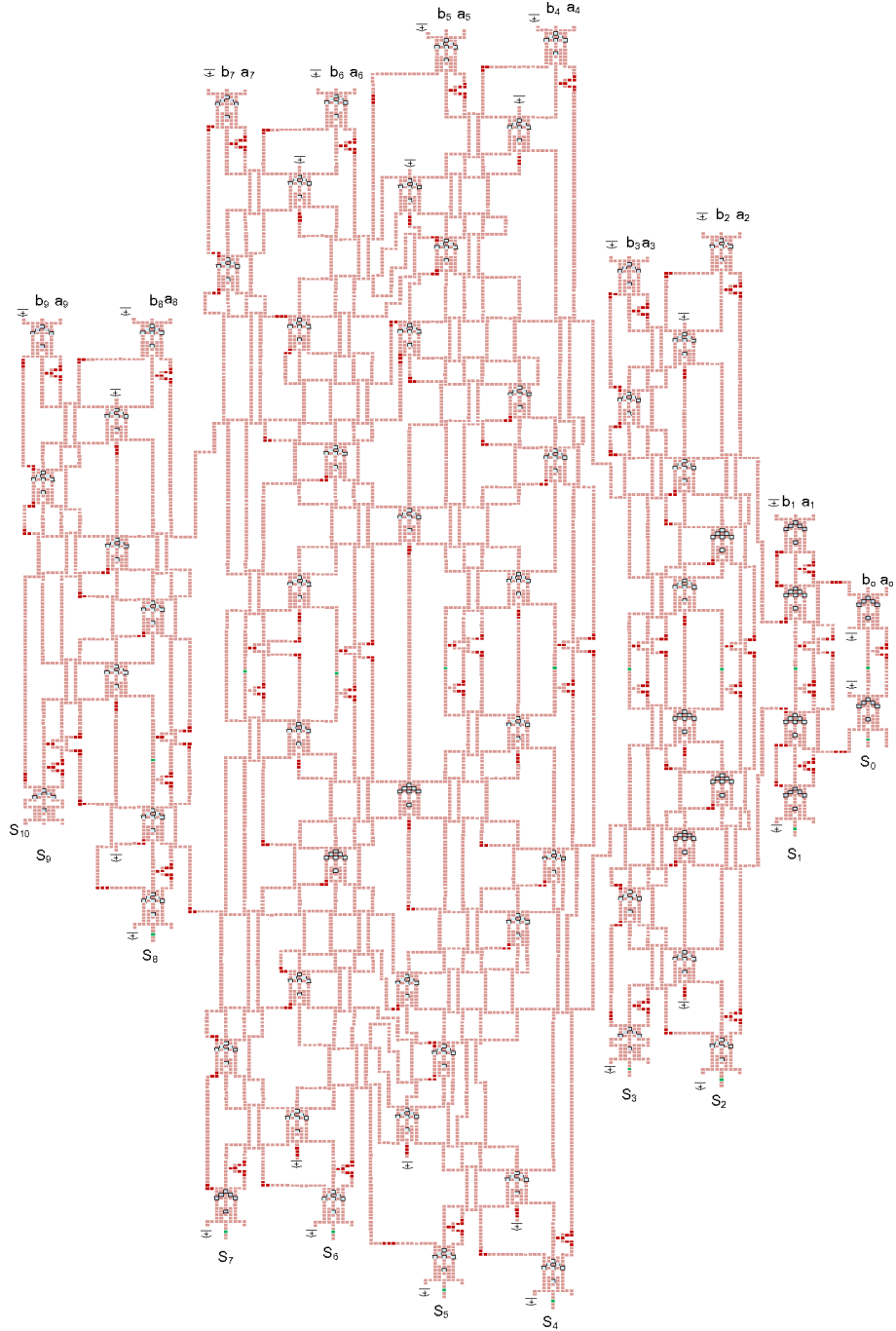


Figure 3.7: The optimized in-place MBQCLA circuit forms a diamond-like circuit. Hand optimization of the circuit reduced the size by $\approx 12\%$.

3.3 Quantum carry-lookahead adder for measurement-based quantum computation

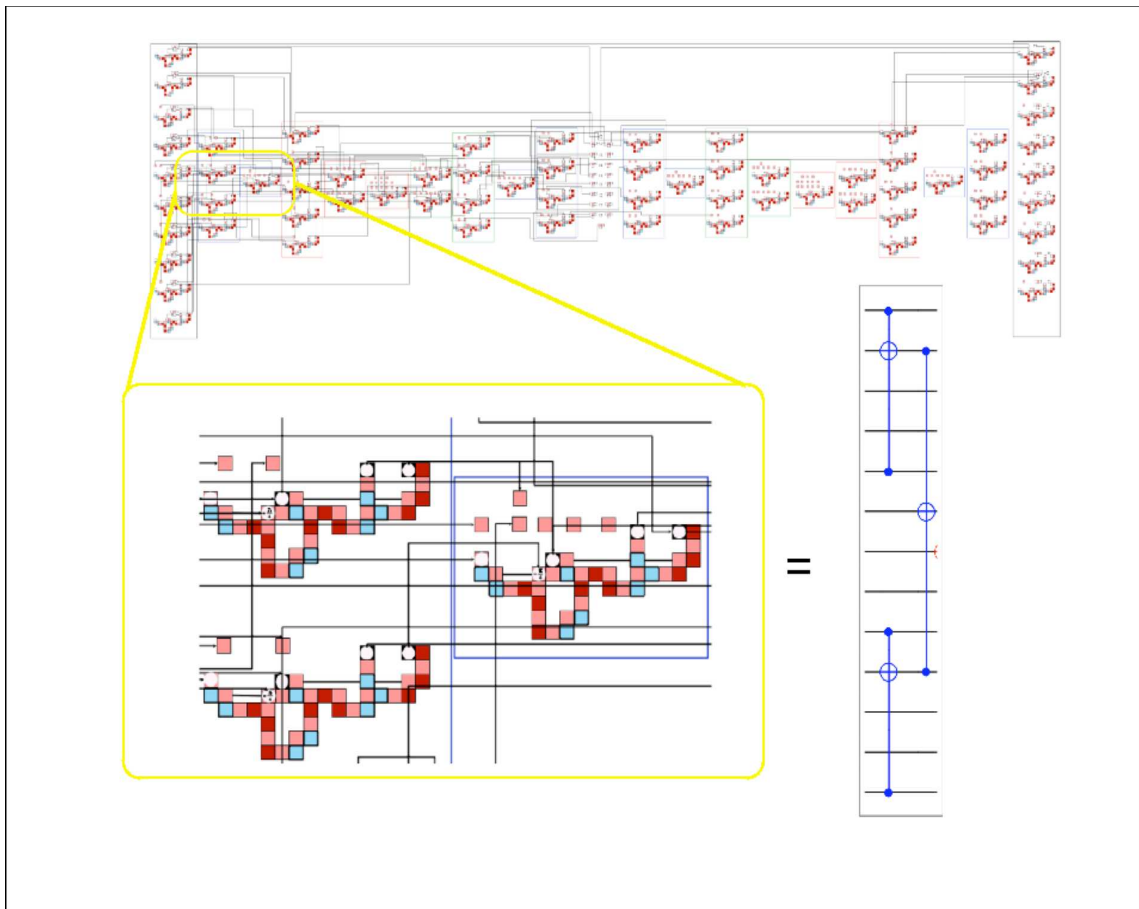


Figure 3.8: MBQCLA figure allowing the use of a graph state for entanglement and communication.

3.4 Limitation and future works

1. **Depth optimization of MBQCLA circuits.** This work explores how to optimize the resources of qubits in MBQCLA. However, the optimization of depth in MBQCLA circuits is still elusive under this scheme, since the unique MBQC may have a unique computational depth complexity^[107]. This aspect needs to be investigated.

Chapter 4

Summary

Measurement-based quantum computation (MBQC) is considered as one of the promising candidates of quantum computation scenarios toward future implementation in real physical systems. By performing subsequent measurements on a system consisting of a set of highly entangled qubits arranged in nearest neighbor manners, which is called cluster state, it is necessary to implement quantum computation on the system. However, MBQC should meet with Divincenzo criteria in order to be realized in the real physical system. Therefore, two issues are discussed in this thesis: the cluster state preparation in cavity quantum electrodynamics, which is illustrated in Fig. (4.1), and the implementation of MBQC into quantum carry-lookahead adders. The contributions of in this thesis with respect to the future developments are provided in Fig. (4.2).

It is shown in Chapter (2) that the perturbation of the atom-field in a cavity by introduction of extra classical electromagnetic field can be used to control the atomic population in the cavity. The perturbation theory on the system is described by employment of one-fold Darboux transformations for the potential transformations of Rabi model. For simplicity, we use the result of this transformation to obtain the Rabi oscillations involving the classical effect. This method shows that it is possible to control the collapse and resurgence of Rabi oscillations in cavity QED under Darboux transformations.

Pauli matrices are the parameters in the BBGS-Darboux transformations to determine the one-dimensional stationary Dirac potential of electromagnetic field. The appropriate choice of the parameters may be necessary for elucidating the responses of the oscillations due to the external perturbations as found in Ref. [87,108].

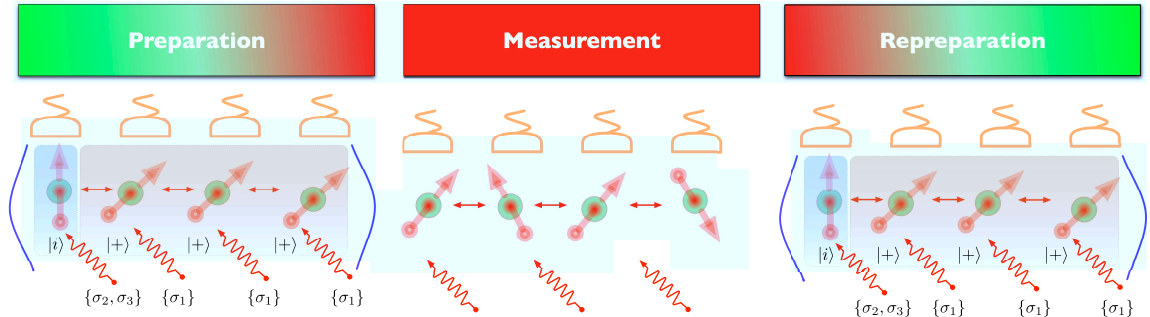


Figure 4.1: Cluster state initialization.

Based on the results, it is possible to propose an *open-loop control* mechanism for Rabi oscillations under Darboux transformations: the operator $\mathcal{D}(\sigma_i)$ is assumed as the controller and σ_i as the system input. The initial state is $\{V, \Psi\}$ and the final state is $\{V[N], \Psi[N]\}$. The output variables that are measured by a sensor are eigenvalues of the new Hamiltonian, $\varepsilon_N(\sigma_i)$. The next challenge is to define an appropriate Darboux transformations so that theoretical explanation of a *closed-loop control* mechanism, as proposed in Ref. [54], can be achieved.

For further studies, it may be interesting to investigate the influence of N -fold Darboux transformations to multi-qubits such as Bose-Einstein condensation of exciton polaritons [109] and Anyons in a weakly interacting system [110]. It is also interesting to expand the Dirac potential to n -dimensions and relates it to various quantum systems. We expect that such an effort will open a new possibility to involve Darboux transformations into the extensive research of quantum information research [80].

Chapter (3) deals with circuit designs for measurement-based quantum computers. Using classical information obtained by measurements over cluster states, circuit designs for several forms of measurement-based quantum carry-lookahead adders (MBQCLA) and graph-state quantum carry-lookahead adders (GSQCLA) are presented. Resources required to perform the quantum carry-lookahead adder are shown as functions of the number of logical qubits, width of quantum gates, and a number of qubits in quantum gates. By bending the network and removing the border between the rounds, the optimization of the in-place MBQCLA circuit

changes its shape from a rectangle to a diamond-like form. The proposed evaluation methods for the cost and performance of application circuits for MBQC will be useful for a large scale quantum computer architecture, since development of circuits for quantum computers will need optimization similar to the one for the classical computer technology.

The work provides a theoretical study on manipulation of qubit populations and architectures for quantum adder towards realization of measurement-based quantum computers. Considering that the proposal is compatible with the framework of present experimental investigations, this work may contribute directly to the next step of MBQC development.

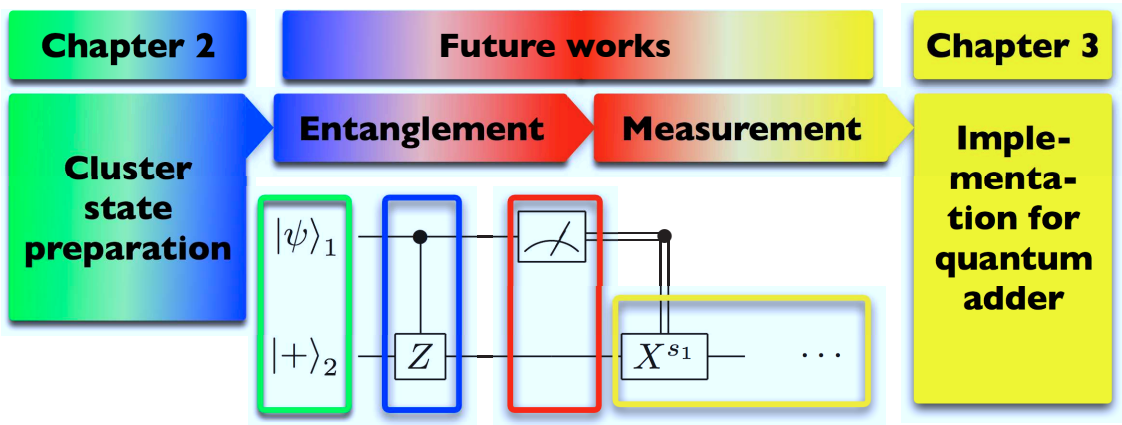


Figure 4.2: A schematic showing the contributions of this thesis and also for the future works.

Appendix A

Homotopy perturbation methods

In this appendix, we provide the algorithm for obtaining exact solution of coupled nonlinear equations^[81].

1. Unravel the differential equations using conventional HPM. In this step, the widely known Taylor series is needed to expand the solution of the nonlinear differential equations, $f(x)$, at the point $x = 0$. The series reads:

$$f(x) = \sum_{i=0}^{\infty} c_i x^i = \sum_{i=0}^{\infty} \frac{f^{(i)}(0)}{i!} x^i. \quad (\text{A.1})$$

2. Shortened the series solution by conventional HPM. This step is accomplished by obtaining the embedding parameter of the solutions.
3. Obtain the Laplace transform of the shortened series. The well-known Laplace transform of a function $y(t)$ reads

$$\mathcal{L}[y(t)] = \hat{y}(s) = \int_0^{\infty} y(t) e^{-st} dt. \quad (\text{A.2})$$

4. Acquire the Padé approximant of the prior step. The Padé approximant is a rational function to approach the Taylor series expansion as best as possible. It gives

$$\left[\frac{M}{N} \right]_{f(x)}(x) = \frac{\sum_{i=0}^M a_i x^i}{1 + \sum_{i=0}^N b_i x^i}, \quad (\text{A.3})$$

where M and N are given positive integers.

5. Obtain the inverse Laplace transform.

Appendix B

Explicit representation for square root of a complex number

Following the Ref. ^[111,112], we provide the theorem to obtain the explicit representation for square root of a complex number.

Theorem. *A complex number*

$$\sqrt{a + ib} \tag{B.1}$$

can be simplified into

$$p + iq \tag{B.2}$$

by defining

$$p = \frac{1}{\sqrt{2}} \sqrt{\sqrt{a^2 + b^2} + a} \tag{B.3}$$

and

$$q = \frac{\text{sgn}(b)}{\sqrt{2}} \sqrt{\sqrt{a^2 + b^2} - a} \tag{B.4}$$

where

$$\{a, b, p, q \in \mathfrak{R} \text{ and } (b \neq 0)\} \tag{B.5}$$

and $\text{sgn}(b) = \frac{b}{|b|}$ is defined as the sign of b (to be $+1$ if $b > 0$ and -1 if $b < 0$).

Appendix C

Computational simulation scheme

This Appendix provides the computational methods to generate graphs in the Section (2.4). In this work, we use *Maple*. The following codes show the codes for modified atomic inversion simulation.

```
[> sim:= exp(-30)*sum(((30)^(n))/(n!)*(1-(2*(Omega)^2)*  
sqrt(Rm+n+1))*((sin(sqrt((kappa)^2+n+1)*t))^2)/(  
(kappa)^2+Rm+n+1)),n=0..1000):  
[>  
[> s7sa:=subs(b[0]=1000.01,h[bar]=0.1,Omega=1,omega=Pi,  
kappa=sqrt(2),%):  
[> plot(sim(t),t=-0..100,numpoints=500,axes=frame,color=  
red);]
```

Figure C.1: *Maple* codes for the *modified* atomic inversion.

The meaning of the parameters in Fig. (C.1) are **Rm** is the *modified* classical electromagnetic field, **sim** is the *modified* atomic inversion, **adj** is the adjustment for atomic inversion in case it is needed, **b[0]** is the amplitude of initial classical electromagnetic field, **h[bar]** is \hbar , **kappa** is κ , **omega** is ω , **Omega** is Ω , and **sol** is the code for setting the value of the constants.

Below, the codes of $\{\mathcal{D}(\sigma_1), \mathcal{D}(\sigma_3), \mathcal{D}(\sigma_2)\}$ solutions are shown, respectively.

```

> reB:=(b[0]+((h_bar)*Omega)-1)*t+((3*b[0]-2)*(1-((h_bar))*
Omega))*sin(omega*t)/(omega*(2*b[0]-1));
> planck(standard);
> reB:=(b[0]+((h_bar)*Omega)-1)*t+((3*b[0]-2)*(1-((h_bar))*
Omega))*sin(omega*t)/(omega*(2*b[0]-1))+(((h_bar)*Omega)-1)
*b[0]*sin(omega*t)/(2*omega*(b[0]-1));
> imB:=(((h_bar)*Omega-1)*(2*b[0]-1))/(omega*(b[0]-1))+((3*b
[0]-2)*(1-(h_bar)*Omega)*cos(omega*t))/(omega*(2*b[0]-1))-((
(h_bar)*Omega)-1)*b[0]*cos(omega*t)/(2*omega*(b[0]-1))-(b[0]
^(2)*t^(2)*omega*((h_bar)*Omega-1))/((2*b[0]-1));
>
> absB:=sqrt((reB)^(2)+(imB)^2);
> Nb:=subs(b[0]=10.01,h[bar]=0.1,Omega=1,omega=Pi,%);
> Rm:=(Nb)^2;

```

Figure C.2: *Maple* codes for the solution of $\mathcal{D}(\sigma_1)$.

```

> Refa[3]:=(b[0]/2)*sin(omega*t);
> Imfa[3]:=(b[0])*sin(omega*t);
> Reina[3]:=-2*(b[0]^2)*((cos(omega*t))^2)+cos(2*omega*t)*((cos
(omega*t))^2)*(b[0]^2)-2*omega*b[0]*cos(2*omega*t)*(sin
(omega*t)+cos(omega*t));
> Imina[3]:=sin(2*omega*t)*((cos(omega*t))^2)*(b[0]^2)-2*omega*
b[0]*sin(2*omega*t)*(sin(omega*t)+cos(omega*t))-2*(b[0]^2)*
sin(omega*t)*cos(omega*t);
> Rep[3]:=(1/sqrt(2))*sqrt(sqrt((Reina[3])^2+(Imina[3]^2))+
Reina[3]);
> Imq[3]:=(sign(Imina[3])/sqrt(2))*sqrt(sqrt((Reina[3])^2+
(Imina[3]^2))-Reina[3]);
> Rera[3]:=Refa[3]-Rep[3]+b[0]*sin(omega*t);
> Imra[3]:=Imfa[3]-Imq[3]-b[0]*cos(omega*t);
> Absbb[3]:=(Imra[3])^2+(Rera[3])^2;
> Rm:=subs(b[0]=0.1,h[bar]=0.1,Omega=0.5,omega=Pi,%);

```

Figure C.3: *Maple* codes for the solution of $\mathcal{D}(\sigma_3)$.

The following diagram shows the scheme of the work in this paper.

```

> Refa[3]:= (b[0]/2)*sin(omega*t);
> Imfa[3]:= (b[0])*sin(omega*t);
> Reina[3]:=-2*(b[0]^2)*((cos(omega*t))^2)+cos(2*omega*t)*((cos(omega*t))^2)*(b[0]^2)-2*omega*b[0]*cos(2*omega*t)*(sin(omega*t)+cos(omega*t));
> Imina[3]:=sin(2*omega*t)*((cos(omega*t))^2)*(b[0]^2)-2*omega*b[0]*sin(2*omega*t)*(sin(omega*t)+cos(omega*t))-2*(b[0]^2)*sin(omega*t)*cos(omega*t);
> Rep[3]:= (1/sqrt(2))*sqrt(sqrt((Reina[3])^2+(Imina[3]^2))+Reina[3]);
> Imq[3]:= (sign(Imina[3])/sqrt(2))*sqrt(sqrt((Reina[3])^2+(Imina[3]^2))-Reina[3]);
> Rera[3]:= Refa[3]-Rep[3]+b[0]*sin(omega*t);
> Imra[3]:= Imfa[3]-Imq[3]-b[0]*cos(omega*t);
> Absbb[3]:= (Imra[3])^2+(Rera[3])^2;
> Nbn[3]:= subs(b[0]=0.00001, h[bar]=0.1, Omega=0.5, omega=Pi, %);
> s7a2:= (1)*(10^11)*exp(-30)*sum(((3)^(n))/(n!)*(1-(2*(Omega)^2)*sqrt(Nbn[3]+n+1)*((sin(sqrt(kappa+Nbn[3]+n+1)*t))^2)/(kappa+Nbn[3]+n+1)), n=0..1000)+0.118;
>
> s7sa2:= subs(h[bar]=0.1, Omega=1, omega=Pi, kappa=sqrt(2), %);
> plot(s7sa2(t)-0.24, t=-0..100, numpoints=6000, axes=frame, color=red);
>

```

Figure C.4: *Maple* codes for the modified atomic inversion in the case of $\mathcal{D}(\sigma_2)$.

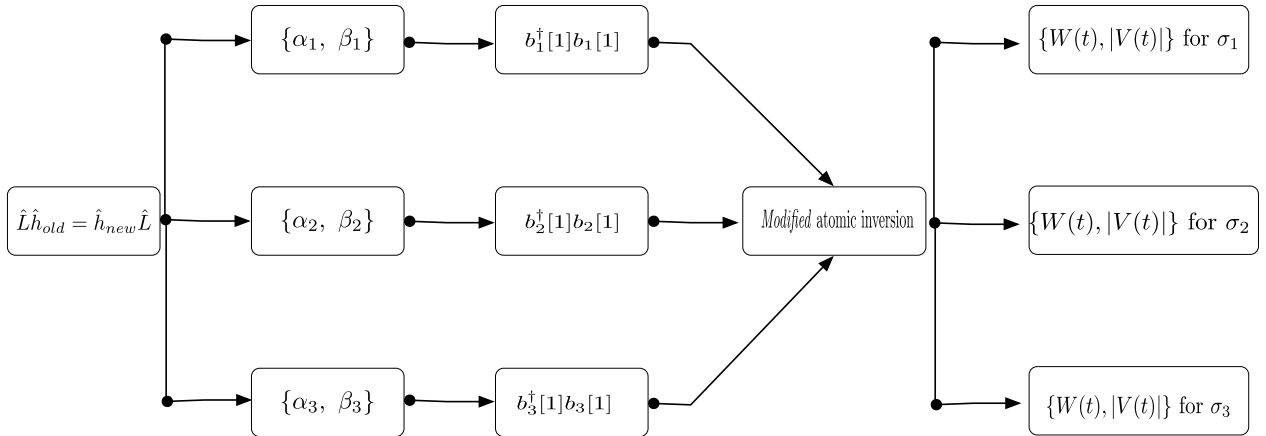


Figure C.5: The scheme for obtaining the correlations between atomic inversion and Dirac potentials.

Appendix D

List of Papers and Presentations

D.1 Journals

1. A. Trisetyarso, “*Correlation of Dirac potentials and atomic inversion in cavity quantum electrodynamics*”, [arXiv:0912.4819](#), *J. Math. Phys.* **51**, 072103 (2010); [doi:10.1063/1.3458598](#).
2. A. Trisetyarso and R. Van Meter, “*Circuit Design for A Measurement-Based Quantum Carry-Lookahead Adder*”, [arXiv:0903.0748](#), *Int. J. Quantum Inf.* **8**, 843 (2010); [doi:10.1142/S0219749910006496](#).

D.2 Conferences

1. A. Trisetyarso, R. Van Meter, and Kohei. M. Itoh, “*Resources for Measurement-Based Quantum Carry-Lookahead Adder*”, [arXiv:0901.3903](#), *International Symposium on Nanoscale Transport and Technology 2009, NTT, Hon Atsugi, Japan*.
2. A. Trisetyarso, R. Van Meter, and Kohei. M. Itoh, “*A Measurement-Based Form of the Out-of-Place Quantum Carry-Lookahead Adder*”,

[arXiv:0901.3901](https://arxiv.org/abs/0901.3901), *Asian Conference on Quantum Information Science 2008*,
KIAS, South Korea.

D.3 Workshop

1. *Workshop on Quantum Statistical Mechanics, Computation and Information*, 14 June - 18 June 2010, ICTP Trieste, Italy.

References

- [1] R.P. Feynman, R. Leighton, and E. Hutchings. " *Surely you're joking, Mr. Feynman!*": adventures of a curious character. WW Norton & Company, 1997. [iii](#)
- [2] R.P. Feynman. Simulating physics with computers. *International journal of theoretical physics*, 21(6):467–488, 1982. [1](#)
- [3] J.P. Dowling and G.J. Milburn. Quantum technology: the second quantum revolution. *Philosophical Transactions of the Royal Society of London. Series A: Mathematical, Physical and Engineering Sciences*, 361(1809):1655, 2003. [1](#)
- [4] G. Brassard. Is information the key? *Nature Physics*, 1(1):2–4, 2005. [1](#)
- [5] S. Barnett. *Quantum information*. Oxford University Press, USA, 2009. [1](#)
- [6] Benjamin Schumacher. Quantum coding. *Phys. Rev. A*, 51(4):2738–2747, Apr 1995. [2](#)
- [7] J.P. Preskill. Course Notes for California Institute of Technology Physics 219, 1997. [4](#), [7](#), [10](#), [30](#)
- [8] Adriano Barenco, Charles H. Bennett, Richard Cleve, David P. DiVincenzo, Norman Margolus, Peter Shor, Tycho Sleator, John A. Smolin, and Harald Weinfurter. Elementary gates for quantum computation. *Phys. Rev. A*, 52(5):3457–3467, Nov 1995. [5](#), [7](#), [8](#)
- [9] Dagmar Bruss. Characterizing entanglement. *Journal of Mathematical Physics*, 43(9):4237–4251, 2002. [5](#)

REFERENCES

- [10] J.S. Bell et al. On the einstein-podolsky-rosen paradox. *Physics*, 1(3):195–200, 1964. [5](#)
- [11] D.M. Greenberger, M.A. Horne, and A. Zeilinger. Going beyond Bell’s theorem. *Bell’s theorem, quantum theory, and conceptions of the universe*, pages 69–72, 1989. [5](#)
- [12] H J Briegel and R Raussendorf. Persistent entanglement in arrays of interacting particles. *Phys. Rev. Lett.*, 86(5):910–913, 2001 Jan 29. [5](#), [64](#)
- [13] Ryszard Horodecki, Paweł Horodecki, Michał Horodecki, and Karol Horodecki. Quantum entanglement. *Rev. Mod. Phys.*, 81(2):865–942, Jun 2009. [5](#)
- [14] Seth Lloyd. Almost any quantum logic gate is universal. *Phys. Rev. Lett.*, 75(2):346–349, Jul 1995. [7](#)
- [15] E. Fredkin and T. Toffoli. Conservative logic. *International Journal of Theoretical Physics*, 21(3):219–253, 1982. [7](#), [9](#)
- [16] D. Deutsch. Quantum Computational Networks. *Proceedings of the Royal Society of London. A. Mathematical and Physical Sciences*, 425(1868):73–90, 1989. [9](#)
- [17] T. Toffoli. Reversible computing. *Automata, Languages and Programming*, pages 632–644, 1980. [9](#)
- [18] P.W. Shor. Algorithms for quantum computation: Discrete logarithms and factoring. In *ANNUAL SYMPOSIUM ON FOUNDATIONS OF COMPUTER SCIENCE*, volume 35, pages 124–124. Citeseer, 1994. [14](#)
- [19] E. Farhi, J. Goldstone, S. Gutmann, and M. Sipser. Quantum computation by adiabatic evolution. *Arxiv preprint quant-ph/0001106, MIT-CTP-2936*, 2000.
- [20] Lov K. Grover. A fast quantum mechanical algorithm for database search. In *Proceedings of the twenty-eighth annual ACM symposium on Theory of computing, STOC ’96*, pages 212–219, New York, NY, USA, 1996. ACM.

REFERENCES

- [21] Robert Raussendorf, Daniel E. Browne, and Hans J. Briegel. Measurement-based quantum computation on cluster states. *Phys. Rev. A*, 68(2):022312, Aug 2003. [14](#), [20](#), [21](#), [25](#), [64](#), [65](#), [66](#), [73](#), [80](#)
- [22] C.H. Bennett, G. Brassard, et al. Quantum cryptography: Public key distribution and coin tossing. In *Proceedings of IEEE International Conference on Computers, Systems and Signal Processing*, volume 175. Bangalore, India, 1984. [14](#)
- [23] S. Lloyd. Ultimate physical limits to computation. *Nature*, 406(6799):1047, 2000. [14](#)
- [24] T. D. Ladd, J. R. Goldman, F. Yamaguchi, Y. Yamamoto, E. Abe, and K. M. Itoh. All-silicon quantum computer. *Phys. Rev. Lett.*, 89(1):017901, Jun 2002. [14](#)
- [25] B.E. Kane. A silicon-based nuclear spin quantum computer. *Nature*, 393(6681):133–138, 1998. [14](#)
- [26] D. Bouwmeester, J.W. Pan, K. Mattle, M. Eibl, H. Weinfurter, and A. Zeilinger. Experimental quantum teleportation. *Nature*, 390(6660):575–579, 1997. [14](#)
- [27] T. D. Ladd, F. Jelezko, R. Laflamme, Y. Nakamura, C. Monroe, and J. L. O’Brien. Quantum computers. *Nature*, 464(7285):45–53, 03 2010. [14](#)
- [28] Michael Nielsen and I. Chuang. *Quantum Computation and Quantum Information*. Cambridge University Press, Cambridge :, 2000. [14](#), [15](#), [16](#), [30](#)
- [29] T.M. Apostol. Calculus, volume II. *American Journal of Physics*, 31:401–402, 1963. [15](#)
- [30] Edward Witten. Dynamical breaking of supersymmetry. *Nuclear Physics B*, 188(3):513 – 554, 1981. [16](#)
- [31] L. M. Nieto, A. A. Pecheritsin, and Boris F. Samsonov. Intertwining technique for the one-dimensional stationary dirac equation. *Annals of Physics*, 305(2):151 – 189, 2003. [16](#), [35](#), [37](#)

-
- [32] Matthias Ernzerhof and Francois Goyer. Conjugated molecules described by a one-dimensional dirac equation. *Journal of Chemical Theory and Computation*, 6(6):1818–1824, 2010. [16](#)
- [33] D.P. DiVincenzo. The physical implementation of quantum computation. *Fortschritte der Physik*, 48(9-11):771–783, 2000. [17](#), [28](#)
- [34] S. Lloyd. A Potentially Realizable Quantum Computer. *Science*, 261(5128):1569, 1993. [18](#), [69](#)
- [35] P Walther, K J Resch, T Rudolph, E Schenck, H Weinfurter, V Vedral, M Aspelmeyer, and A Zeilinger. Experimental one-way quantum computing. *Nature*, 434(7030):169–176, 2005 Mar 10. [19](#), [64](#)
- [36] R Raussendorf and H J Briegel. A one-way quantum computer. *Phys. Rev. Lett.*, 86(22):5188–5191, 2001 May 28. [20](#), [64](#)
- [37] Daniel E Browne and Terry Rudolph. Resource-efficient linear optical quantum computation. *Phys. Rev. Lett.*, 95(1):010501, 2005 Jul 1. [20](#)
- [38] Vincent Danos, Elham Kashefi, and Prakash Panangaden. The measurement calculus. *J. ACM*, 54(2):8, 2007. [20](#)
- [39] Gerardo Ortiz Larisse D. Voufo and Amr Sabry. Quantum circuits: From a network to a one-way model - a tutorial version. Proceedings of the DCM-QPL’08 workshop, June 2008. [20](#), [81](#)
- [40] F Meier, J Levy, and D Loss. Quantum computing with antiferromagnetic spin clusters. *Physical Review B*, 68(13), OCT 1 2003. [21](#), [72](#)
- [41] Alberto Politi, Martin J. Cryan, John G. Rarity, Siyuan Yu, and Jeremy L. O’Brien. Silica-on-silicon waveguide quantum circuits. *Science*, 320(5876):646–649, MAY 2 2008. [21](#), [72](#)
- [42] Simon J. Devitt, Austin G. Fowler, Ashley M. Stephens, Andrew D. Green-tree, Lloyd C. L. Hollenberg, William J. Munro, and Kae Nemoto. Topological cluster state computation with photons. arXiv:0808.1782v1, 2008. [21](#), [72](#)

-
- [43] S.G.R. Louis, K. Nemoto, WJ Munro, and TP Spiller. The efficiencies of generating cluster states with weak nonlinearities. *New Journal of Physics*, 9:193, 2007. [21](#)
- [44] DW Leung. Quantum computation by measurements. *International Journal of Quantum Information*, 2(1):33–43, MAR 2004. [23](#)
- [45] V. B. Matveev and M. A. Salle. *Darboux Transformations and Solitons*. Springer Series in Nonlinear Dynamics. Springer, 1990. [25](#), [34](#)
- [46] A. Trisetyarso. Application of darboux transformation to solve multisoliton solution on non-linear schrödinger equation. Undergraduate thesis, Institut Teknologi Bandung, July 2000. [28](#)
- [47] T. Pellizzari, S. A. Gardiner, J. I. Cirac, and P. Zoller. Decoherence, continuous observation, and quantum computing: A cavity qed model. *Phys. Rev. Lett.*, 75(21):3788–3791, Nov 1995. [28](#)
- [48] Q. A. Turchette, C. J. Hood, W. Lange, H. Mabuchi, and H. J. Kimble. Measurement of conditional phase shifts for quantum logic. *Phys. Rev. Lett.*, 75(25):4710–4713, Dec 1995. [28](#)
- [49] J. Cho and H.W. Lee. Generation of atomic cluster states through the cavity input-output process. *Physical review letters*, 95(16):160501, 2005. [28](#)
- [50] Liu Ye, Long-Bao Yu, and Guang-Can Guo. Generation of entangled states in cavity qed. *Phys. Rev. A*, 72(3):034304, Sep 2005. [29](#)
- [51] XuBo Zou and W. Mathis. Schemes for generating the cluster states in microwave cavity qed. *Phys. Rev. A*, 72(1):013809, Jul 2005. [28](#)
- [52] P J Blythe and B T H Varcoe. A cavity-qed scheme for cluster-state quantum computing using crossed atomic beams. *New Journal of Physics*, 8(10):231, 2006. [28](#)
- [53] Xin-Wen Wang and Guo-Jian Yang. Schemes for preparing atomic qubit cluster states in cavity qed. *Optics Communications*, 281(20):5282 – 5285, 2008. [29](#)

REFERENCES

- [54] H. Mabuchi and A. C. Doherty. Cavity Quantum Electrodynamics: Coherence in Context. *Science*, 298(5597):1372–1377, 2002. [30](#), [31](#), [91](#)
- [55] JE Mooij, TP Orlando, L. Levitov, L. Tian, C.H. Van der Wal, and S. Lloyd. Josephson persistent-current qubit. *Science*, 285(5430):1036, 1999. [30](#)
- [56] M. Brune, F. Schmidt-Kaler, A. Maali, J. Dreyer, E. Hagley, J. M. Raimond, and S. Haroche. Quantum rabi oscillation: A direct test of field quantization in a cavity. *Phys. Rev. Lett.*, 76(11):1800–1803, Mar 1996.
- [57] TH Stievater, X. Li, DG Steel, D. Gammon, DS Katzer, D. Park, C. Piermarocchi, and LJ Sham. Rabi oscillations of excitons in single quantum dots. *Physical Review Letters*, 87(13):133603, 2001.
- [58] C. Boehme and K. Lips. Electrical detection of spin coherence in silicon. *Physical review letters*, 91(24):246603, 2003. [30](#)
- [59] P. Knight and GC Gerry. *Introductory Quantum Optics*. Cambridge University Press, 2005. [31](#)
- [60] O. Babelon. A SHORT INTRODUCTION TO CLASSICAL AND QUANTUM INTEGRABLE SYTEMS. *Lecture Notes*, 2007. [31](#)
- [61] J. M. Raimond, M. Brune, and S. Haroche. Manipulating quantum entanglement with atoms and photons in a cavity. *Rev. Mod. Phys.*, 73(3):565–582, Aug 2001. [33](#)
- [62] Murray Gell-Mann and James B. Hartle. Classical equations for quantum systems. *Phys. Rev. D*, 47(8):3345–3382, Apr 1993. [33](#)
- [63] Charles H. Bennett, Gilles Brassard, Claude Crépeau, Richard Jozsa, Asher Peres, and William K. Wootters. Teleporting an unknown quantum state via dual classical and einstein-podolsky-rosen channels. *Phys. Rev. Lett.*, 70(13):1895–1899, Mar 1993. [33](#)
- [64] A. Imamog̃lu, H. Schmidt, G. Woods, and M. Deutsch. Strongly interacting photons in a nonlinear cavity. *Phys. Rev. Lett.*, 79(8):1467–1470, Aug 1997. [33](#)

- [65] K.M. Birnbaum, A. Boca, R. Miller, A.D. Boozer, T.E. Northup, and H.J. Kimble. Photon blockade in an optical cavity with one trapped atom. *Nature*, 436(7047):87–90, 2005. [33](#), [62](#)
- [66] Daniel A. Steck, Kurt Jacobs, Hideo Mabuchi, Tanmoy Bhattacharya, and Salman Habib. Quantum feedback control of atomic motion in an optical cavity. *Phys. Rev. Lett.*, 92(22):223004, Jun 2004. [34](#)
- [67] R. R. Puri and G. S. Agarwal. Collapse and revival phenomena in the jaynes-cummings model with cavity damping. *Phys. Rev. A*, 33(5):3610–3613, May 1986.
- [68] EB Flagg, A. Muller, JW Robertson, S. Founta, DG Deppe, M. Xiao, W. Ma, GJ Salamo, and CK Shih. Resonantly driven coherent oscillations in a solid-state quantum emitter. *Nature Physics*, 5(3):203–207, 2009.
- [69] S. Rudin and TL Reinecke. Anharmonic oscillator model for driven and vacuum-field Rabi oscillations. *Physical Review B*, 63(7):75308, 2001. [34](#)
- [70] J. Förstner, C. Weber, J. Danckwerts, and A. Knorr. Phonon-assisted damping of rabi oscillations in semiconductor quantum dots. *Phys. Rev. Lett.*, 91(12):127401, Sep 2003. [34](#)
- [71] Norihito Kosugi, Shigemasa Matsuo, Kohkichi Konno, and Noriyuki Hatakenaka. Theory of damped rabi oscillations. *Phys. Rev. B*, 72(17):172509, Nov 2005.
- [72] Subir Sachdev. Atom in a damped cavity. *Phys. Rev. A*, 29(5):2627–2633, May 1984. [34](#)
- [73] J.L. Shao, D. Suqing, and X.G. Zhao. Dynamics of coupled chains in an ac electric and a magnetic fields. *Physics Letters A*, 330(3-4):267–273, 2004. [34](#)
- [74] V. Hussin, Ş. Kuru, and J. Negro. Generalized Jaynes–Cummings Hamiltonians. *Journal of Physics A: Mathematical and General*, 39:11301–11311, 2006. [34](#)

-
- [75] Boris F Samsonov and Javier Negro. Darboux transformations of the jaynes and cummings hamiltonian. *Journal of Physics A: Mathematical and General*, 37(43):10115–10127, 2004. [34](#)
- [76] V. Bagrov, M. Baldiotti, D. Gitman, and V. Shamshutdinova. Darboux transformation for two-level system. *Annalen der Physik*, 14(6):390–397, 2005. [34](#), [36](#)
- [77] Arlen Anderson. Intertwining of exactly solvable dirac equations with one-dimensional potentials. *Phys. Rev. A*, 43(9):4602–4610, May 1991. [34](#)
- [78] Boris F Samsonov and V V Shamshutdinova. Dynamical qubit controlling via pseudo-supersymmetry of two-level systems. *Journal of Physics A: Mathematical and Theoretical*, 41(24):244023 (9pp), 2008. [35](#)
- [79] DF Walls and G.J. Milburn. *Quantum optics*. Springer, 2006. [35](#)
- [80] Agung Trisetyarso. Dirac four-potential tunings-based quantum transistor utilizing the lorentz force. *arXiv/1003.4590*, 2010. [36](#), [91](#)
- [81] NH Sweilam and MM Khader. Exact solutions of some coupled nonlinear partial differential equations using the homotopy perturbation method. *Computers and Mathematics with Applications*, 2009. [38](#), [40](#), [93](#)
- [82] M. Nomura, N. Kumagai, S. Iwamoto, Y. Ota, and Y. Arakawa. Laser oscillation in a strongly coupled single-quantum-dot–nanocavity system. *Nature Physics*, 2010. [38](#)
- [83] Agung Trisetyarso. Correlation of dirac potentials and atomic inversion in cavity quantum electrodynamics. *Journal of Mathematical Physics*, 51(7):072103, 2010. [39](#)
- [84] J.H. He. Homotopy perturbation method: a new nonlinear analytical technique* 1. *Applied Mathematics and Computation*, 135(1):73–79, 2003. [40](#)
- [85] P. Alsing, D.-S. Guo, and H. J. Carmichael. Dynamic stark effect for the jaynes-cummings system. *Phys. Rev. A*, 45(7):5135–5143, Apr 1992. [49](#)

REFERENCES

- [86] L. Tian and H. J. Carmichael. Quantum trajectory simulations of two-state behavior in an optical cavity containing one atom. *Phys. Rev. A*, 46(11):R6801–R6804, Dec 1992. [49](#)
- [87] L.S. Bishop, JM Chow, J. Koch, AA Houck, MH Devoret, E. Thuneberg, SM Girvin, and RJ Schoelkopf. Nonlinear response of the vacuum Rabi resonance. *Nature Physics*, 5(2):105–109, 2008. [50](#), [90](#)
- [88] A. Kubanek, M. Koch, C. Sames, A. Ourjoumtsev, P. W. H. Pinkse, K. Murr, and G. Rempe. Photon-by-photon feedback control of a single-atom trajectory. *Nature*, 462(7275):898–901, 12 2009. [62](#)
- [89] LV Keldysh. Ionization in the field of a strong electromagnetic wave(Multiphonon absorption processes and ionization probability for atoms and solids in strong electromagnetic field). *Soviet Physics-JETP*, 20:1307–1314, 1965. [62](#)
- [90] P. Colosimo, G. Doumy, C. I. Blaga, J. Wheeler, C. Hauri, F. Catoire, J. Tate, R. Chirla, A. M. March, G. G. Paulus, H. G. Muller, P. Agostini, and L. F. DiMauro. Scaling strong-field interactions towards the classical limit. *Nat Phys*, 4(5):386–389, 05 2008. [62](#)
- [91] H. J. Briegel, D. E. Browne, W. Dur, R. Raussendorf, and M. Van den Nest. Measurement-based quantum computation. *Nature Physics*, pages 19–26, 01 2009. [64](#)
- [92] Tetsufumi Tanamoto, Yu-xi Liu, Shinobu Fujita, Xuedong Hu, and Franco Nori. Producing cluster states in charge qubits and flux qubits. *Phys. Rev. Lett.*, 97(23):230501, 2006 Dec 8. [64](#), [72](#)
- [93] Peter W. Shor. Polynomial-time algorithms for prime factorization and discrete logarithms on a quantum computer. *SIAM J. Comput.*, 26(5):1484–1509, 1997. [65](#)
- [94] V Vedral V, A Barenco, and A Ekert. Quantum networks for elementary arithmetic operations. *Phys. Rev. A*, 54(1):147–153, 1996 Jul. [65](#)

-
- [95] D Beckman, AN Chari, S Devabhaktuni, and J Preskill. Efficient networks for quantum factoring. *Phys. Rev. A*, 54(2):1034–1063, 1996 Aug. [65](#)
- [96] Rodney Van Meter and Kohei M. Itoh. Fast quantum modular exponentiation. *Phys. Rev. A*, 71(5):052320, May 2005. [65](#)
- [97] Rodney Van Meter and Mark Oskin. Architectural implications of quantum computing technologies. *ACM Journal on Emerging Technologies in Computing Systems*, 2(1):31–63, 2006. [65](#)
- [98] Byung-Soo Choi and Rodney Van Meter. Effects of interaction distance on quantum addition circuits. *To appear in ACM J. Emerging Tech. in Comp. Sys., quant-ph:0809.4317*, 2008. [65](#), [70](#)
- [99] Steven A. Cuccaro, Thomas G. Draper, Samuel A. Kutin, and David Petrie Moulton. A new quantum ripple-carry addition circuit. arXiv:quant-ph/0410184v1, 2004. [65](#)
- [100] Y Takahashi and N Kunihiro. A linear-size quantum circuit for addition with no ancillary qubits. *Quantum Information & Computation*, 5(6):440–448, SEP 2005. [65](#)
- [101] Thomas G. Draper, Samuel A. Kutin, Eric M. Rains, and Krysta M. Svore. A logarithmic-depth quantum carry-lookahead adder. *Quantum Information & Computation*, 6(4-5):351–369, JUL 2006. [65](#), [66](#), [68](#), [76](#)
- [102] Milos D. Ercegovic and Tomas Lang. *Digital Arithmetic*. Morgan-Kaufman, San Francisco, 2004. [67](#)
- [103] A. Broadbent and E. Kashefi. Parallelizing quantum circuits. *Theoretical Computer Science*, 410(26):2489–2510, 2009. [69](#)
- [104] J. Q. You, Xiang-bin Wang, Tetsufumi Tanamoto, and Franco Nori. Efficient one-step generation of large cluster states with solid-state circuits. *Physical Review A*, 75(5), MAY 2007. [72](#)
- [105] YS Weinstein, CS Hellberg, and J Levy. Quantum-dot cluster-state computing with encoded qubits. *Phys. Rev. A*, 72(2), AUG 2005.

REFERENCES

- [106] Florian Meier, Jeremy Levy, and Daniel Loss. Quantum computing with spin cluster qubits. *Phys. Rev. Lett.*, 90(4):047901, 2003 Jan 31. [72](#)
- [107] D.E. Browne, E. Kashefi, and S. Perdrix. Computational depth complexity of measurement-based quantum computation. *Arxiv preprint arXiv:0909.4673*, 2009. [89](#)
- [108] K. Hennessy, A. Badolato, M. Winger, D. Gerace, M. Atature, S. Gulde, S. Falt, EL Hu, and A. Imamoglu. Quantum nature of a strongly coupled single quantum dot–cavity system. *Nature*, 445(7130):896–899, 2007. [90](#)
- [109] J. Kasprzak, M. Richard, S. Kundermann, A. Baas, P. Jeambrun, JMJ Keeling, FM Marchetti, MH Szymanska, R. Andre, JL Staehli, et al. Bose-Einstein condensation of exciton polaritons. *NATURE-LONDON*, 443(7110):409, 2006. [91](#)
- [110] C. Weeks, G. Rosenberg, B. Seradjeh, and M. Franz. Anyons in a weakly interacting system. *Nat Phys*, 3(11):796–801, 11 2007. [91](#)
- [111] A. Mostowski and M. Stark. *Introduction to higher algebra*. Pergamon, 1964. [95](#)
- [112] S. Rabinowitz. How to Find the Square Root of a Complex Number. *Mathematics and Informatics Quarterly*, 3:54–56, 1993. [95](#)